



Universiteit  
Leiden  
The Netherlands

## **Towards a single-molecule FRET study of Frauenfelder's nonexponential rebinding of CO in myoglobin**

Eskandari Alughare, Z.

### **Citation**

Eskandari Alughare, Z. (2022, June 23). *Towards a single-molecule FRET study of Frauenfelder's nonexponential rebinding of CO in myoglobin*. *Casimir PhD Series*. Retrieved from <https://hdl.handle.net/1887/3348505>

Version: Publisher's Version

License: [Licence agreement concerning inclusion of doctoral thesis in the Institutional Repository of the University of Leiden](#)

Downloaded from: <https://hdl.handle.net/1887/3348505>

**Note:** To cite this publication please use the final published version (if applicable).

# Towards a single-molecule FRET study of Frauenfelder's nonexponential rebinding of CO in myoglobin

Proefschrift

ter verkrijging van  
de graad van doctor aan de Universiteit Leiden,  
op gezag van rector magnificus prof.dr.ir. H. Bijl,  
volgens besluit van het college voor promoties  
te verdedigen op donderdag 23 juni 2022  
klokke 13.45 uur

door

Zohre Eskandari Alughare

geboren te Falavarjan-Isfahan, Iran  
in 1979

Promotores: Prof. dr. M.A.G.J. Orrit  
Prof. dr. S.A. Bonnet

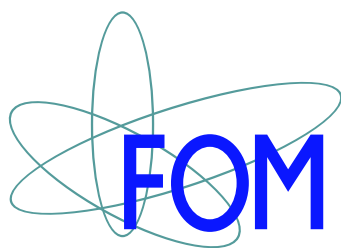
Promotiecommissie: Prof. dr. R. Croce (Vrije Universiteit Amsterdam)  
Prof. dr. D. C. Lamb (Ludwig-Maximilians-Universität München, Munich,  
Duitsland)  
Prof. dr. J. Aarts  
Dr. A. Pandit  
Prof. dr. T. Schmidt



Universiteit  
Leiden  
The Netherlands



*Casimir*  
research school



Nederlandse Organisatie voor Wetenschappelijk Onderzoek

Casimir PhD series, Delft-Leiden 2022-17

ISBN 978-90-8593-528-5

An electronic version of this thesis can be found at <https://openaccess.leidenuniv.nl>

This work is part of the research programme of the Foundation of Fundamental Research on Matter (FOM), which is now part of Netherlands Organization for Scientific Research (NOW). The research of this thesis was performed at Leiden University.

Cover: designed and draw by Mrs. Zohre Eskandari Alughare. The front side of cover shows two states of fluorescent dye-labeled Myoglobin: the left 3D structure and the left cartoon show dye-labeled carboxymyoglobin (MbCO) and the right 3D structure and the right cartoon show dye-labeled deoxymyoglobin (Deoxy-Mb). They demonstrate that when CO bound to the myoglobin (MbCO), less FRET and less quenching effect occurs and the fluorescent dye shines, whereas in Deoxy-Mb, the attached dye is quenched due to the higher FRET. It is possible to follow this conversion in a microscope. At the bottom, the structure of heme in two states are shown. The back cover presents two fluorescent dyes (donor-acceptor) doped in a polymeric layer of PMMA to study FRET quenching at both single-molecule and ensemble levels.

*To my husband: Payam*

*and*

*To our parents*





# Contents

<b>1</b>	<b>Introduction.....</b>	<b>1</b>
1.1	Luminescence .....	2
1.2	Photoluminescence .....	2
1.3	Properties of fluorophores .....	4
1.3.1	<i>Molar absorption coefficient</i> .....	4
1.3.2	<i>Quantum yield</i> .....	4
1.3.3	<i>Fluorescence lifetime</i> .....	5
1.4	Fluorescence resonance energy transfer (FRET) .....	5
1.4.1	<i>Distance between donor and acceptor</i> .....	7
1.4.2	<i>The overlap integral</i> .....	7
1.4.3	<i>The orientation factor <math>\kappa^2</math></i> .....	9
1.5	Ensemble and single-molecule spectroscopy .....	10
1.6	Confocal microscopy .....	11
1.6.1	<i>Time-Correlated Single-Photon Counting (TCSPC)</i> .....	12
1.7	Proteins .....	12
1.7.1	<i>Primary Structure</i> .....	12
1.7.2	<i>Secondary Structure</i> .....	14
1.7.3	<i>Tertiary Structure</i> .....	14
1.7.4	<i>Quaternary Structure</i> .....	15
1.8	FRET in proteins.....	16
	References .....	18
<b>2</b>	<b>The photodissociation of carboxymyoglobin (MbCO).....</b>	<b>23</b>
2.1	Myoglobin function.....	24
2.2	Myoglobin structure .....	24
2.3	Components of MbCO and deoxy-Mb spectra .....	27
2.3.1	<i>Soret Band</i> .....	27
2.3.2	<i>Q- Band</i> .....	28
2.3.3	<i>Near Infrared</i> .....	28
2.4	Photodissociation and its mechanism .....	29
2.5	Photodissociation of Mb-CO bond .....	30
2.6	Photodissociation and CO rebinding at room temperature.....	34
2.7	Photodissociation at low temperature.....	36
2.7.1	<i>Model for photodissociation at low temperature</i> .....	36
2.8	Outline .....	40
	References .....	41

### 3 Estimation of dissociation quantum yield of the Mb-CO bond ... 49

3.1 Introduction .....	50
3.1.1 Does red light ( $\lambda > 700$ nm) break the Mb-CO bond?.....	52
3.1.2 Preparation of MbCO and deoxy-Mb from Met-Mb .....	52
3.1.3 Photodissociation methods .....	53
3.2 Results .....	54
3.2.1 Preparation of deoxy-Mb and MbCO from met-Mb .....	54
3.2.2 Design of the setup .....	56
3.2.3 Study of photodissociation kinetics of Mb-CO and designed experiment .....	56
3.2.4 Control experiment .....	58
3.2.5 Study of the photodissociation kinetics of Mb-CO in the presence of.....	
H <sub>2</sub> O <sub>2</sub> under blue LED illumination ( $\lambda = 450$ nm) .....	60
3.2.6 Study of photodissociation kinetics of the Mb-CO in presence of H <sub>2</sub> O <sub>2</sub> ...	
and red LED illumination ( $\lambda = 730$ nm) .....	61
3.2.7 Estimation of photon rate .....	62
3.2.8 Comparison and calculation of quantum yield efficiency for .....	
photodissociation of unlabeled Mb-CO by red and blue LEDs .....	64
3.3 Conclusion and outlook .....	64
References .....	65

### 4 FRET study of CO binding to fluorescently labeled myoglobin . 67

4.1 Introduction .....	68
4.1.1. Can we measure the FRET efficiency of different states of labeled.....	
Mb(CO)? .....	69
4.1.2 Investigating rebinding kinetics of CO to Mb with FRET .....	70
4.2 Results .....	70
4.2.1 Labeling position and fluorescent dye selection .....	70
4.2.2 Preparation of labeled Mb variants .....	74
4.2.3 Materials and equipment .....	74
4.2.4 Labeling and characterization of met-Mb .....	74
4.2.5 Preparation of ATTO 643-, Cy7-, and ATTO 740 -labeled deoxy-Mb .....	
and MbCO .....	78
4.2.6 Ensemble fluorescence lifetime measurement of ATTO 643-, Cy7-, .....	
and ATTO 740-labeled Mb .....	79
4.2.7 Comparison of ensemble fluorescence lifetime measurement of ATTO...	
643-, Cy7-, and ATTO 740-labeled deoxy-Mb, MbCO, and met-Mb .....	81
4.3 Discussion .....	84
4.3.1 Fluorescent labelling and preparation of different states of Mb .....	84
4.3.2 Comparison of calculated Förster resonance energy transfer .....	
parameters and experimental lifetime .....	84
4.3.3 Förster resonance energy transfer radius ( $R_0$ ) .....	85
4.3.4 Förster Resonance Energy Transfer Rate ( $k_{ET}$ ) and Energy Transfer .....	
Efficiency ( $E$ ) .....	85
4.4 Conclusion .....	90
Reference .....	90

<b>5 FRET to a distribution of acceptors at the ensemble and single-molecule levels .....</b>	<b>93</b>
5.1 Introduction .....	94
5.1.1 <i>Non-fluorescent quenching</i> .....	94
5.1.2 <i>Donor: Long-lifetime fluorescent ADOTA dye, a triangulenium dye</i> .....	95
5.1.3 <i>Acceptor: ATTO575Q, a non-fluorescent quencher dye</i> .....	95
5.1.4 <i>Calculation of the Förster radius <math>R_0</math> for ADOTA (donor)- ATTO575Q.....</i> ( <i>acceptor</i> ) .....	96
5.1.5 <i>Ensemble fluorescent quenching</i> .....	96
5.1.6 <i>Ensemble measurements of fluorescence quenching in solid-state dye-doped polymer layers.....</i>	97
5.1.7 <i>Fluorescence quenching as a function of quencher concentration</i> .....	97
5.1.8 <i>Single-molecule fluorescence quenching</i> .....	98
5.2 Results .....	99
5.2.1 <i>Confocal setup</i> .....	99
5.2.2 <i>Surface preparation of glass microscope cover slips.....</i>	100
5.2.3 <i>Ensemble sample preparation</i> .....	100
5.2.4 <i>Ensemble fluorescent lifetime quenching measurements.....</i>	101
5.2.5 <i>Single-molecule sample preparation.....</i>	101
5.2.6 <i>Single-molecule fluorescence lifetime measurements.....</i>	102
5.3 Discussion .....	103
5.3.1 <i>Comparison of single-molecule results with and without quenchers</i> ....	103
5.3.2 <i>Comparison of ensemble and single molecule results.....</i>	104
5.4 Conclusion .....	104
References .....	105
<b>Summary .....</b>	<b>107</b>
<b>Samenvatting .....</b>	<b>111</b>
<b>Curriculum Vitae .....</b>	<b>115</b>
<b>List of Publications .....</b>	<b>117</b>
<b>Acknowledgments.....</b>	<b>119</b>



# 1

## Introduction

*Optical single-molecule techniques emerged more than 30 years ago with experiments monitoring single probe molecule behavior in solids at cryogenic temperatures and extended to much higher temperatures. Single-molecule microscopy enable the imaging of biological structures such as proteins at resolutions close to the molecular scale to determine the individual molecules' behaviors and elucidation of the distribution, rather than the average.*

*Early time-resolved experiments by Frauenfelder on the ensemble of the kinetic rebinding of CO to myoglobin molecules resulted in a stretched exponential relaxation due to a very large spread of the reaction rates of individual molecules. These results were assigned to the heterogeneity in this system originated from different conformations of different single-molecule proteins and from the widely different reaction rates associated with each of these conformations. This approach marked the beginning of a new area in the physical chemistry of proteins. The research to image this heterogeneity in this system with single molecule microscopy is still missing.*

*The work presented in this thesis contains two lines of research. On the one hand, we investigate the Förster Resonance Energy Transfer (FRET) of dye labeled-carboxymyoglobin (MbCO) in the ensemble to show the feasibility of performing single molecule-FRET experiments to study the kinetic rebinding of CO to myoglobin. On the other hand, we study the Förster theory about a stretched-exponential fluorescence intensity decay under ensemble conditions for a distribution of acceptors in the vicinity of each donor; This non-exponential kinetics arise from a distribution of the exponential steps originated from different single molecules. Using single-molecule microscopy, we study the histograms of the decay rates of single fluorophore molecules (donor) in the presence of acceptors as exponential which average out as non-exponential decay in the ensemble.*

*In this introduction chapter, we briefly describe the experimental techniques we used and the main characteristics of the systems we worked with. More detailed discussions will be given in the respective chapters.*

### 1.1 Luminescence

Luminescence is any process where photons are spontaneously emitted not because of heat, in the visible, ultraviolet, or infrared spectral range.<sup>1,2</sup> Based on the process leading to the emission of the electromagnetic radiation, there are different kinds of luminescence such as photoluminescence,<sup>3,4</sup> chemiluminescence, and electroluminescence.<sup>5</sup>

Photoluminescence is one form of luminescence in which a material is first excited by electromagnetic radiation, which causes an electron from the ground state to go to a higher energy level in an atom or molecule. The excitation is followed by re-radiation.<sup>6</sup> Photoluminescence spectroscopy is widely used to characterize the optical and electronic properties of photoluminescent molecules and mostly is referred to as fluorescence spectroscopy.<sup>7</sup> As very few biomolecules are naturally fluorescent, they are generally labeled with fluorescent dyes to make them detectable.

### 1.2 Fluorescence spectroscopy

Photoluminescence can refer to either a fluorescence or a phosphorescence process. Fluorescence excitation and detection is the most common and important method in light microscopy, thanks to its high sensitivity and specificity. In fluorescence, the emitting species first absorbs an excitation photon, which brings it from its ground electronic state (usually a singlet spin state) to one of the vibrational states of an excited electronic state (usually another singlet state). The excited molecule loses excess vibrational energy through interactions with the surrounding medium, and relaxes to the lowest vibrational state of its excited electronic state. Thereafter, the excited molecule, without changing its spin, emits a photon with a longer wavelength than the excitation photon. The electronic transitions of molecules are often illustrated in an energy level diagram called the Jablonski diagram (Figure 1.1). The diagram shows the absorption process consisting of the excitation of an electron from the singlet ground state ( $S_0$ ) to one of the vibronic levels of the singlet excited state ( $S_1$ ). Then the molecule relaxes non-radiatively to the first vibrational level of the singlet excited state through the dissipation of energy towards other molecules in the environment.<sup>8,9</sup>

In phosphorescence, similar to fluorescence, the species after photon excitation emits a photon to the ground state with a longer wavelength than the excitation radiation. However, this relaxation is accompanied by a change in the electron spin in which the excited molecule goes through intersystem crossing from a singlet state ( $S_1$ , or  $S_2$ ) to a state with a different spin multiplicity, usually a triplet state ( $T$ ). This results in a longer lifetime of the excited state (milli seconds to minutes, see Figure 1.1).<sup>8-10</sup>

Some nonradiative transitions are known to occur through different mechanisms such as internal conversion (IC), intersystem crossing (ISC) (Figure 1.1), and collisional quenching. Non-radiative IC is a process in which a photoexcited molecule in a vibrational excited state relaxes to a vibrational state of a lower electronic state in a time of the order of a few ps.<sup>8,11</sup> ISC is a transition of a photoexcited molecule from its singlet excited state to a state with a different spin multiplicity (triplet state) usually on the  $\mu s$  time scale.<sup>8,12</sup> Collisional quenching is another deactivating process in which the excited state of the fluorophore loses energy by energy transfer to a quencher or by other relaxation processes induced by interactions with the surrounding molecules in the solution. In the case of quenching by species Q, the

fluorescence intensity of the fluorophore decreases according to the Stern–Volmer equation<sup>8,13,14</sup>:

$$\frac{I}{I_q} = 1 + K_{SV}[Q] = 1 + k_q \tau [Q] \quad 1.1$$

where  $I$  is and  $I_q$  are the fluorescence intensity of fluorophore in the absence and presence of the quencher,  $K_{SV}$  presents the Stern–Volmer quenching constant, and  $k_q$ ,  $\tau$ , and  $[Q]$  are the bimolecular quenching constant, the lifetime of fluorophore in the absence of quencher, and the concentration of quencher, respectively.

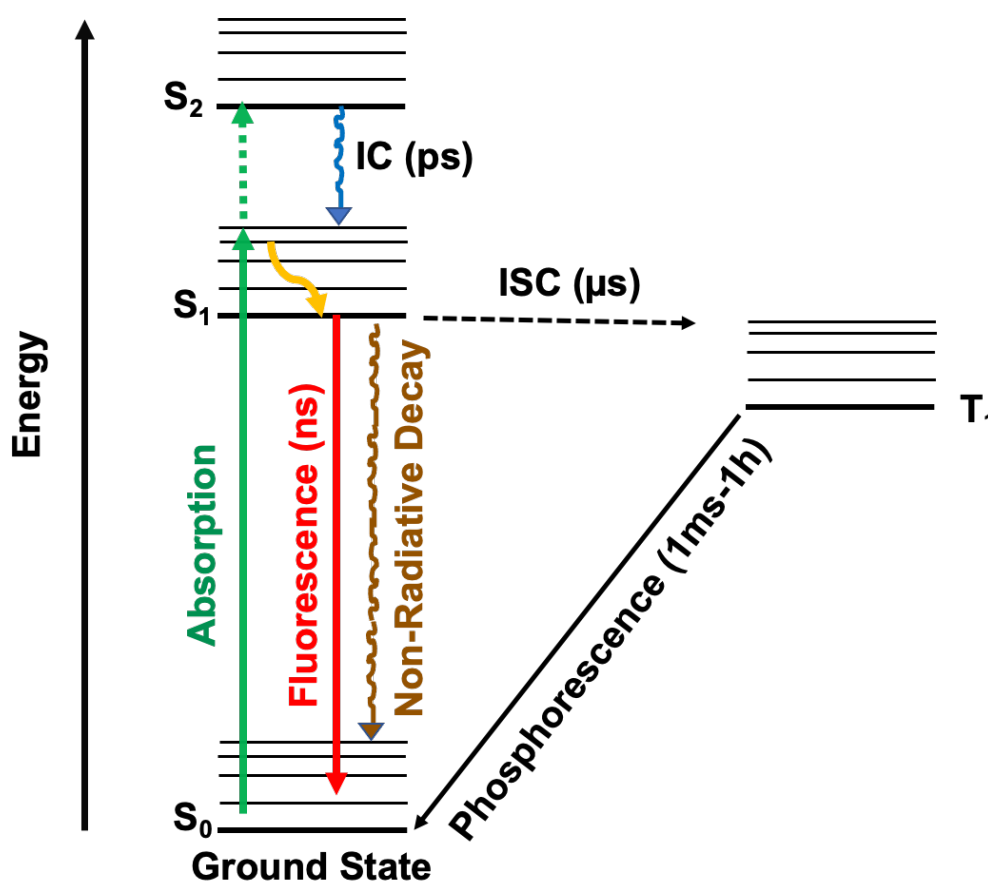


**Figure 1.1** A Jablonski diagram illustrating the following processes: light absorption including an electronic transition  $S_0 \rightarrow S_1$  (green arrow), a non-radiative transition (orange arrow), fluorescence  $S_1 \rightarrow S_0$  (red arrow), non-radiative decay (brown arrow), IC (blue arrow), ISC (dashed black arrow), and phosphorescence  $T_1 \rightarrow S_0$  (black arrow). The states involved are the singlet ground state ( $S_0$ ), singlet excited states ( $S_1$ ,  $S_2$ ) and the triplet excited state ( $T_1$ ) [modified after <sup>8</sup>].

Fluorescence is widely used in different areas particularly in cellular biochemistry and biomedicine. Fluorescence-based assays are widely used, specially in the biomedical science and allow one to discover the details of the molecular mechanisms in biological reactions. Fluorescent experiments can be performed in real-time in



ensembles and at the single- molecule level and constitute a practical tool for measuring biomolecular conformational changes, probing protein–nucleic acid interactions, etc.<sup>15–17</sup>

### 1.3 Properties of fluorophores

#### 1.3.1 Molar absorption coefficient

A well-known intrinsic property of a chemical species is its molar extinction coefficient ( $\epsilon$ ) which indicates how strongly a chemical species or substance absorbs the light at a determined wavelength. Thus, the higher extinction coefficient, the greater the amount of light being absorbed.  $\epsilon$  is constant for a specific compound at a certain wavelength under fixed conditions, for example solvent, pH and temperature. Since it is a substance-specific constant under those conditions, chemists frequently use  $\epsilon$  to measure the concentration of chemicals, e.g., proteins in solution.

The absorption process can be described by the Beer-Lambert Law:<sup>18</sup>

$$A = \epsilon bc \quad 1.2$$

where  $A$  is the absorbance,  $\epsilon$  is the molar extinction coefficient,  $b$  is the optical path length through the solution and  $c$  is the concentration of the species.

The brightness of a fluorescent molecule can be calculated from the molar extinction coefficient at the excitation wavelength and the fluorescence quantum yield as efficiency of fluorescent emission by using the following equation:<sup>19</sup>

$$\text{Brightness} = \epsilon \phi \quad 1.3$$

where  $\phi$  is the quantum yield discussed below.

Basically, the brightness depends on how strongly a fluorophore absorbs the light ( $\epsilon$ ) and how well it emits the light ( $\phi$ ). Fluorophores with a high quantum yield and extinction coefficient are the brightest.

#### 1.3.2 Quantum yield

Not all of the light absorbed by a fluorophore is completely re-emitted as light during relaxation to the ground state, because some non-radiative decay processes compete with photon emission as described in section 1.2. The fluorescence quantum yield ( $\phi$ ) is defined as the number of photons emitted by the excited fluorophore divided by the number of absorbed photons.  $\phi$  is calculated from the ratio of the radiative decay rate ( $k_r$ ) to the total fluorescence decay rate ( $k_f$ ), including radiative and non-radiative channels:<sup>20</sup>

$$\phi = \frac{k_r}{k_r + k_{nr}} \quad 1.4$$

According to the above equation, when the radiative rate ( $k_r$ ) is high and the non-radiative rate ( $k_{nr}$ ) is low,  $\phi$  will be large, whereas a non-fluorescent fluorophore has a quantum yield of zero.

The magnitude of  $k_{nr}$  depends strongly on the local environment whereas  $k_r$  is essentially determined by the electronic structure of fluorophore.

### 1.3.3 Fluorescence lifetime

When a fluorophore is photoexcited, it relaxes to the ground state through radiative and/or nonradiative pathways. The relation between the fluorescence decay rate and the fluorescence decay time is described according to: <sup>21</sup>

$$I_t = I_0 e^{-t/\tau} \quad 1.5$$

$$\frac{1}{\tau} = \sum k_i \quad 1.6$$

where  $t$  is the time,  $\tau$  the fluorescence lifetime,  $I_0$  and  $I_t$  the fluorescence intensity at time zero ( $t = 0$ ), and at time  $t$ , respectively.  $k_i$  are the decay rates for the various decay pathways, for example the radiative decay rate,  $k_r$ , or the non-radiative decay rate,  $k_{nr}$ .

These radiative and non-radiative rates determine the quantum yield, fluorescence intensity, and lifetime. The lifetime is characteristic of the electronic properties of the fluorophore but is influenced by the surrounding environment. Lifetime is the parameter that is most easily measured precisely and is least affected by the equipment.

## 1.4 Fluorescence resonance energy transfer (FRET)

FRET, first described by Theodor Förster, <sup>22</sup> is a process by which the excitation energy is transferred nonradiatively from a photoexcited donor fluorophore to an acceptor fluorophore over distances of 10-90 Å (Figure 1.2). Thus, when a chromophore is photoexcited to an excited state, instead of directly relaxing to the ground state by fluorescing, it may transfer its energy to the excited state of an acceptor chromophore in the vicinity (10-90 Å) through nonradiative dipole–dipole coupling. The efficiency of the FRET process scales with the inverse sixth power of the distance between the donor and acceptor. Thus, this technique is highly sensitive to changes in distance on the scale of Angstroms. Since energy transfer occurs through dipole–dipole coupling, the FRET efficiency also depends on the orientations of donor and acceptor dipole moments with respect to each other and to the radius vector between their centers. <sup>23</sup>

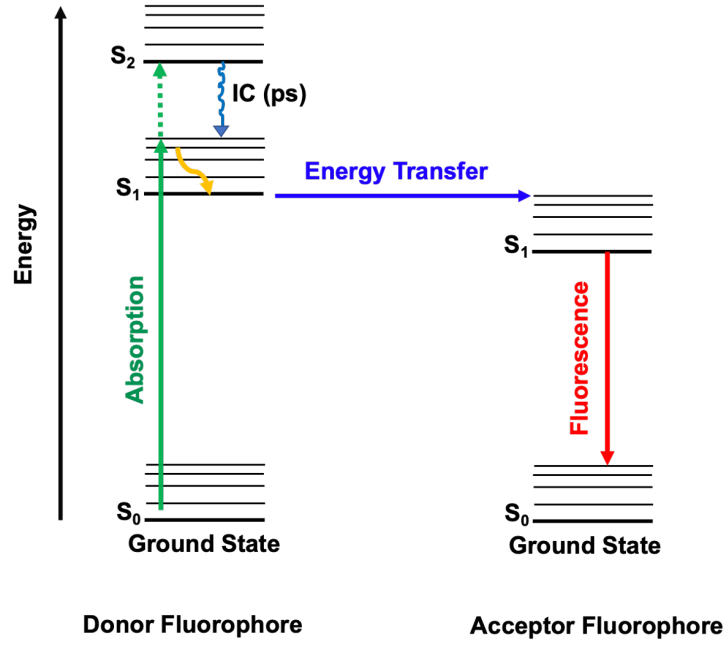


**Figure 1.2.** A Jablonski diagram illustration for FRET. The singlet ground and excited states  $S_0$ ,  $S_1$ , and  $S_2$  of the donor are shown on the left side with excitation and de-excitation pathways. On the right side of the figure, the ground state  $S_0$  and first excited state  $S_1$  of an acceptor for FRET are shown together with the energy transfer pathway from the donor  $S_1$  state to the acceptor  $S_1$  state [after <sup>8</sup>].

The FRET efficiency  $E$  is defined as the fraction of donor excitations that result in energy transfer and it is determined by the ratio of the energy transfer rate  $k_{ET}$  to the sum of all rates depopulating the excited state of the donor: <sup>23</sup>

$$E = \frac{k_{ET}}{k_{ET} + k_r + \sum k_i} \quad 1.7$$

where  $k_{ET}$  is the rate of energy transfer,  $k_r$ , the radiative decay rate of the donor,  $k_i$  the rates of any other nonradiative de-excitation pathways not involving FRET.

The Förster radius  $R_0$ , i.e. the distance at which the energy transfer efficiency is 50%, depends on the overlap of the donor emission spectrum with the acceptor absorption spectrum and on their mutual molecular orientation as expressed by the following equation: <sup>24</sup>

$$R_0 = 0.2108 \left( \frac{\phi_D \kappa^2}{n^4} \int \bar{F}_D(\lambda) \epsilon_A(\lambda) \lambda^4 d\lambda \right)^{\frac{1}{6}} \quad 1.8$$

where  $\phi_D$  is the fluorescence quantum yield of the donor in the absence of the acceptor,  $\kappa^2$  is the dipole orientation factor which can change between 0 and 4,  $n$  is the refractive index of the medium,  $\epsilon_A(\lambda)$  is the acceptor molar extinction coefficient ( $M^{-1}cm^{-1}$ ), and  $\bar{F}_D$  is the donor emission spectrum normalized to an area of 1 ( $\int_0^\infty F_D(\lambda) d\lambda = 1$ ).

As the FRET efficiency is inversely proportional to the sixth power of the distance between donor and acceptor chromophores, it is possible to measure small changes in this distance. FRET has emerged as a powerful fluorescent spectroscopic technique in cell biochemistry and biophysics to measure structural dynamics, kinetics, and for mapping the conformations of biomolecules in complex systems.

### 1.4.1 Distance between donor and acceptor

As mentioned before, the energy transfer efficiency ( $E$ ) depends inversely on the 6th power of the distance between the donor and acceptor ( $r$ ), due to the dipole–dipole coupling mechanism (Figure 1.3 A): <sup>24</sup>

$$E = \frac{1}{1 + \left(\frac{r}{R_0}\right)^6} \quad 1.10$$

According to this equation, any event or process that alters the distance between donor and acceptor will strongly change the energy transfer rate and allow one to observe biomolecular conformational changes in a time range of ps-ms on a nanometer scale by measuring the resonance energy transfer.

Based on the Eq. 1.8, due to the  $\lambda^4$  dependence of the overlap integral, small shifts in the spectra can have large effects on the  $R_0$ . The following sections describe two factors: the overlap integral and the orientation factor ( $\kappa^2$ ), that influence  $R_0$  and the FRET efficiency.

### 1.4.2 The overlap integral

The rate of energy transfer depends on how well the donor emission spectra and acceptor absorption spectra overlap (Figure 1.3B). <sup>24</sup>

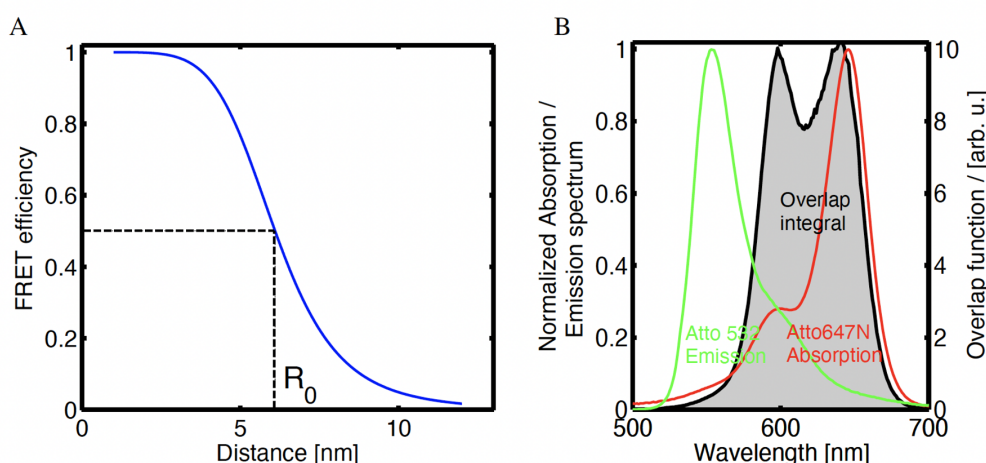


**Figure 1.3 (A)** Dependence of the FRET efficiency on the distance between the donor (Atto 532) and acceptor fluorophores (Atto 647N). For this donor-acceptor pair, the calculated Förster radius is  $R_0 = 6.1$  nm, at which distance the FRET efficiency ( $E$ ) is 50%. **(B)** The grey colour area is a visualization of the overlap between the emission spectrum of donor (Atto 532, green colour) and acceptor emission spectra (Atto 647N, red colour). The overlap integral is proportional to the area under this curve (gray area), based on equation 1.8 (as  $\int \bar{F}_D(\lambda) \epsilon_A(\lambda) \lambda^4 d\lambda$ ). <sup>25</sup>

The phenomenon of fluorescence resonance energy transfer does not require the acceptor to be fluorescent. In this case, after excitation of the donor the donor fluorescence is quenched by the acceptor and the fluorescence intensity and lifetime of the donor will change. (Figure 1.4B).

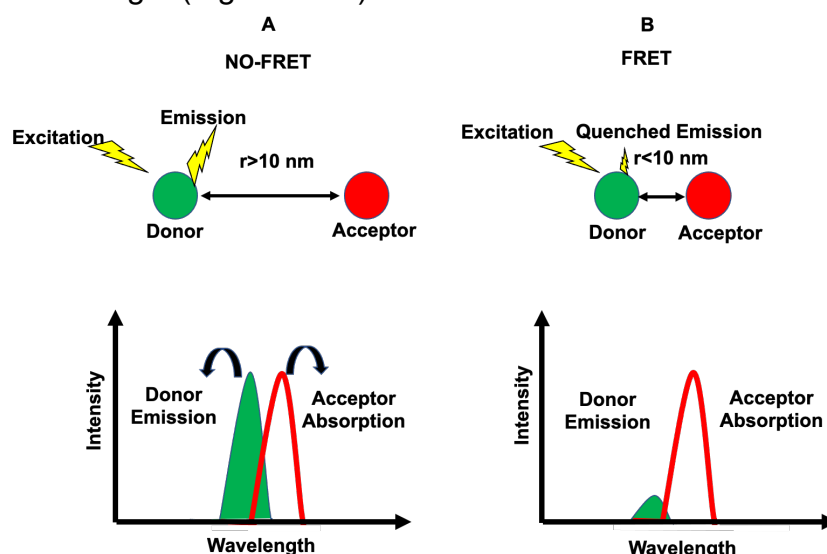


**Figure 1.4** Schematic of FRET in the presence of a non-fluorescent quenching acceptor (A) describes No FRET because of  $r > 10 \text{ nm}$ , (B) FRET occurs ( $r < 10 \text{ nm}$ ) after excitation of donor. The fluorescence emission of the donor is quenched by the acceptor. The acceptor does not fluoresce but the intensity and lifetime of the donor change. The donor and acceptor shown in green and red colours respectively.

In most applications, however, both donor and acceptor are fluorescent, and in most cases, the energy transfer occurs through quenching of the donor fluorescence and a reduction of the donor fluorescence lifetime, and an increase in the intensity of the acceptor fluorescence (Figure 1.5B).

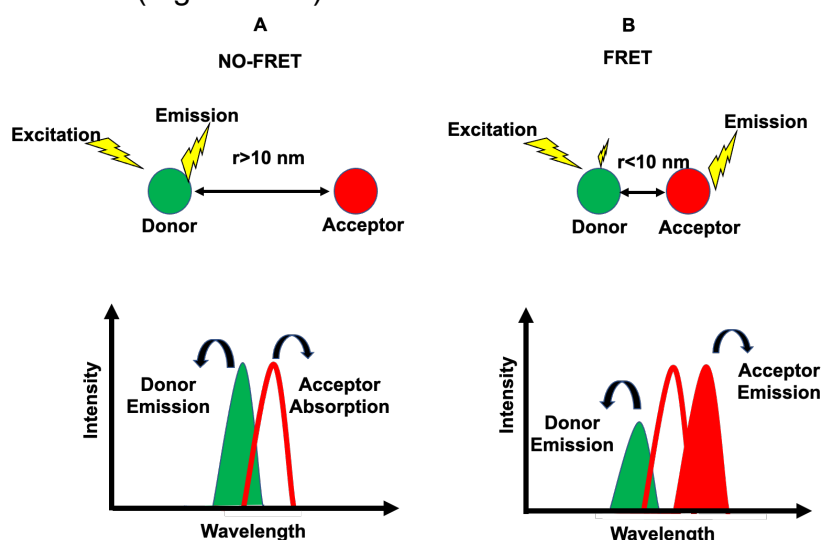


**Figure 1.5** Schematic of FRET in the presence of a fluorescent quenching acceptor (A) describes No FRET because of  $r > 10 \text{ nm}$ , (B) FRET occurs ( $r < 10 \text{ nm}$ ) after excitation of donor. The energy is transferred from donor to the acceptor. In this case, both donor and acceptor are fluorescent. Donor and acceptor have been shown in green and red colours respectively.

### 1.4.3 The orientation factor $\kappa^2$

Since energy transfer occurs through dipole–dipole coupling, the FRET efficiency also depends on the orientations of donor and acceptor dipole moments with respect to each other and to the radius vector between their centers.

The orientation factor ( $\kappa^2$ ) depends on how the donor emission dipole and the acceptor absorption dipole are oriented relative to each other.  $\kappa^2$  can range from zero to 4, however, it is typically assumed to be the dynamically averaged value of  $2/3$  (0.67) (Figures 1.6A).

When the donor emission dipole and the acceptor absorption dipole are parallel and they are perpendicular to the donor-acceptor radius vector, the value of  $\kappa^2$  is 1 (Figure 1.6B), whereas for perpendicular transition moments of donor and acceptor in the same spatial disposition,  $\kappa^2$  is zero (Figures 1.6 C). The  $\kappa^2$  factor has a maximum value of 4 when the dipoles are parallel and lie along the radius vector.<sup>26</sup>

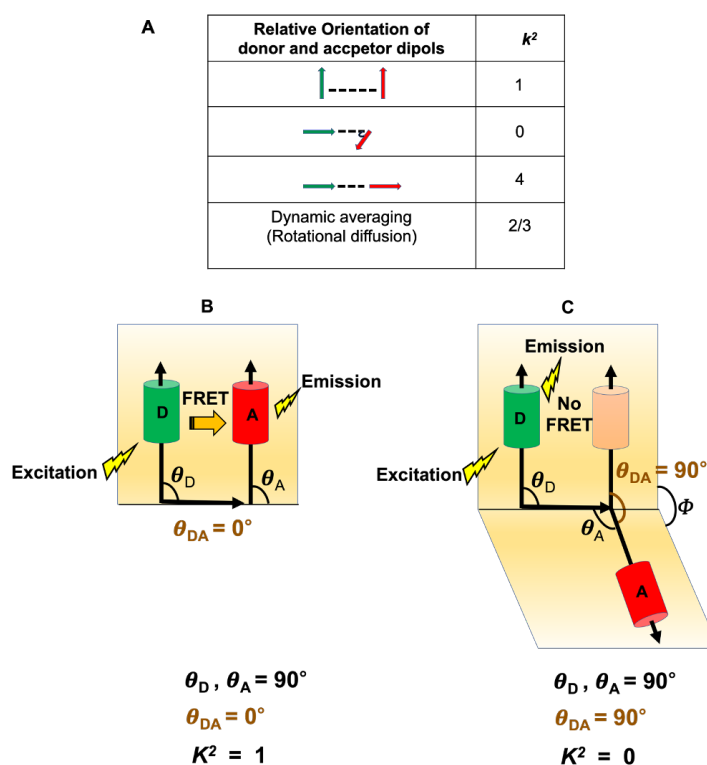


**Figure 1.6** The orientation factor  $\kappa^2$  (A) The various orientations of the donor-acceptor dipoles. (B) example where the donor emission dipole and the acceptor absorption dipole are parallel, and (C) where the donor emission dipole and the acceptor absorption dipole are perpendicular relative to the molecular connection radius vector. The donor (green) emission dipole D and the acceptor (red) absorption dipole A, and the vector connecting the donor emission and acceptor absorption dipoles are shown by the black arrows. The angles  $\theta_D$  and  $\theta_A$  are the angles between the line connecting the dipoles and the dipoles D and A, respectively.  $\theta_{DA}$  is the angle between the emission transition dipole of the donor (purple) and the absorption transition dipole of the acceptor (when the distance is zero), and  $\phi$  is the angle between the planes containing the two transition dipoles (planes shown in yellow) [after <sup>27</sup>].

The dependence of the orientation factor ( $\kappa$ -squared) on the relative orientations of the donor emission dipole and the acceptor absorption dipole (illustrated in Figure 1.6A) is given by the equation: <sup>27,28</sup>

$$\kappa^2 = (\cos\theta_{DA} - 3\cos\theta_D\cos\theta_A)^2 = (\sin\theta_D\sin\theta_A\cos\Phi - 2\cos\theta_D\cos\theta_A)^2 \quad 1.11$$

where  $\theta_{DA}$  is the angle between the emission transition dipole of the donor and the absorption transition dipole of the acceptor,  $\theta_D$  and  $\theta_A$  are the angles between these dipoles and the radius vector joining the donor and acceptor, and  $\Phi$  is the angle between the planes containing the two transition dipoles.

## 1.5 Ensemble and single-molecule spectroscopy

Ensemble fluorescent assays from a homogeneous sample provide a value for the experimental observables that depend on the molecular properties of the sample. However, fluorescence spectroscopy of a non-homogeneous ensemble sample that consists of several different subpopulations similarly reports an average value of the molecular parameters, which depends on the nature of the heterogeneity. In a non-homogeneous ensemble sample, each molecule has a different environment, and interaction. Thus each individual molecule behaves differently and ensemble fluorescence assays only report the mean value of the fluorescent measurement and do not give any information about individual molecules. <sup>27,29</sup>

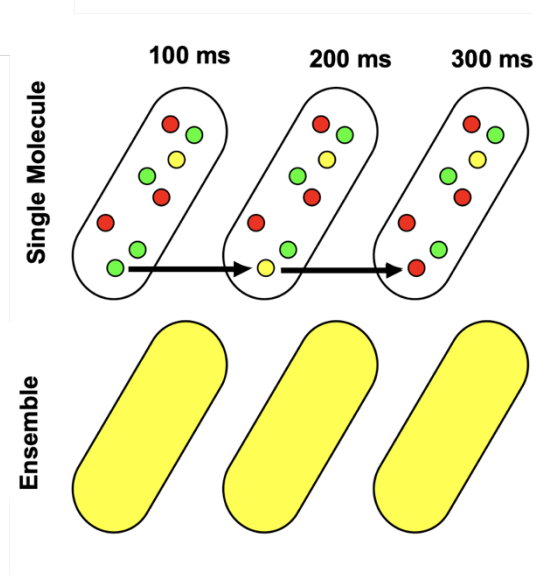


**Figure 1.7** A scheme illustrating the difference between single-molecule (top) and ensemble detection (bottom) for the static and dynamic heterogeneities in a sample. In this illustration, a biomolecule has, for instance, three different states depicted in the three colors: red, yellow, and green (static heterogeneity) and biomolecules can interconvert between these three states every 100-ms (dynamic heterogeneity). Single-molecule techniques can detect and distinguish both static heterogeneity and dynamic heterogeneity, whereas ensemble techniques only measure average values

A fundamental advantage of smFRET (single-molecule FRET) is its ability to resolve sample heterogeneity and to provide distributions of quantities related to the different subpopulations in the sample. For example, in an ensemble, it is impossible to detect the dynamic switching of a protein between different states over the course of the experiment, but it can be measured by smFRET. Single-molecule spectroscopy has several known advantages: a high sensitivity to nano-meter distances (1-10 nm), the ability to measure a single molecule, the ability to measure structural and dynamic heterogeneities, and a high sensitivity and specificity to the labelled molecules, because only the fluorescence signal of label molecules is detected, even in a crowded environment.<sup>24</sup>

## 1.6 Confocal microscopy

Although the number of single-molecule methods is continuously increasing and each of them has specific advantages and disadvantages, detection of single molecules with a confocal microscope makes the observation of individual molecules possible with a simple setup.<sup>30</sup> Confocal microscopy was invented by Marvin Minsky in the late 1950s.<sup>31</sup> His confocal setup was made of a lamp, a pinhole, a lens, and a detector. The principle of a confocal microscope is to produce a point source of light in a focal plane and reject all photons from the out-of-focus planes to increase the optical resolution and the image contrast. Figure 1.8 demonstrates a general confocal setup in which the excitation photons from a laser are sent to a single spot in the sample through an objective. The fluorescence photons emitted by the sample are transmitted by a dichroic mirror, focused by suitable lenses, pass through a pinhole positioned so that only photons from the objective's focus pass whereas photons emitted by out-of-focus planes are mostly rejected. Photons from the in-focus excitation point finally reach the detector after spectral filtering by a long-pass fluorescence filter. By raster-scanning the focal plane, one obtains a fluorescence image. Technological advances have increased the sensitivity and lowered the pixel dwell times in confocal microscopy, making it today an ideal tool for fluorescence microscopy.<sup>32</sup>

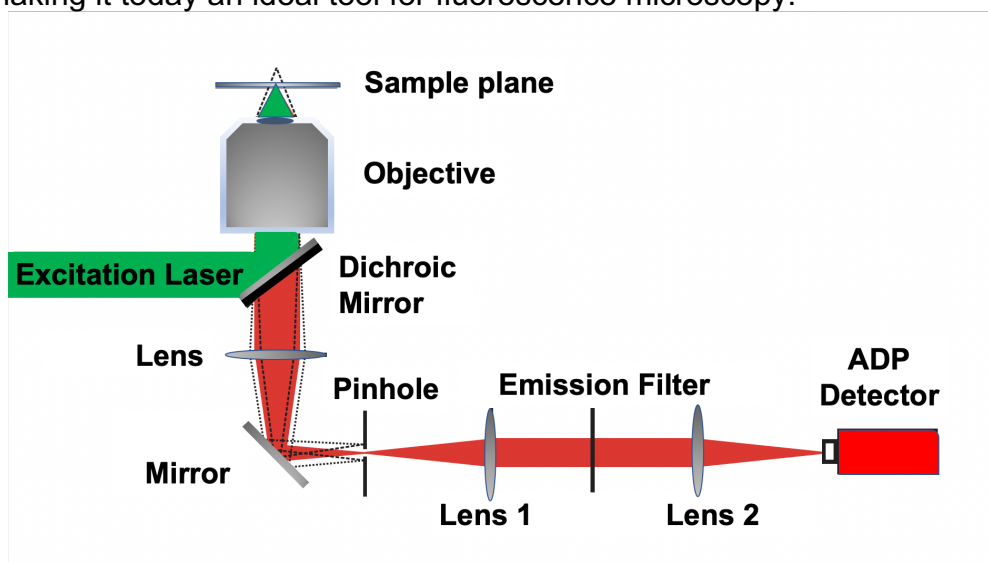


**Figure 1.8** Schematic of a general confocal setup. The laser sends excitation photons (green) into the objective by a dichroic mirror. Fluorescence light (red) emitted from the plane of sample arrive at a pinhole and only the photons emitted from the focus of the objective pass through and reach the detector, an avalanche photodiode (APD) in this case [modified after <sup>25</sup>].



### 1.6.1 Time-Correlated Single-Photon Counting (TCSPC)

It is essential for fluorescence lifetime measurements to determine the exact arrival time of individual fluorescence photons. TCSPC is a tool to precisely record the arrival time of each photon upon excitation by a laser pulse. The laser has a high repetition rate (around 80 MHz) and delivers short pulsed (ps) pulses. APDs produce one electrical pulse for each detected photon. The fluorescence decay profile is obtained based on the detection at a multitude of single photon events, which are collected over many cycles. The synchronization is controlled by the laser driver “Sepia I”.<sup>33</sup>

## 1.7 Proteins

Proteins are known as essential molecular machines in the cells which are responsible for many vital functions. Such proteins as enzymes, hormone receptors, regulatory and transport proteins, are indispensable key molecules in such vital processes as immunity, circulation, and homeostasis. In 1838, Gerardus Mulder was the first who introduced the word protein in his publication and he defined it as: “The *name protein that I propose for the organic oxide of fibrin and albumin, I wanted to derive from Greek word proteios, because it appears to be the primitive or principal substance of animal nutrition*”.<sup>34</sup>

Proteins are complex polymers made of monomeric amino-acid units linked together. A protein chain is a sequence of amino-acids taken out of 20 different compounds, and arranged in a specific order. Which amino-acid comes next upon protein synthesis is determined by a codon of three nucleotides in the DNA or RNA of the cell coding for that protein. The number of amino acids in a protein varies from 50 to more than 30,000 amino-acids. Macromolecules which have less than 50 amino acids are called peptides.

The structure of a protein determines its function in the living organism. Importantly, the conditions in the surroundings of a protein, such as pH, temperature, and salt concentration, have a direct effect on the protein structure and consequently on the protein function. One distinguishes four levels in the structure of proteins: primary structure, secondary structure, tertiary structure and quaternary structure.<sup>34</sup>

### 1.7.1 Primary Structure

The chemistry of amino acid side chains is important in the formation of protein structure. In general, an amino acid consists of an alpha carbon ( $C_\alpha$ ) bound to three different substituents comprising an amine (via a nitrogen atom), a carboxylic carbon (via a carbon atom), and a hydrogen (Figure 1.9).<sup>35</sup>

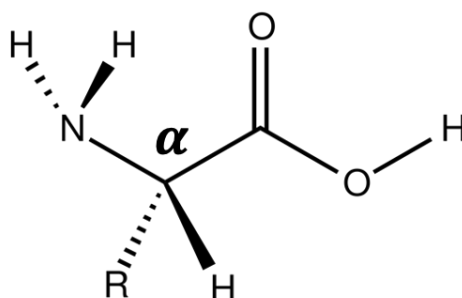


**Figure 1.9** Chemical structure of an amino-acid.<sup>35</sup>

The reaction between two amino-acids in which the carboxylic group of an upstream amino-acid (Figure 1.9A left) and the amine group of a downstream amino-acid (Figure 1.10 A, right) condense by losing a water molecule, results in the formation of a peptide bond (Figure 1.10B). Polypeptides are formed by successive dehydration reactions between successive amino-acids (Figure 1.10C). The primary structure is constituted by this specific sequence of amino-acids bound by peptide bonds into a polypeptide chain (Figure 1.10 D).

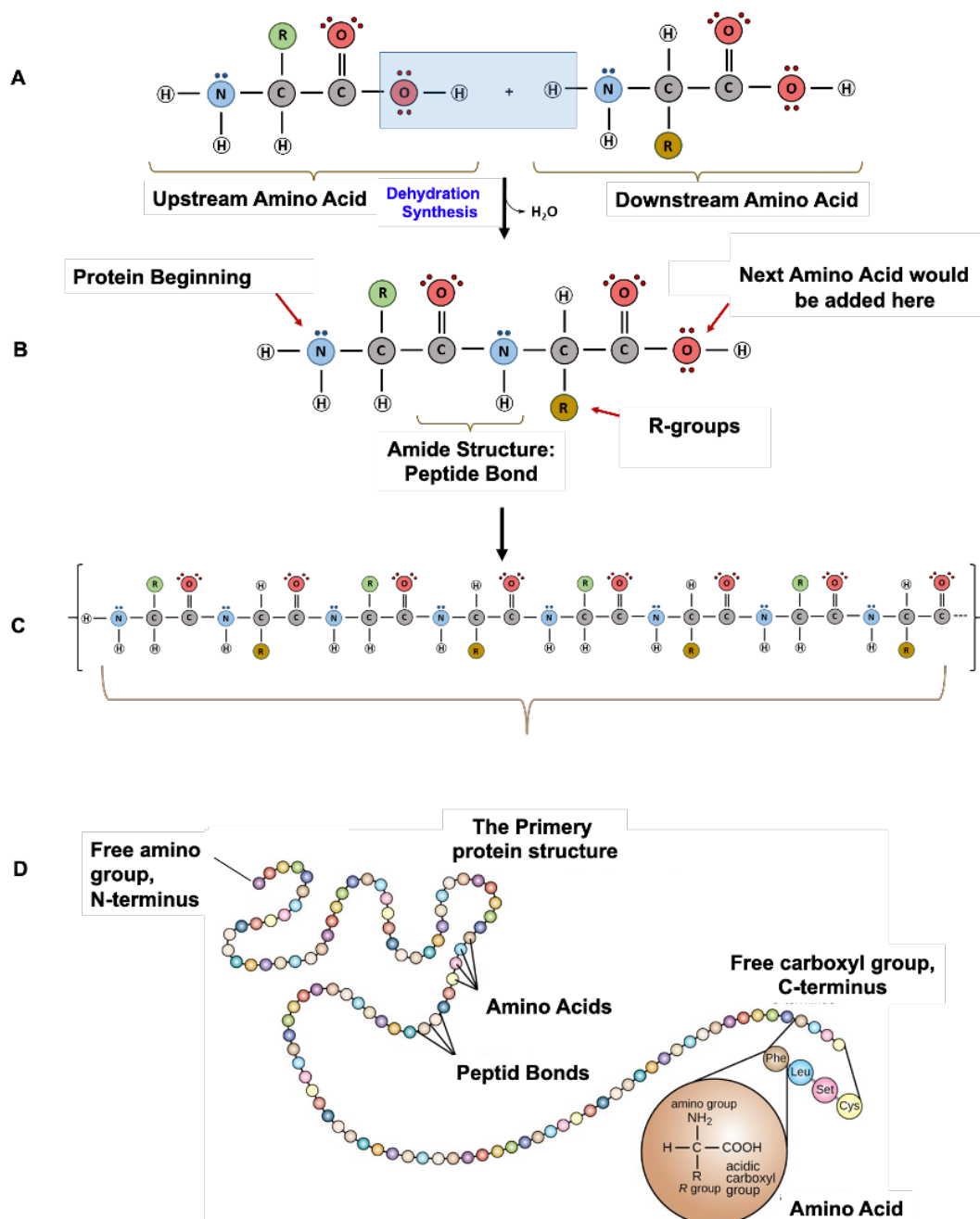


**Figure 1.10 Formation of the primary protein structure (A-D).** The dehydration reaction between two amino-acids form a peptide bond and successive dehydration steps produce a polypeptide with the primary protein structure [modified after <sup>36</sup>]



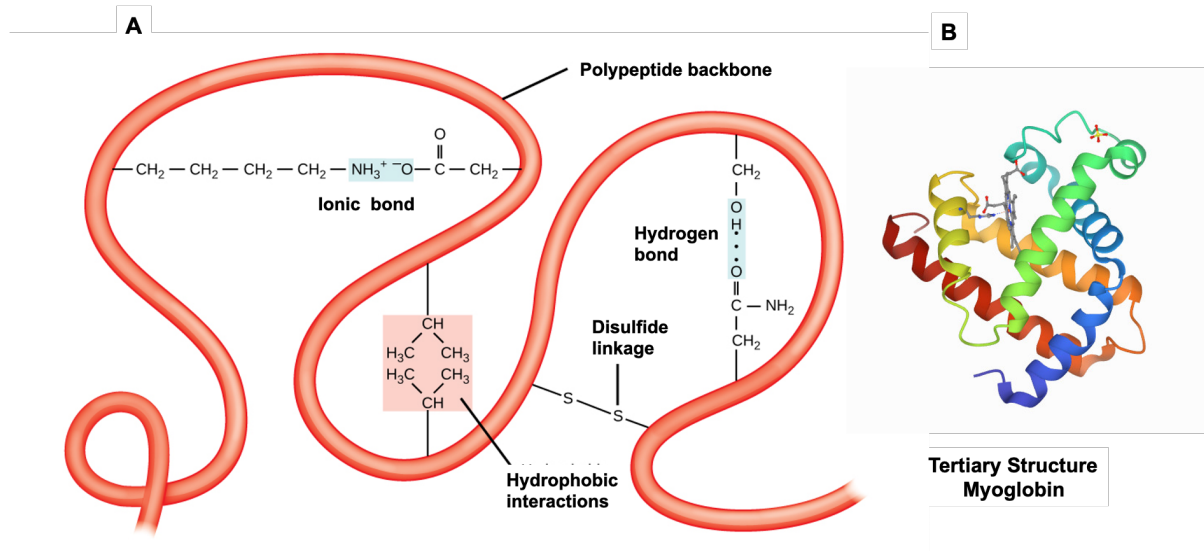


**Figure 1.12** (A) The tertiary structure of proteins forms from different kinds of chemical interactions between polypeptide backbone residues such as hydrophobic interactions, ionic interactions, hydrogen bonding and disulfide bridges [modified after <sup>39</sup>], (B) Tertiary structure of Myoglobin protein from Protein Data Bank (PDB:1VXA)

### 1.7.4 Quaternary Structure

While many proteins consist of only a single poly-peptide chain, some consist of multi-chains. The interaction and linking of two or more motifs of tertiary protein structure gives rise to the quaternary structure. Hemoglobin is a well-known protein with a quaternary structure constituted of four myoglobin-like (tertiary structure) subunits and an heme group which contains iron. Two subunits are designated as alpha, and the two other chains are called beta (Figure 1.13 A-B). <sup>40</sup>

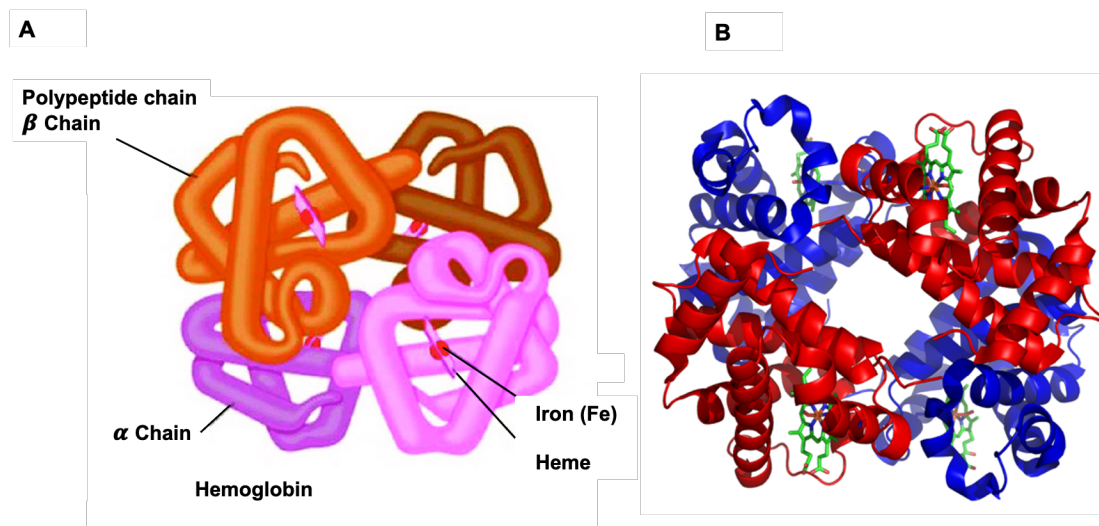


**Figure 1.13** (A) Illustration of the quaternary structure of the hemoglobin protein constituted of four subunits [after <sup>41</sup>] (B) Quaternary structure of human hemoglobin with  $\alpha$  and  $\beta$  subunits, colored in red and blue, respectively, and four heme groups in green from PDB: 1GZX Proteopedia Hemoglobin.

## 1.8 FRET in proteins

Labeling of a protein with specific fluorophores at specific sites enables measurements of structural changes of the protein in solution through FRET. In this well-known method, the protein is labeled with two fluorophores, one of them acts as an energy donor and the other one accepts the transferred energy from donor (Figure 1.14). The conformational changes within a protein have a significant effect on the distance between donor and acceptor molecules and therefore on their interaction, resulting in variations of the FRET efficiency. Because the FRET efficiency is extremely sensitive to the separation distance between donor and acceptor fluorophores, a given value of the efficiency can be assigned to a specific conformation of the protein.

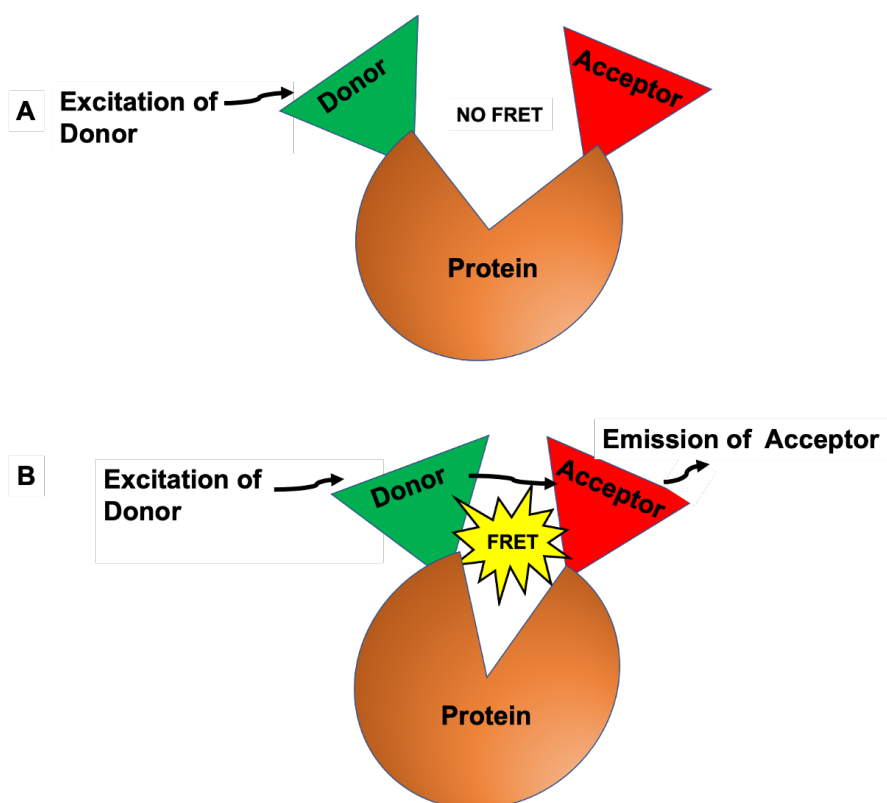


**Figure 1.14** Schematics of FRET in a doubly-labeled protein in which a donor (green) and an acceptor (red) fluorophore are attached to the same protein. The FRET interaction enables studies of conformational changes of the molecule. (A) Upon a conformational change, the distance between donor and acceptor fluorophores attached to the protein becomes  $r > 10$  nm, thus no energy transfer takes place. (B) Upon a conformational change, the distance between donor and acceptor fluorophores attached to the protein becomes  $r < 10$  nm and, upon excitation of the donor fluorophore, FRET occurs [after <sup>42</sup>].

The resonance energy transfer can also occur towards a non-fluorescent acceptor, for example towards a non-fluorescent absorbing metal center in a protein or towards a non-fluorescent dye attached to the protein (Figure 1.15).



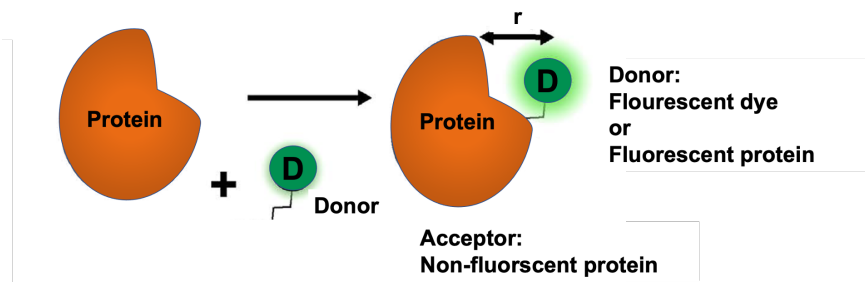


**Figure 1.15** Schematics of FRET in one labeled **protein** in which a fluorescent dye/or a fluorescent protein act as donor (green) attached to an absorbing but non-fluorescent protein as acceptor (orange). When  $r < 10$  nm, FRET occurs and fluorescent emission of donor is quenched by the absorption through the protein acceptor.

Resonance energy transfer can thus occur between a fluorescent protein (donor) and myoglobin as nonfluorescent acceptor. For example Myoglobin-mCherry is a FRET-based probe in which the mCherry fluorescent protein (as donor) is attached to the non-fluorescent myoglobin (as acceptor)<sup>43</sup> [Fig. 1.16].

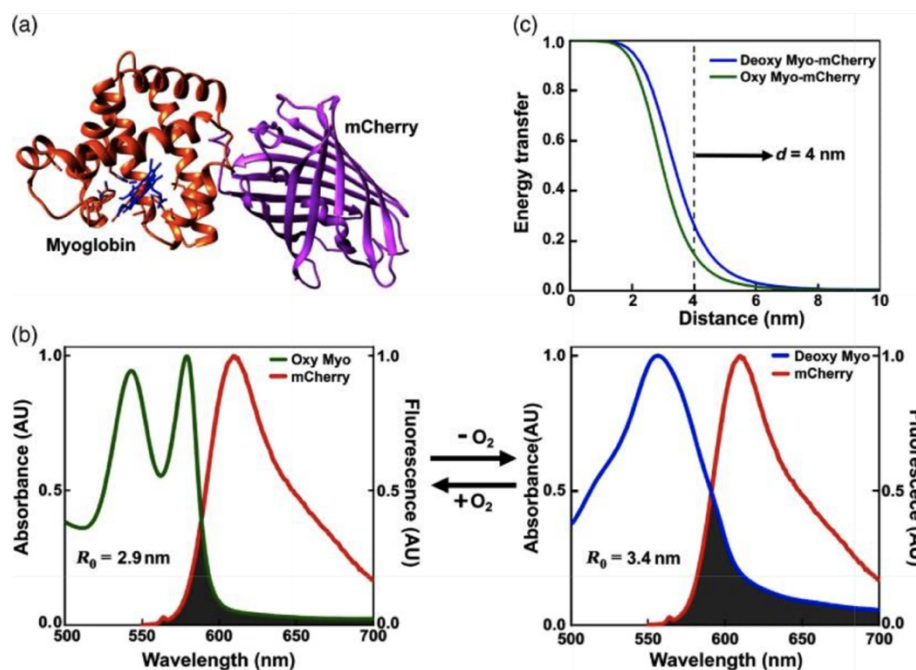


**Figure 1.16** Myoglobin-mCherry as a FRET-based probe in which the mCherry fluorescent protein (as donor, right side) is attached to the non-fluorescent myoglobin (as acceptor, left side), (B, left side) The absorption spectrum of oxymyoglobin in which myoglobin is bound to oxygen (green curve) overlaps with the emission spectrum of mCherry (red curve) and (B, right side) the absorption spectrum of deoxy-myoglobin in which myoglobin is unbound to oxygen (blue curve) overlaps with the emission spectrum of mCherry (red curve), Basically the spectral overlap between donor and acceptor is different when  $O_2$  is bound (left side) and when  $O_2$  is unbound (right side). (C) The distance between donors (oxymyoglobin/deoxy-myoglobin) and acceptor (mCherry) is estimated to  $\sim 4$  nm by using the Protein Data Bank (PDB).<sup>43</sup>

When O<sub>2</sub> is bound to myoglobin, forming oxymyoglobin as the acceptor, the spectral overlap of donor with the mCherry as the donor is significantly less than when O<sub>2</sub> is unbound to myoglobin (deoxy-myoglobin). Therefore, the mCherry's fluorescence is quenched when O<sub>2</sub> is unbound and its fluorescence intensity increases significantly when O<sub>2</sub> is bound to myoglobin. It should be noted that the distance between the two proteins (donor-acceptor) is defined by the linker that connects them. Thus, the FRET probe presented here is on the basis of the changes in the spectral features of the energy acceptor and not based on the distance changes between the donor and acceptor.

## References

- (1) Obodovskiy, I. Chapter 12 - Luminescence. In *Radiation*; Obodovskiy, I., Ed.; Elsevier, 2019; pp 207–220.
- (2) Gao, R.; S. Kodaimati, M.; Yan, D. Recent Advances in Persistent Luminescence Based on Molecular Hybrid Materials. *Chem. Soc. Rev.* **2021**, 50 (9), 5564–5589.
- (3) Yang, B.; Chen, G.; Ghafoor, A.; Zhang, Y.; Zhang, Y.; Zhang, Y.; Luo, Y.; Yang, J.; Sandoghdar, V.; Aizpurua, J.; Dong, Z.; Hou, J. G. Sub-Nanometre Resolution in Single-Molecule Photoluminescence Imaging. *Nat. Photonics* **2020**, 14 (11), 693–699.
- (4) Sun, C.; Yang, J.; Li, L.; Wu, X.; Liu, Y.; Liu, S. Advances in the Study of Luminescence Probes for Proteins. *J. Chromatogr. B Analyt. Technol. Biomed. Life. Sci.* **2004**, 803 (2), 173–190.
- (5) Srisomwat, C.; Yakoh, A.; Avihingsanon, A.; Chuaypen, N.; Tangkijvanich, P.; Vilaivan, T.; Chailapakul, O. An Alternative Label-Free DNA Sensor Based on the Alternating-Current Electroluminescent Device for Simultaneous Detection of Human Immunodeficiency Virus and Hepatitis C Co-Infection. *Biosens. Bioelectron.* **2022**, 196, 113719.
- (6) Photoluminescence. *Wikipedia*; 2022.
- (7) Sinkeldam, R. W.; Greco, N. J.; Tor, Y. Fluorescent Analogs of Biomolecular Building Blocks: Design, Properties and Applications. *Chem. Rev.* **2010**, 110 (5), 2579–2619.
- (8) Principles of Fluorescence Spectroscopy - Joseph R. Lakowicz - Google Boeken [https://books.google.nl/books/about/Principles\\_of\\_Fluorescence\\_Spectroscopy.html?id=3QKTAQAACAAJ&redir\\_esc=y](https://books.google.nl/books/about/Principles_of_Fluorescence_Spectroscopy.html?id=3QKTAQAACAAJ&redir_esc=y) (accessed 2022 -04 -01).
- (9) Omary, M. A.; Patterson, H. H. Luminescence, Theory. In *Encyclopedia of Spectroscopy and Spectrometry*; Elsevier, 2017; pp 636–653.
- (10) Theory and Calculation of the Phosphorescence Phenomenon | Chemical Reviews <https://pubs.acs.org/doi/10.1021/acs.chemrev.7b00060> (accessed 2022 -04 -01).

- (11) Litvinenko, K. L.; Webber, N. M.; Meech, S. R. Internal Conversion in the Chromophore of the Green Fluorescent Protein: Temperature Dependence and Isoviscosity Analysis. *J. Phys. Chem. A* **2003**, *107* (15), 2616–2623.
- (12) Marian, C. M. Spin–Orbit Coupling and Intersystem Crossing in Molecules. *WIREs Comput. Mol. Sci.* **2012**, *2* (2), 187–203.
- (13) Gehlen, M. H. The Centenary of the Stern-Volmer Equation of Fluorescence Quenching: From the Single Line Plot to the SV Quenching Map. *J. Photochem. Photobiol. C Photochem. Rev.* **2020**, *42*, 100338.
- (14) Tanwar, A. S.; Parui, R.; Garai, R.; Chanu, M. A.; Iyer, P. K. Dual “Static and Dynamic” Fluorescence Quenching Mechanisms Based Detection of TNT via a Cationic Conjugated Polymer. *ACS Meas. Sci. Au* **2022**, *2* (1), 23–30.
- (15) Tinoco, I.; Gonzalez, R. L. Biological Mechanisms, One Molecule at a Time. *Genes Dev.* **2011**, *25* (12), 1205–1231.
- (16) Harroun, S. G.; Lauzon, D.; Ebert, M. C. C. J. C.; Desrosiers, A.; Wang, X.; Vallée-Bélisle, A. Monitoring Protein Conformational Changes Using Fluorescent Nano-antennas. *Nat. Methods* **2022**, *19* (1), 71–80.
- (17) Hwang, H.; Myong, S. Protein Induced Fluorescence Enhancement (PIFE) for Probing Protein-Nucleic Acid Interactions. *Chem. Soc. Rev.* **2014**, *43* (4), 1221–1229.
- (18) Swinehart, D. F. The Beer-Lambert Law. *J. Chem. Educ.* **1962**, *39* (7), 333.
- (19) Tian, Y.; Halle, J.; Wojdyr, M.; Sahoo, D.; Scheblykin, I. G. Quantitative Measurement of Fluorescence Brightness of Single Molecules. *Methods Appl. Fluoresc.* **2014**, *2* (3), 035003.
- (20) Crosby, G. A.; Demas, J. N.; Callis, J. B. Absolute Quantum Efficiencies. *J. Res. Natl. Bur. Stand. Sect. Phys. Chem.* **1972**, *76A* (6), 561–577.
- (21) Fluorescence Lifetime Measurements and Biological Imaging | Chemical Reviews <https://pubs.acs.org/doi/10.1021/cr900343z> (accessed 2022 -04 -01).
- (22) Förster, Th. Zwischenmolekulare Energiewanderung und Fluoreszenz. *Ann. Phys.* **1948**, *437* (1–2), 55–75.
- (23) Lee, S.; Lee, J.; Hohng, S. Single-Molecule Three-Color FRET with Both Negligible Spectral Overlap and Long Observation Time. *PloS One* **2010**, *5* (8), e12270.
- (24) Lerner, E.; Barth, A.; Hendrix, J.; Ambrose, B.; Birkedal, V.; Blanchard, S. C.; Börner, R.; Sung Chung, H.; Cordes, T.; Craggs, T. D.; Deniz, A. A.; Diao, J.; Fei, J.; Gonzalez, R. L.; Gopich, I. V.; Ha, T.; Hanke, C. A.; Haran, G.; Hatzakis, N. S.; Hohng, S.; Hong, S.-C.; Hugel, T.; Ingargiola, A.; Joo, C.; Kapanidis, A. N.; Kim, H. D.; Laurence, T.; Lee, N. K.; Lee, T.-H.; Lemke, E. A.; Margeat, E.; Michaelis, J.; Michalet, X.; Myong, S.; Nettels, D.; Peulen, T.-O.; Ploetz, E.; Razvag,



- Y.; Robb, N. C.; Schuler, B.; Soleimaninejad, H.; Tang, C.; Vafabakhsh, R.; Lamb, D. C.; Seidel, C. A.; Weiss, S. FRET-Based Dynamic Structural Biology: Challenges, Perspectives and an Appeal for Open-Science Practices. *eLife* **2021**, *10*, e60416.
- (25) Sikor, M. Single-molecule fluorescence studies of Protein Folding and Molecular Chaperones. Text.PhDThesis, Ludwig-Maximilians-Universität München, 2011.
- (26) Stryer, L. Fluorescence Energy Transfer as a Spectroscopic Ruler. *Annu. Rev. Biochem.* **1978**, *47* (1), 819–846.
- (27) Ishikawa-Ankerhold, H. C.; Ankerhold, R.; Drummen, G. P. C. Advanced Fluorescence Microscopy Techniques—FRAP, FLIP, FLAP, FRET and FLIM. *Molecules* **2012**, *17* (4), 4047–4132.
- (28) Sustarsic, M.; Kapanidis, A. N. Taking the Ruler to the Jungle: Single-Molecule FRET for Understanding Biomolecular Structure and Dynamics in Live Cells. *Curr. Opin. Struct. Biol.* **2015**, *34*, 52–59.
- (29) Pradhan, B.; Engelhard, C.; Mulken, S. V.; Miao, X.; Canters, G. W.; Orrit, M. Single Electron Transfer Events and Dynamical Heterogeneity in the Small Protein Azurin from *Pseudomonas Aeruginosa*. *Chem. Sci.* **2020**, *11* (3), 763–771.
- (30) Elliott, A. D. Confocal Microscopy: Principles and Modern Practices. *Curr. Protoc. Cytom.* **2020**, *92* (1), e68.
- (31) Marvin, M. Microscopy Apparatus. US3013467A, December 19, 1961.
- (32) Reilly, W. M.; Obara, C. J. Advances in Confocal Microscopy and Selected Applications. *Methods Mol. Biol. Clifton NJ* **2021**, *2304*, 1–35.
- (33) Wahl, M. Time-Correlated Single Photon Counting. 14.
- (34) Murray, J. E.; Laurieri, N.; Delgoda, R. Proteins. In *Pharmacognosy*; Elsevier, 2017; pp 477–494.
- (35) Amino Acid. *Wikipedia*; 2022.
- (36) Chapter 2: Protein Structure – Chemistry <https://wou.edu/chemistry/courses/online-chemistry-textbooks/ch450-and-ch451-biochemistry-defining-life-at-the-molecular-level/chapter-2-protein-structure/> (accessed 2022 -04 -01).
- (37) Kamtekar, S.; Schiffer, J. M.; Xiong, H.; Babik, J. M.; Hecht, M. H. Protein Design by Binary Patterning of Polar and Nonpolar Amino Acids. *Science* **1993**, *262* (5140), 1680–1685.
- (38) File:Secondary.jpg - The School of Biomedical Sciences Wiki <https://teaching.ncl.ac.uk/bms/wiki/index.php/File:Secondary.jpg> (accessed 2022 -04 -01).

- (39) Rehman, I.; Kerndt, C. C.; Botelho, S. Biochemistry, Tertiary Protein Structure. In *StatPearls*; StatPearls Publishing: Treasure Island (FL), 2022.
- (40) Smith, A. M. CHAPTER 1 Interaction of Metal Ions with Proteins as a Source of Inspiration for Biomimetic Materials. **2015**, 1–31.
- (41) Figure 2-Structure of hemoglobin showing its alpha and beta subunits... [https://www.researchgate.net/figure/Structure-of-hemoglobin-showing-its-alpha-and-beta-subunits-and-the-heme-moiety-Source\\_fig1\\_221925240](https://www.researchgate.net/figure/Structure-of-hemoglobin-showing-its-alpha-and-beta-subunits-and-the-heme-moiety-Source_fig1_221925240) (accessed 2022 -04 -01).
- (42) Patel, M. J.; Yilmaz, G.; Bhatia, L.; Biswas-Fiss, E. E.; Biswas, S. B. Site-Specific Fluorescence Double-Labeling of Proteins and Analysis of Structural Changes in Solution by Fluorescence Resonance Energy Transfer (FRET). *MethodsX* **2018**, 5, 419–430.
- (43) Penjweini, R.; Andreoni, A.; Rosales, T.; Kim, J.; Brenner, M. D.; Sackett, D. L.; Chung, J. H.; Knutson, J. R. Intracellular Oxygen Mapping Using a Myoglobin-MCherry Probe with Fluorescence Lifetime Imaging. *J. Biomed. Opt.* **2018**, 23 (10), 1–14.



# 2

## The photodissociation of carboxymyoglobin (MbCO)

*This chapter focuses on myoglobin, a relatively small protein (~18 kDa) which is present in all vertebrate systems. Myoglobin plays an essential role in the diffusion of oxygen to the mitochondria of aerobic muscle, and also as oxygen storage for metabolic respiration during periods of hypoxia or high oxygen demand. This chapter presents an introduction with special focus on myoglobin characterization and on the kinetics of the rebinding reaction of a CO molecule after photodissociation.*

### 2.1 Myoglobin function

Myoglobin is a single-subunit intercellular protein found in vertebrates particularly in mammals.<sup>2</sup> Its main function is to deliver oxygen to the mitochondria in red muscle cells.<sup>1,3</sup> Similarly to hemoglobin (Hb), myoglobin (Mb) is a heme protein whose physiological importance is principally related to its ability to bind molecular oxygen via its heme cofactor. Its structure is similar to the subunits of hemoglobin and although the heme cofactor is identical in both of them, myoglobin has higher oxygen binding affinity than hemoglobin: In the blood of a healthy person, the partial pressure of oxygen ( $pO_2$ ) for Hb is approximately 26 mm Hg at 50% saturation of Hb. However,  $pO_2$  for Mb for this condition is about 1 mm Hg.<sup>4</sup> This difference in affinity leads to these proteins performing different functions in the body.<sup>5</sup> Whereas hemoglobin is responsible for binding oxygen in the lung and transporting the bound oxygen through the body via the bloodstream, myoglobin is found mostly in muscle tissue as an intracellular storage site for oxygen.<sup>6</sup>

Like oxygen, carbon monoxide binds coordinately to the heme's iron atom, but its binding affinity is 240 times greater than that of oxygen. This preferential binding of carbon monoxide is largely responsible for the asphyxiation resulting from carbon monoxide poisoning:<sup>7</sup> CO replaces oxygen in hemoglobin, decreasing the oxygen-carrying capacity and resulting in less released oxygen to tissues.<sup>8</sup> Similarly, CO when bound to myoglobin, leads to a lower supply of oxygen to the muscles.<sup>9</sup> Other heme-containing proteins, in particular mitochondrial cytochrome c oxidase, can also be a target site in human acute CO poisoning.<sup>10</sup> For more than a hundred years, carbon monoxide (CO) has been known as a toxic-killer substance that competes with oxygen for delivery to tissues. In recent years, it has been discovered that low concentrations of CO show remarkable protective effects as a cytoprotective and homeostatic molecule with important signaling capabilities and pathophysiological situation.<sup>11</sup> Moreover, each cell of a mammalian organism expresses heme oxygenase enzymes for continuous generation of CO with a key role in circadian rhythms, memory and hemodynamic regulation.<sup>12,13</sup>

### 2.2 Myoglobin structure

Myoglobin was the first protein that its three-dimensional structure determined by X-ray crystallography. This crystal structure was revealed by J.C. Kendrew, who shared the 1962 Nobel Prize in chemistry with Max Perutz<sup>14</sup> for this work. Myoglobin with a molecular mass of 18 kDa is a monomeric protein consisting of seven  $\alpha$ -helical and six non-helical segments, which contains 153 amino acids<sup>15</sup> that form a binding pocket for the heme cofactor to be discussed below (Figure 2.1A).

The iron ion has six positions to bind ligands, four of which are provided by the nitrogen atoms of the four pyroles of a porphyrin. The  $\pi$  electron system of the porphyrin interacts with an iron d-orbital in the porphyrin plane. The imidazole side chain of His93 (proximal histidine) is attached directly to the iron (Figure 2.1B). It provides the fifth ligand, stabilizing the heme group and slightly displacing the iron ion away from the plane of the heme. The sixth ligand position is available for potential ligands such as  $O_2$ , CO or NO. His-64 (distal histidine) interacts with ligand substrates but not with iron. These two main interactions between the heme's iron center, the porphyrin ring and the surrounding amino acids stabilize the heme-protein conjugate.

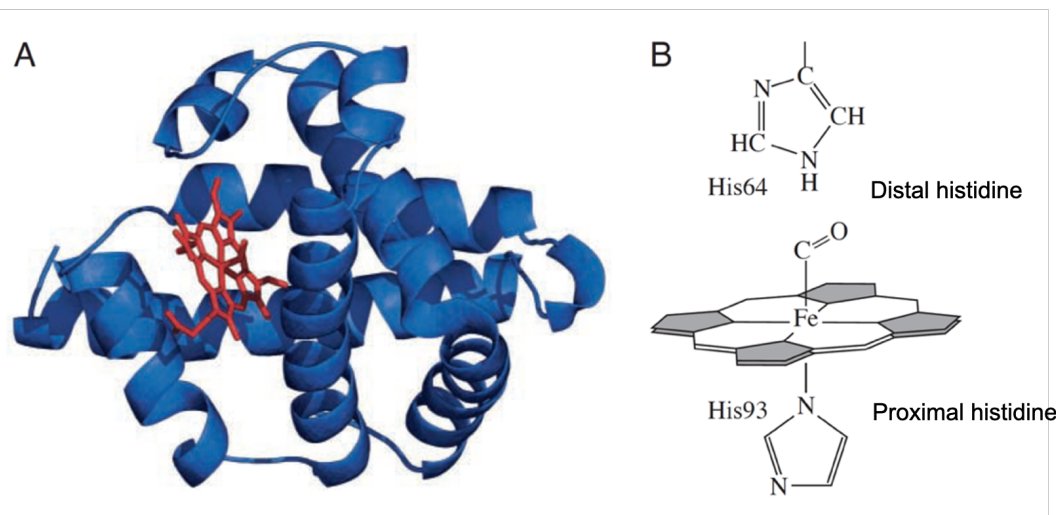


**Figure 2.1.** (A) The myoglobin structure consists of eight  $\alpha$ -helices (blue) that surround a central heme pocket (red). The heme binds to various gaseous ligands including oxygen, carbon monoxide and nitric oxide. (B) The protoheme group is stabilized by two histidine amino acids: the distal histidine residue above (His64) and the proximal histidine below (His93).<sup>15</sup>

The porphyrin group is a heterocyclic organic macrocycle, consisting of four modified pyrrole rings joined by methine bridges ( $=CH-$ ). The core structure of porphyrin is called porphin (Figure 2A).<sup>16,17</sup> Typical absorption spectra of porphyrins exhibit two main features, a single intense band named the Soret band and a group of weaker bands called Q-bands (Figure 2.2B).<sup>18</sup>

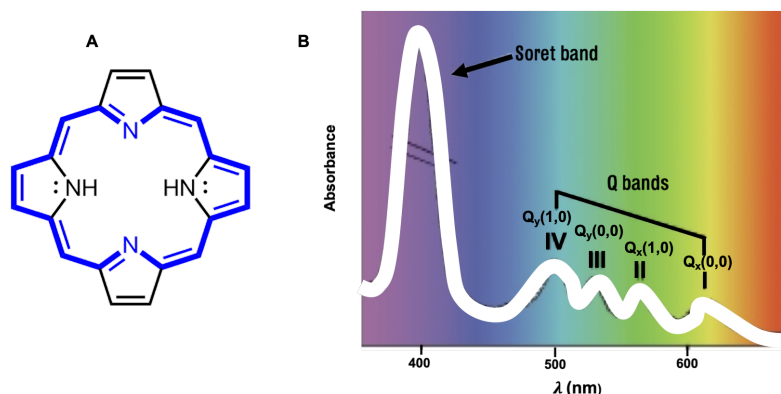


**Figure 2.2** (A) The chemical structure of porphin and (B) The absorption spectra of porphyrin. The strong peak is referred to as the Soret band and the weak group appearing at higher wavelength is split into four bands.<sup>17,19</sup>

There are three relevant ligation states for myoglobin, metmyoglobin (met-Mb), in which the iron is in the oxidized form ( $Fe^{3+}$ ) and a water molecule is covalently bound to the heme; deoxymyoglobin (deoxy-Mb), in which the iron is in the ferrous state ( $Fe^{2+}$ ) and no ligand is bound to the iron, leaving it with an unoccupied sixth coordination site; and oxymyoglobin (oxy-Mb) or carboxymyoglobin (MbCO), in which the iron is in the ferrous state ( $Fe^{2+}$ ) and has a ligand ( $O_2$  or CO) covalently bound to the heme via the iron's sixth coordination site.<sup>20</sup>

These different oxidation states of iron and the type of bound ligand can be readily identified using ultra-violet/visible (Uv-vis) absorption spectra (Figure 2.3). The main

## 2. The photodissociation of carboxymyoglobin (MbCO)

features of the Mb Uv-Vis spectra stem from the heme cofactor and consist of (1) the Soret-band in the 365 to 500 nm region and (2) the Q-bands in the 500 to 700 nm region. For met-Mb, the Soret band peak appears at 409 nm and the Q-band is marked by a weak peak at around 503 nm (Figure 2.3A, brown color) while, in deoxymyoglobin (deoxy-Mb), the Soret peak is observed at 433 nm and the Q-band shows a strong peak at 555 nm (Figure 2.3B, green color). Binding of CO (carboxymyoglobin, MbCO) shifts the Soret band to 423 nm and splits the Q-band into two peaks centered at 540 nm and 580 nm (Figure 2.3C, red color). Figure 2.4 shows the difference between deoxy-Mb and MbCO states in the Q-bands (500-700 nm) (Figure 2.4A), and Near-Infrared (NIR) (700-1000 nm) regions of the spectrum (Figure 2.4B).<sup>20,21</sup>

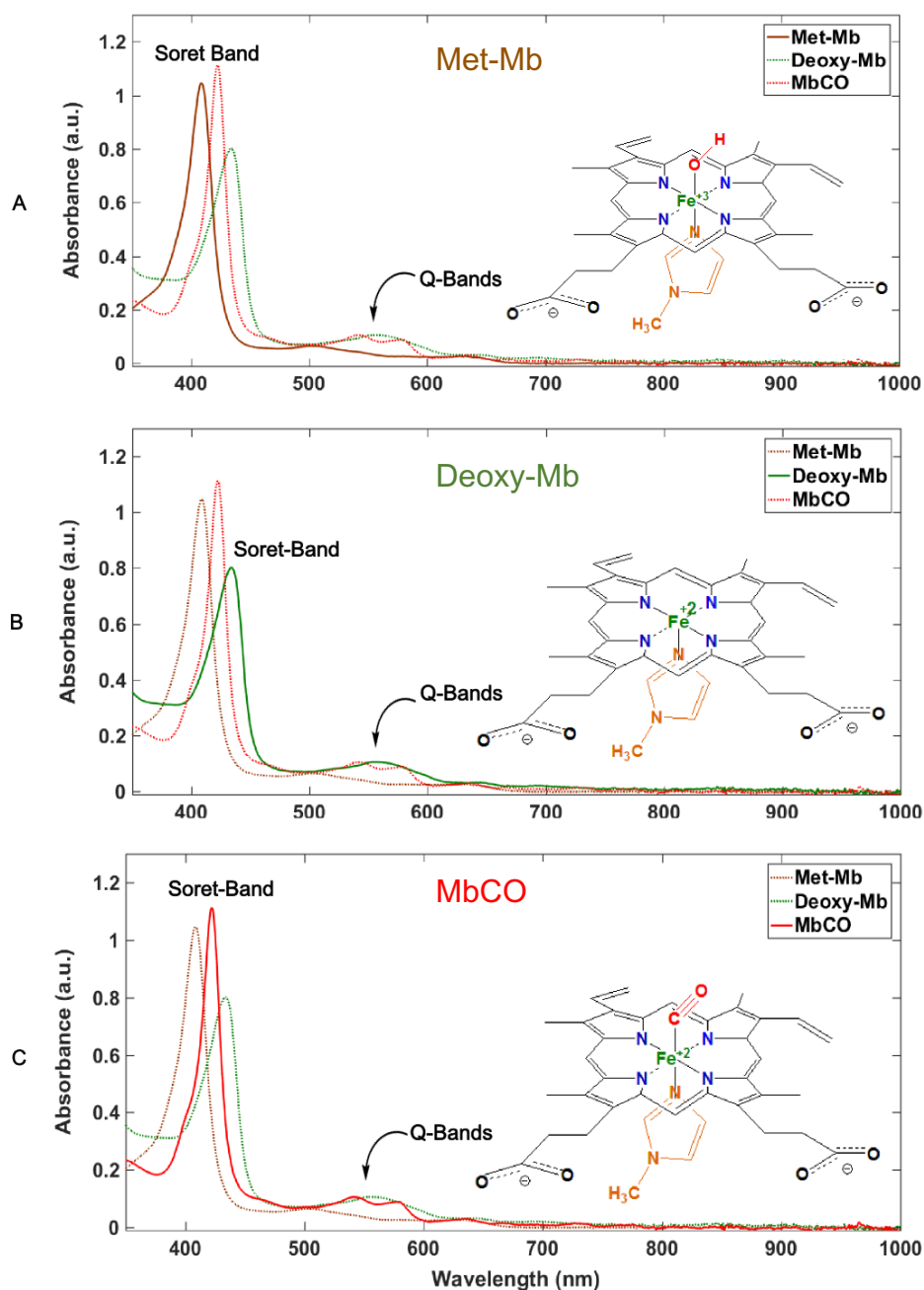


**Figure 2.3.** Absorption spectra and chemical structures of heme for met-Mb (A), deoxy-Mb (B), and MbCO (C). All absorption spectra have been measured experimentally at Leiden University.

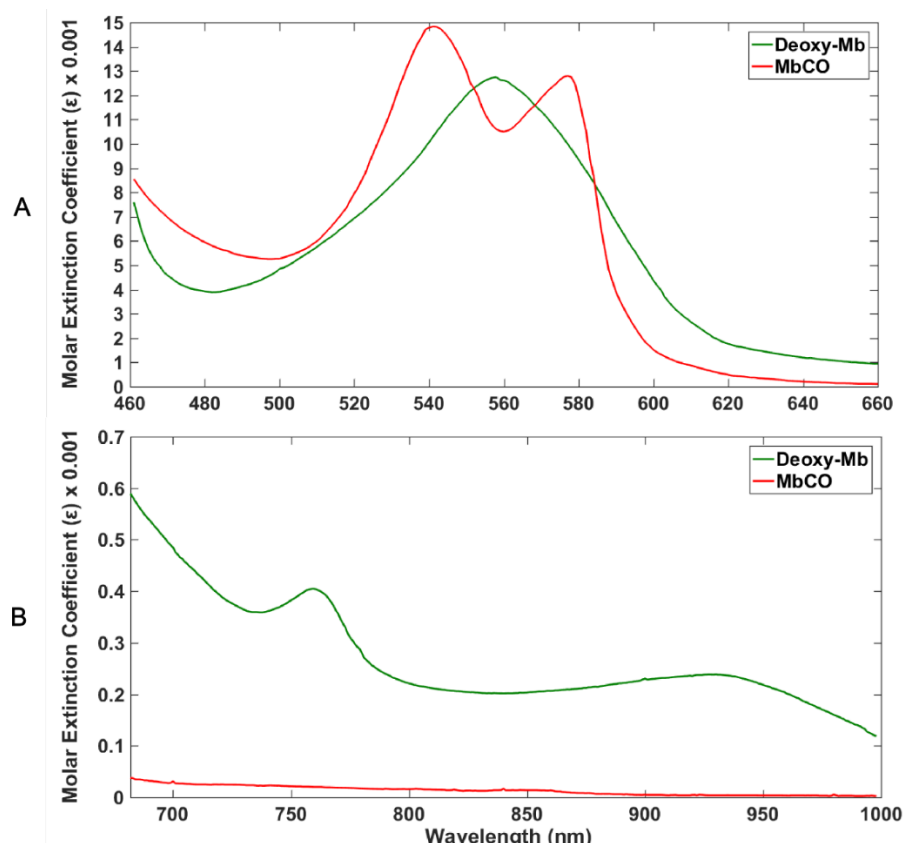


**Figure 2.4.** (A) A comparison of the Q-bands (500-700 nm) and (B) NIR (700-1000 nm) bands between deoxy-Mb and MbCO. <sup>21</sup>

## 2.3 Components of MbCO and deoxy-Mb spectra

As discussed above, association or dissociation of ligands to the heme is accompanied by spectral changes in the visible, infrared, and ultraviolet regions of the spectrum and by modifications of the magnetochemical features. This section will discuss in more detail which transitions these features stem from and how they relate to the structural changes due to ligand binding.

### 2.3.1 Soret Band

The main electronic transitions are related to the  $\pi$  electron system of the porphyrin ring, the d-orbitals of the iron atom and the nearby proximal Histidine. They comprise the intense band around 400 nm named the Soret band and the lowest-energy visible band around 550 nm.

The spectrum of Mb in the Soret region consists of a single band, which is attributed to a porphyrin  $\pi \rightarrow \pi^*$  electronic transition. Based on the Gouterman's theory of the origin of absorption bands in a porphyrin system, HOMOs (Highest Occupied Molecular Orbitals) are formed by two nearly degenerate  $a_{1u}$  and  $a_{2u}$  orbitals and the LUMOs (Lowest Unoccupied Molecular Orbitals) are formed by a set of  $e_g$  orbitals (Figure 2.5A). Transitions between these orbitals lead to two excited states of  ${}^1E_u$  character. The Soret band arises from excitation from the two orbitals  $a_{1u}(\pi)$  and  $a_{2u}(\pi)$  to the higher energy  $E_u$  orbitals of the porphyrin ring (Figure 2.5B). <sup>22,23</sup>



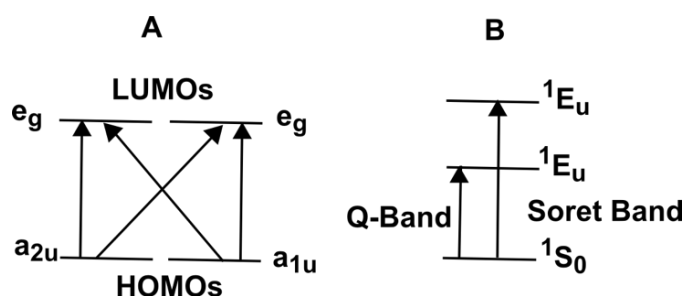


**Figure 2.5.** (A) Gouterman's model;  $a_{1u}$  and  $a_{2u}$  orbitals (HOMOs) and the two  $e_g$  orbitals (LUMOs), (B) Energy levels and electronic transitions of Soret band and Q-band in porphyrins.<sup>22</sup>

### 2.3.2 Q- Band

There is another porphyrin  $\pi \rightarrow \pi^*$  electronic transition at the lower energy side of the two bands usually denoted by [Q(0,0) and Q(1,0)]. In a symmetric molecule, the first excited state,  $S_1$ , is a degenerate state comprising  $Q_x$  and  $Q_y$  components. At lower symmetry, the above-mentioned bands are further split into two bands each. The X and Y components are no longer degenerate and therefore we see four bands in the Q band region, which are denoted by  $Q_x(0,0)$ ,  $Q_y(0,0)$ ,  $Q_x(1,0)$  and  $Q_y(1,0)$  (Figure 2.2B).<sup>23</sup> These four bands in the visible regions of the spectrum are allowed by  $D_2$  symmetry. In case of a metalloporphyrin, the symmetry changes from  $D_2$  to  $D_{4h}$  because the two of the inner pyrrole hydrogens are replaced by metal-nitrogen bonds. Thus, the coplanar metalloporphyrins have a higher symmetry.<sup>24,25</sup> The lack of two hydrogens reduces the number of visible bands from four group bands (Figure 2.2B) to two group bands, such as in myoglobin (Figure 2.3).

### 2.3.3 Near Infrared

The NIR (750- 2500 nm) regions of the spectrum of deoxy-Mb exhibits three bands that are labeled I, II, and III (Figure 2.6B). Band I is related to a charge-transfer from the iron to the porphyrin [ $d_{xz} \rightarrow e_g(\pi^*)$ ], band II corresponds to an iron  $d \rightarrow d$  transition ( $d_{xz} \rightarrow d_{z^2}$ ), and band III corresponds to a porphyrin to iron charge-transfer transition ( $a_{2u}(\pi) \rightarrow d_{yz}$ ) (Figure 2.6A, green). Experimentally measuring band III is difficult due to its small extinction coefficient (approximately  $350 \text{ M}^{-1} \text{ cm}^{-1}$ ) at room temperature (Figure 2.6B).<sup>26</sup>

The transitions observed in the MbCO spectrum are classified in three types: 1) metal centered (d)  $\rightarrow$  (d) transitions, 2) charge-transfer transitions from porphyrin to iron [ $(\pi) \rightarrow (d)$ ] and 3) promotions of an electron from either an iron d or porphyrin ( $\pi$ ) orbital into the CO ( $\pi^*$ ) orbital.<sup>27</sup> The optical spectrum of carboxymyoglobin is very much like that of a closed-shell metal porphyrin, which generally only exhibits the porphyrin Soret and Q bands (Figure 2.3C).

MbCO has a much lower extinction coefficient around 700-800 nm, ( $\epsilon < 30 \text{ M}^{-1} \text{ cm}^{-1}$ ) compared to deoxy-Mb ( $350 \text{ M}^{-1} \text{ cm}^{-1}$ ) (Figure 2.6B),<sup>28</sup> but there is no evidence for NIR bands in either the crystal or solution absorption spectra of MbCO.<sup>29,30</sup> This lack of any near-infrared electronic absorption is important for the design of our experiments. The magnetic circular dichroism (MCD) technique can detect weak transitions which cannot be seen in an absorption spectrum. A near-ultraviolet-visible

MCD study of MbCO by Vickery et al. also provides no evidence for additional transitions.<sup>20</sup> The single-crystal data shown the absence of iron (d)  $\rightarrow$  porphin ( $\pi^*$ ) transitions since there is no evidence for any z-polarized intensity as would be expected for the  $d_{yz} \rightarrow e_g (\pi^*)$  transitions. The most plausible assignment for bands I and II, then, is that they correspond to iron d  $\rightarrow$  d transitions, as originally suggested by Eaton and Charney on the basis of their relatively large CD anisotropy factors.<sup>31</sup>

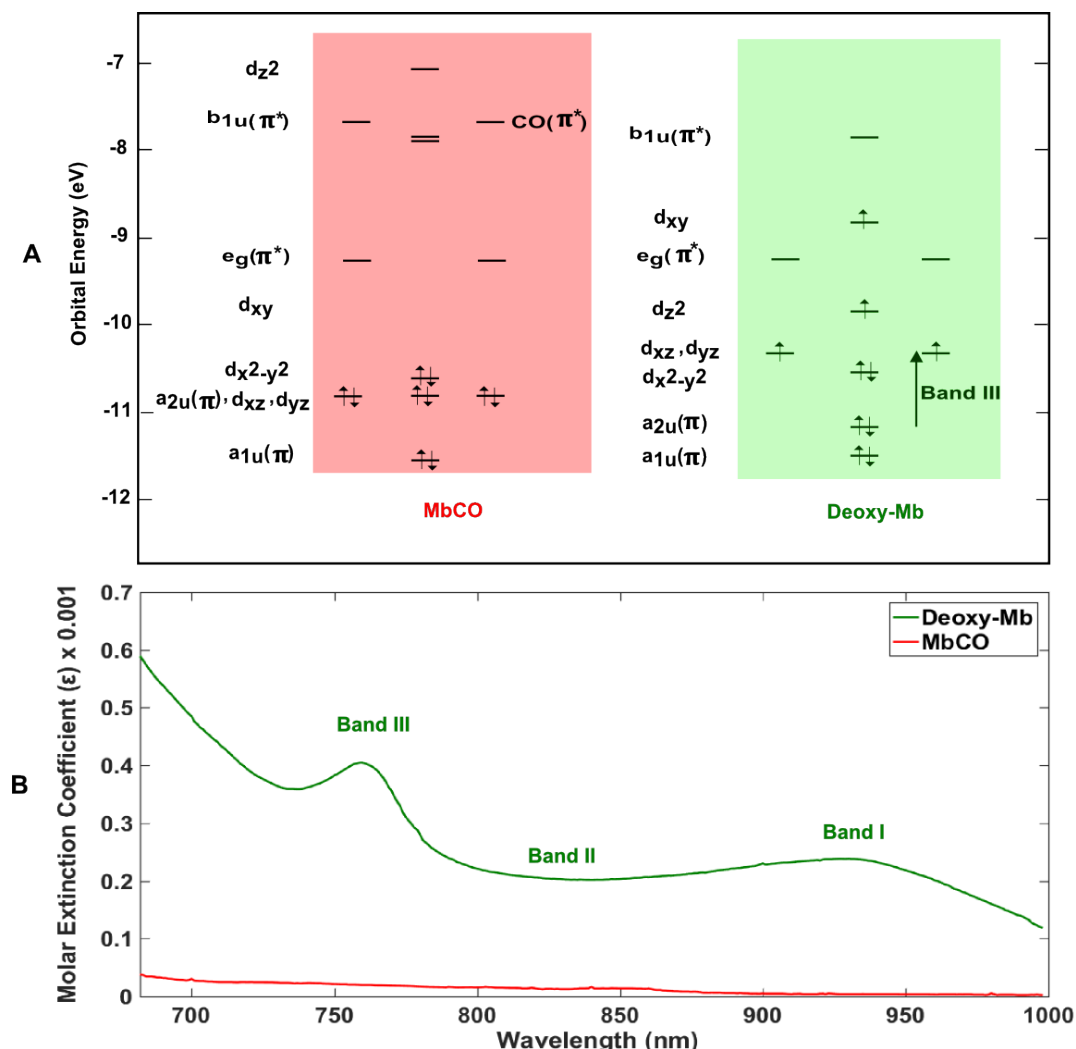


**Figure 2.6.** (A) Extended Hückel orbital energies for MbCO (red), and deoxy-Mb (green). The arrow indicate the electronic transition related to Band III in deoxy-Mb (modified after<sup>20</sup>). (B) Comparison of the absorption in NIR region (700-1000 nm) between MbCO and deoxy-Mb. Band I, Band II, and Band III have been labeled for deoxy-Mb (modified after<sup>21</sup>).

## 2.4 Photodissociation and its mechanism

Photodissociation and binding-rebinding rates provide useful information about conformational changes of myoglobin related to ligand migration inside protein pocket. Studies on the rebinding reaction rate of myoglobin with ligands have revealed a complex ligand-protein interaction after bond breaking, which results in multiple kinetic intermediates due to the protein relaxation and movements of the ligand within the protein.<sup>32–35</sup>

## 2.5 Photodissociation of Mb-CO bond

Over decades, many investigations have revealed that the carbon monoxide complex of myoglobin (MbCO) is light-sensitive.<sup>36–38</sup> Upon the absorption of a photon, the iron-carbon monoxide bond breaks (dissociation), and a series of spectroscopic and structural changes starts, after which the carbon monoxide spontaneously rebinds at room temperature and MbCO is reconstituted (recombination).<sup>39–42</sup> The dissociation and recombination reactions of Mb\*CO have been investigated with various spectroscopic techniques at various temperatures and in a number of solvents.<sup>43–51</sup> After photodissociation, the CO ligand is still located close to the heme (primary docking site) in the initial intermediate noted Mb:CO. From there, CO can either rebind again to the heme by crossing the inner barrier (geminate rebinding) or escape. In the latter case, CO migrates through the protein matrix to a different protein internal cavity, one of the so-called xenon cavities (Figure 2.7).

Figure 2.7A shows four internal cavities in myoglobin named Xe1, Xe2, Xe3, Xe4 that bind a xenon atom with high affinity (Figure 2.7A).<sup>52</sup> The extent of ‘geminate’ (internal) recombination from these sites depends on the reactivity of the ligand with the heme iron and on its ability to diffuse away from the active site to the xenon cavities.

Based on X-ray crystallography, it is found that CO accumulates in one of the Xe binding cavities (Xe1) which is located on the proximal side of the heme (the side in which the imidazole side chain of His93 is attached directly to the iron) (Figure 2.7A). The Xe1 site is highly occupied by the CO ligand and is the one with the highest affinity. The Xe4 pocket is another possible secondary binding site in the back of the distal pocket, located in the neighborhood of the primary docking site. According to MD simulations native MbCO, CO occupies the Xe4 cavity, which suggests a migration route from Xe4 to Xe1.<sup>53,54</sup>

From Xe(4), CO escapes to the solvent with a lifetime of 400 ns, but the transfer of CO to the Xe(1) trapping site occurs much faster. Thus, CO is trapped in the Xe(1) site and, from there, it escapes to the solvent with a lifetime of 700 ns. The docking positions of CO in wild type Mb: the primary docking site, Xe(4), and the Xe(1) sites, and the escape path of CO to the solvent are shown in Figure 2.7B.<sup>55</sup>

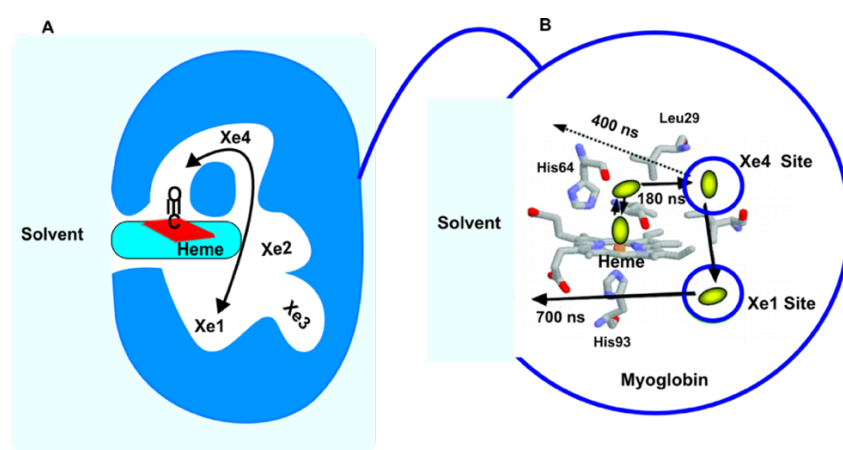


**Figure 2.7.** (A) Schematic illustration of the internal xenon cavities in MbCO which consist of locations Xe1, Xe2, Xe3, Xe4 (modified after<sup>56</sup>). (B) Mechanism after Wild-type MbCO photodissociation at room temperature, which consists the geminate rebinding of CO ligand (green ellipsoid ball) with heme, migration to xenon cavities (Xe4, and Xe1), and escape to the solvent (modified after ref.<sup>55</sup>).

As far as the photolytic state is concerned, the most widely accepted hypothesis is that dissociation occurs from a metal-to-ligand charge-transfer (MLCT) state.

Based on the experimental data, the fast heme dissociation step is not just one quick step; it is a complicated process which consists of several internal conversion (IC) steps along a series of intermediate excited states with gradual structural changes until it ends in the ground state of high spin deoxy-Mb (Figure 2.8).<sup>42</sup>

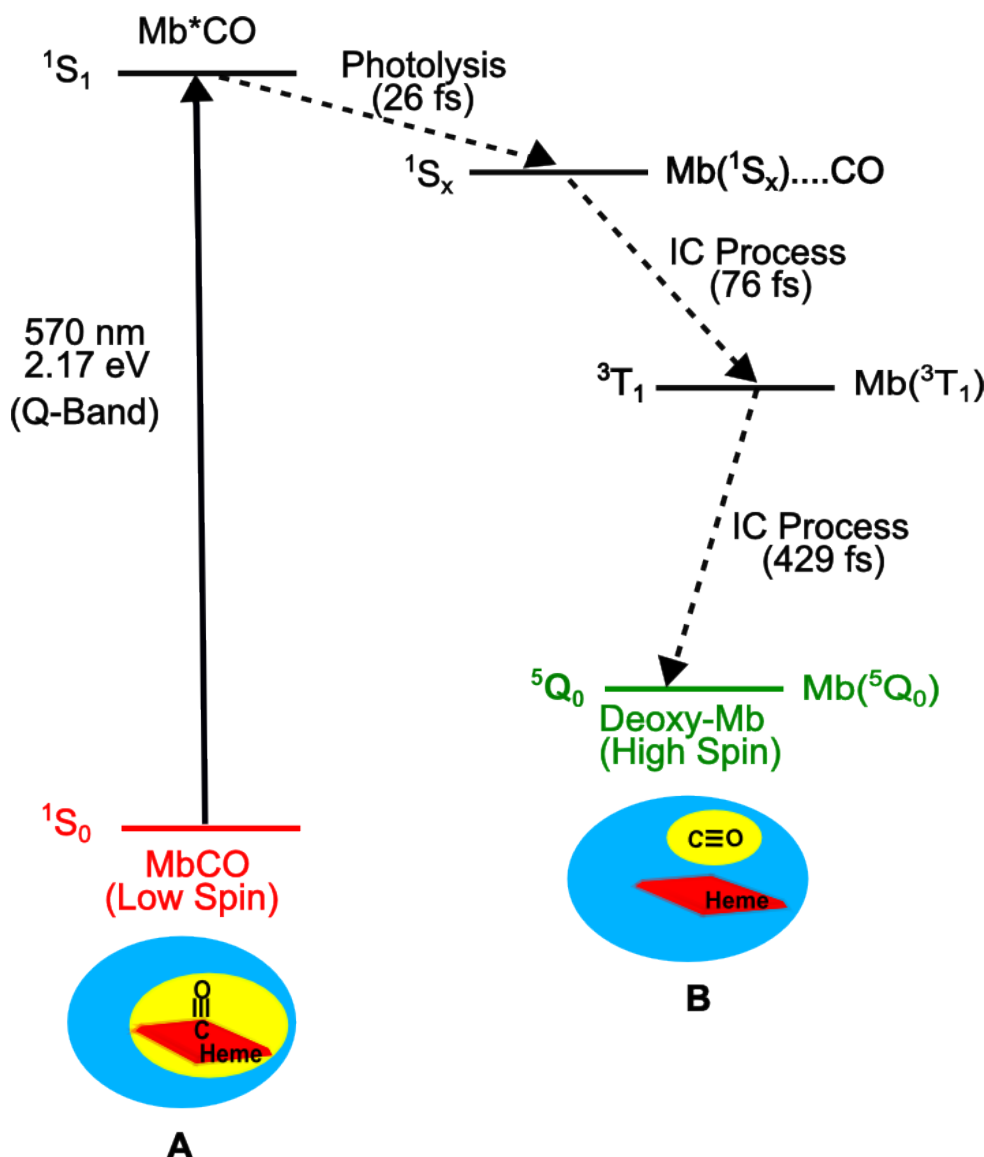


**Figure 2.8.** An energy level schematic for photodissociation of MbCO at room temperature. Illumination of MbCO at 570 nm and excitation from ground state ( $^1S_0$ ) of MbCO (A) to the excited state ( $^1S_1$ ), is followed by photodissociation within 50 fs to the first excited intermediate state ( $^1S_x$ ) relaxes, through an IC process to the second intermediate excited state ( $^3T_1$ ), and finally, through another IC process, the photodissociation completes and MbCO relaxes to the deoxy-Mb ground state ( $^5Q_0$ ) (B) (modified after<sup>42</sup>).

This overall process encompasses three main sequential steps (Figure 2.8):<sup>57</sup>

$^1S_1 \rightarrow ^1MLCT \rightarrow ^3MLCT \rightarrow ^5MLCT$ :

1).  $^1S_1 \rightarrow ^1S_x$  ( $^1MLCT$ ): singlet lowest excited state to singlet metal-ligand CT state;

2).  $^1S_x (^1MLCT) \rightarrow ^3T_1 (^3MLCT)$ : spin crossover (ISC) from singlet metal-ligand CT state to triplet metal CT state;

3).  $^3T_1 (^3MLCT) \rightarrow ^5Q_0 (^5MLCT)$ : spin crossover (ISC) from triplet metal-ligand CT state to quintet metal- ligand CT state;

The first relaxation step is a transition from the  $^1S_1$  state of Mb\*CO to a  $^1S_x$  state of Mb...CO ( $^1MLCT$ ). This leads to a complete decay of the  $^1S_1$  population after  $\sim 100$  fs and the dissociation takes 26 fs (Figure 2.7A). Franzen et al. were the first to rule out the involvement of a high spin state in the transition from the Q state to a  $^1MLCT$  state and they assigned a mechanism for the photolysis which was not considered before: the removal of one sigma bonding electron from an iron-CO ( $d_{Fe}-\pi_{CO}$ ) orbital reduces the back-bonding of the CO ligand to the iron ( $d_{Fe}-\pi^*_{CO}$ ).<sup>57</sup> The similarities of the excited states lifetimes and absorption maxima in the spectra of both ligated and unligated forms indicate that the first fast step already results in the dissociation of the ligand. Based on the proposed photophysical pathway, iron-to-ring charge-transfer is the key event in the mechanism of photolysis of diatomic ligands following a porphyrin ring  $\pi \rightarrow \pi^*$  transition.

The second step includes a change in the spin state of the Mb from a singlet ( $^1S_x$ ) to a triplet ( $^3T_1$ ,  $^3MLCT$ ) on a time scale of around 76 fs. This is followed by the third step in which the system relaxes to the deoxy-Mb with high-spin quintet state ( $^5Q_0$ ,  $^5MLCT$ ) on a time scale of around 429 fs (Figure 2.7).

Basically, in MbCO, the iron atom is located within the plane of the porphyrin ring in a low spin state whereas, in deoxy-Mb, iron is about 0.3 Å out of the plane in a high-spin state. Experimental evolution of the Fe–C(O) distance and data obtained from the Fe out-of-plane distance also show that the iron goes out of the plane of the porphyrin ring almost instantly upon photodissociation and oscillates with a large amplitude with a 40 fs period. Therefore, this measured iron motion is probably due to crossover spin state where the iron switches from the low-spin configuration in the ligated species to of the unligated form.<sup>57</sup> Figure 2.9 shows the Fe out-of-plane upon photodissociation of MbCO and as it can be seen, the Fe–CO distance oscillates between the equilibrium distance (1.7–1.8 Å) (undissociated Mb-CO) and 2.5 Å (dissociated Mb-CO) (). The amplitude of the oscillation is initially 0.9 Å and reaches a value of 2.2 Å where CO is dissociated. Followed by initial oscillation, the wave packet is in the MLCT bands where, due to repulsive interactions, CO does not recombine to heme and continues oscillations. Relaxation of the structure restrains these oscillations to reach the equilibrium value of 2.2 Å.<sup>57</sup>

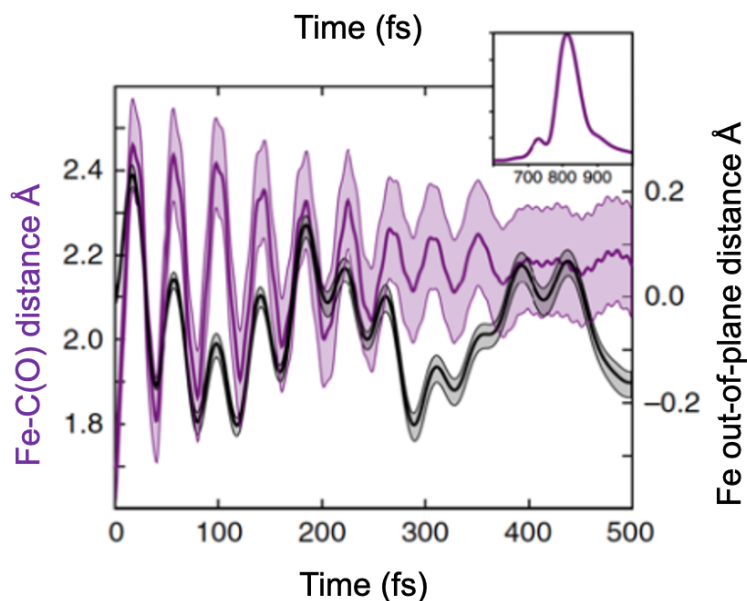


**Figure 2.9.** Evolution of the Fe–C(O) distance (magenta, left axis) and of the Fe out-of-plane distance (black, right axis) upon photodissociation of MbCO. The amplitude of the oscillation is initially 0.9 Å. The Fe distance (Fe–C(O)) stabilizes at a value of 2.2 Å. At this distance, the CO is essentially photodissociated. The measured equilibrium distance of Fe–C(O) is between (1.7–1.8 Å) and 2.5 Å and the standard deviation of these geometric values is indicated by the shaded area. The Fourier transform of the Fe–C(O) oscillations is illustrated in the insert (in  $\text{cm}^{-1}$ ).<sup>57</sup>

Photodissociation of MbCO through excitation to the lowest excited state of the heme ( $^1S_1$  of Mb\*CO, Figure 2.7) is forced by a iron to porphyrin charge-transfer with a quantum yield of essentially 1. MCD studies have shown the lack of any near-infrared electronic absorption for MbCO. Also, the single-crystal data confirm the absence of a iron (d) —porphyrin ( $\pi^*$ ) transition since there is no evidence for any z-polarized intensity as would be expected for a  $d_{xz}, d_{yz} \rightarrow (e_g\pi^*)$  transition. In the absorption spectrum of MbCO, there is a very-low-intensity absorption between 700–800 nm ( $\epsilon < 30 \text{ M}^{-1} \text{ cm}^{-1}$ ), which is not due to the metal to protein charge-transfer and may derive from a metal-centered iron (d)  $\rightarrow$  (d) transition. Therefore, excitation of MbCO in the NIR is unlikely to facilitate photodissociation of MbCO.<sup>20,27–29</sup>

Many authors have studied the kinetics of rebinding after photodissociation and found that the rebinding parameters significantly change with temperature, solvent composition, viscosity, and the myoglobin mutant.<sup>43–51,58–64</sup>

Despite much work,<sup>65–68</sup> the ligand migration pathway and protein dynamics are still mysterious and not yet completely known. Frauenfelder has suggested that ligand binding is governed by successive barriers depending differently on temperature, and solvent.<sup>69–72</sup> Information regarding the barriers and the energy of the intermediates is very important to reach a coherent description of the dynamics of ligand binding to Mb, but our knowledge in this area is very limited.

Regarding the MbCO photodissociation at low temperature, several kinetic intermediates have been shown during geminate rebinding and recombination of the escaped ligand with the protein. However, at ambient temperature kinetics studies of MbCO photodissociation in water revealed no features of the multiple intermediate states except for geminate recombination kinetics.<sup>73–77</sup>

### 2.6 Photodissociation and CO rebinding at room temperature

In solution at physiological temperatures, a protein undergoes some conformational fluctuations that grow in related amplitude with temperature. In the case of MbCO, temperature enhancement facilitates ligand escape to the solution.<sup>78</sup>

Photodissociation in solution has been intensively investigated by measurements of the geminate recombination kinetics (fast pathway) or bimolecular recombination kinetics (slow pathway) at different temperatures, viscosities, pHs, and with various mutants.<sup>43–51,58–64</sup> Although it has been well-recognized that there are several intermediate states separated by activation barriers along the escape pathway, the CO escape process in solution at physiological temperatures has been less clear because it is spectroscopically almost silent.<sup>78</sup>

Advances in spectroscopic methods such as femtosecond and nanosecond time-resolved UV-visible<sup>79,80</sup> and IR spectroscopy<sup>81–83</sup> have made it possible to study the re-binding process of the photolyzed MbCO and to resolve ligand escape from the protein in real time. Based on IR spectroscopy, it was concluded that upon photodissociation of MbCO, CO becomes trapped in a docking site in the vicinity of the heme iron within a distance of a few Angströms.<sup>45</sup> The docking site forces CO to orient approximately parallel to the plane of the heme, which is almost perpendicular to the bound CO. This orientation and interaction in the docking site have the effect of dramatically slowing the rate of CO rebinding. The Mb docking site therefore facilitates efficient expulsion of CO from the protein with less than 2% geminate rebinding at 32 °C. Similarly, nanosecond transient absorption spectroscopy at room temperature shows that, after photolysis of the carbon monoxide complex, about 4% of the photodissociated carbon monoxide molecules rebinds to the heme with a relaxation time of 180 ns.<sup>45</sup>

It is worth mentioning that these absorption spectroscopic studies only focused on structural changes around the heme chromophore and no other part of the pocket in the vicinity of the heme. Laser-induced transient grating (TG) and laser-induced photoacoustic calorimetric techniques could determine quantitatively the energetics and structural volume changes of the protein after photodissociation of MbCO and provide more detailed information about the protein dynamics during photodissociation.<sup>84</sup> Based on the transient grating (TG) experiments for sperm whale MbCO, the rate of ligand escape to the solvent was measured to be 700 ns at 20 °C. This fact that ligand escape is slower than the apparent geminate recombination (180 ns) clearly indicates that there is a ligand trapping site inside the protein (Figure 2.7). It should be noted that for horse heart MbCO a faster kinetics (79 ns at 20 °C) besides the 700-ns dynamics were obtained and this component might represent the CO transport process inside the protein.<sup>84</sup>

The photodissociation reaction scheme is shown in Figure 2.10.

In the first step, MbCO is photoexcited to the electronic excited state, where the ligand photodissociates from the heme within 2 ps; in this step, CO is trapped in the heme pocket in close proximity to the heme (Mb:CO) as the first intermediate species which can recombine and re-establish the initial Fe-CO bond. The explanation for the initial structural and enthalpy changes ( $t < 10$  ns) could be the initial movement of the proximal His and the motion of the heme. The energy of the first intermediate species ( $\Delta H_f = 61$  kJ/mol) demonstrated in Figure 2.10, is smaller than the Fe-CO bond enthalpy (105 kJ/mol). This difference indicates that the protein structure is relaxed

and stabilized after the CO dissociation within 10 ns, which is consistent with a negative volume change in the initial step ( $\Delta V_f = -5$  ml/mol).

Then, with a lifetime of 180 ns, CO goes to another trapped site where it is far enough from the heme (Mb::CO) so that it cannot recombine again. The 180 ns step is probably related to the diffusion of the CO out of the heme pocket which is accompanied by a change in the electronic state of the heme. The transfer of the CO to another site in the protein matrix does not change the protein structure significantly and could involve only a small change in enthalpy and volume and the TG signal is not sensitive enough to detect these changes. The third step is the diffusion of CO out of the protein into the solvent by a monoexponential process with a characteristic time of 700 ns at room temperature.

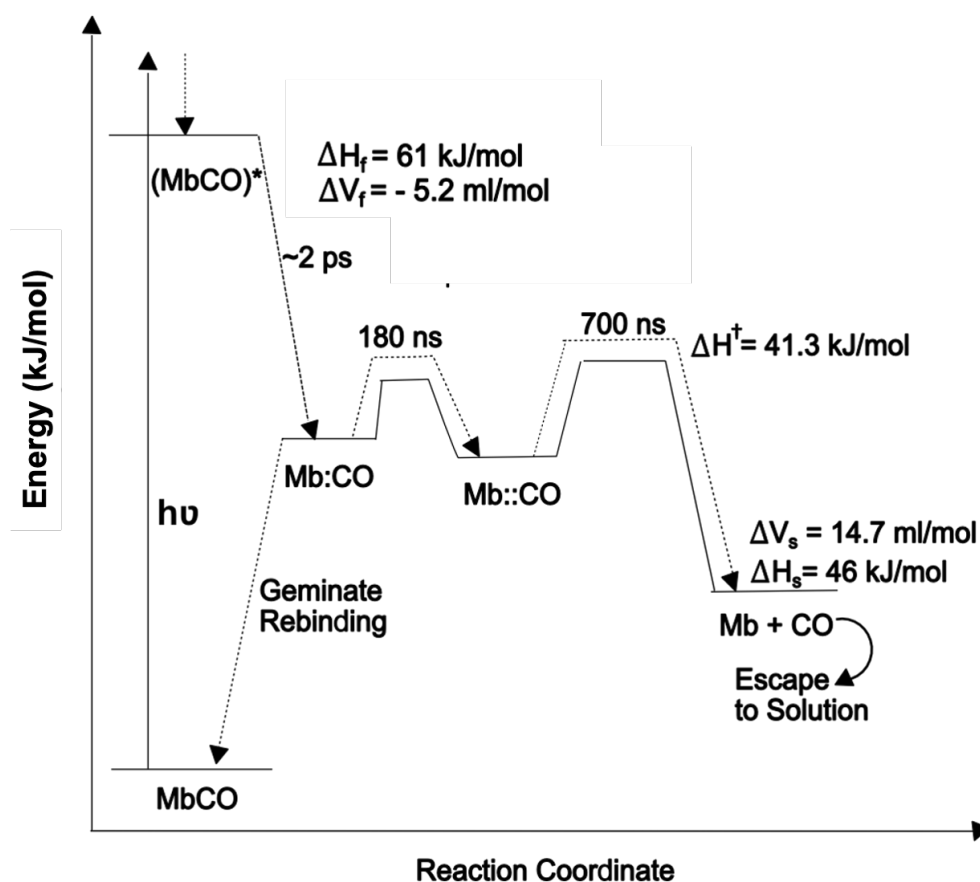


**Figure 2.10.** Photodissociation reaction scheme of CO from MbCO at room temperature. After photoexcitation to the electronic excited state of MbCO, the ligand photodissociates from the heme within 2 ps; the ligand is thereby trapped in the heme pocket, and from there the CO can recombine to the heme again. On a time scale of 180 ns, the CO moves to another trapped site from which it cannot recombine to the heme. The ligand escapes from the protein to the solvent in 700 ns at room temperature. The kinetics can be expressed by a single-exponential function (modified after <sup>84</sup>).

As demonstrated in Figure 2.10, after the initial volume contraction associated with MbCO to Mb::CO, an expansion of volume ( $\Delta V_f = 14.7$  mL/mol at 20 °C) and exothermic enthalpy changes (from  $\Delta H^\ddagger = 41.3$  kJ/mol to  $\Delta H_s = 46$  kJ/mol) have been observed in the 700 ns step. This large effect could be explained in terms of the CO



escaping from the myoglobin into the solvent. It should be noted that this 700 ns process has not been detected by IR absorption and Raman scattering because the heme is not affected by this step.

### 2.7 Photodissociation at low temperature

At low temperatures, after a photoflash, the same ligand previously bound to the heme may recombine again with that heme. In contrast to the familiar exponential kinetics of elementary unimolecular reactions, below 180 K rebinding occurs nonexponentially in a 75% glycerol/water solvent.<sup>85</sup> It is assumed that in frozen samples (low temperature) each Mb molecule has a determined conformational state whereas, in a liquid sample (high temperature), the conformational state of each Mb molecule can change rapidly from one state to another. If, at low temperatures, the rate of transition between such conformations is slow, contrary to high temperature, each molecule will not be able to average the activation barrier over all conformations, resulting in a distribution of barrier heights instead of a sharp activation energy.<sup>73–77,85</sup>

#### 2.7.1 Model for photodissociation at low temperature

Hans Frauenfelder was born on June 28, 1922,<sup>86–87</sup> whose 100th birthday is the occasion of this thesis, was the first who explained the structural heterogeneity of proteins using the energy landscapes.<sup>87</sup> An energy landscape is a map of possible atomic motions in a molecule and their related Gibbs free energy. The hypersurface of energy landscape constitutes some valleys and the free-energy minimum is related to the initial and final state of a reaction named a “state”, whereas the saddle point between two minima named “transition state”. Each state contains a huge number of conformational substates that hierarchally ordered into different tiers of energy (Figure 2.11).

Frauenfelder and coworkers proposed a hierarchical arrangement of conformational substates based on the photodissociation experiments on MbCO. MbCO has the conformational energy ( $E_c$ ) with the unique energy valley (Figure 2.11A), which has a few taxonomic substates, exist on the highest level, denoted Tier 0 (Figure 2.11B). These substates present the energy minima separated by high free-energy barriers and they are characterized based on their structural, spectroscopic and energetic properties. For example, there are at least three substate of  $A_0$ ,  $A_1$ , and  $A_3$  (Tier 0), after photodissociation of MbCO at low temperature ( $T < k$ ). They have the same primary amino acid sequence but differ, at least, in the geometry of the bound CO as shown in Figure 2.11 B at right. It should be noted that each substrate binds to CO with different rates for example,  $A_3$  shows the slowest CO binding rate and  $A_0$  has the fastest rate and all three substates ( $A_0$ ,  $A_1$ , and  $A_3$ ) rebind nonexponentially in time (Figure 2.11, right). The relative energies, entropies, and volumes for each of these substates are known and characterized. Each taxonomic substate harbors a large number of statistical substates of lower tiers such as tier 1, tier 2, tier 3,... that are separated by smaller energy barriers (Figure 2.11C). The energy landscape is changed by environmental conditions of the protein such as solvent properties, ligand binding which make it possible for protein to perform its functions.<sup>88</sup>

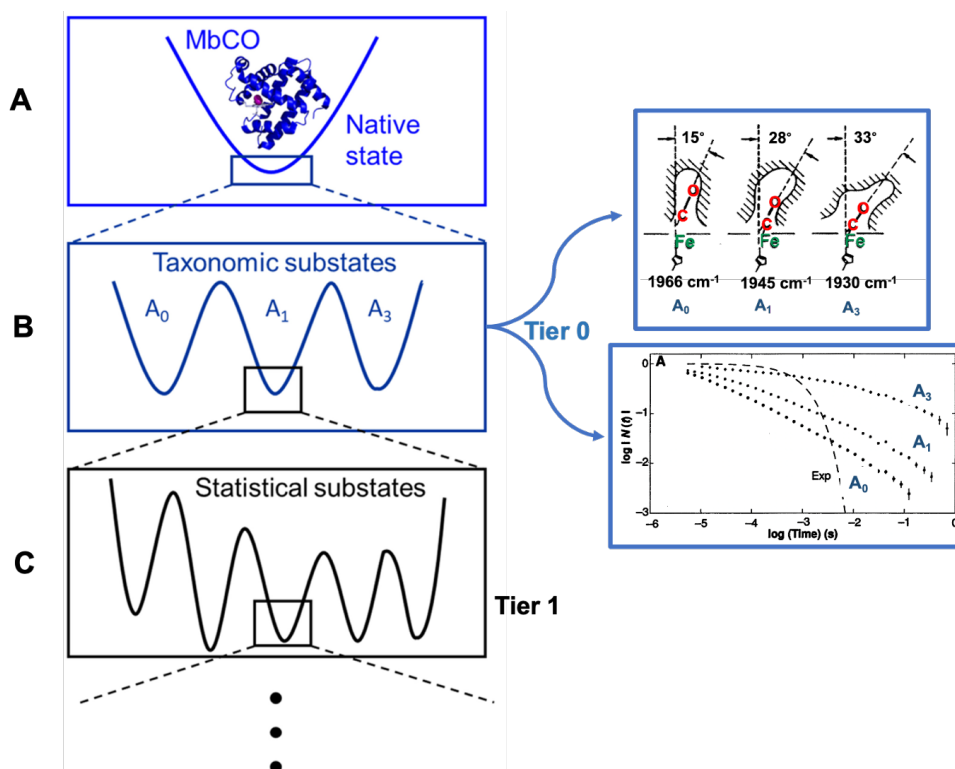
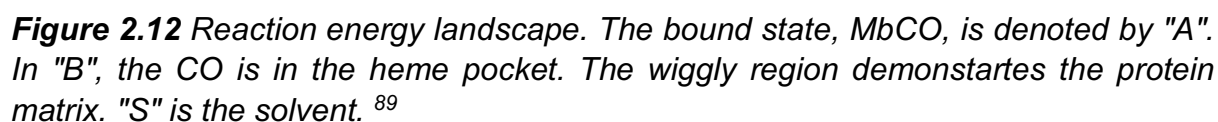


**Figure 2.11** Structure and conformational energy landscape of MbCO. The energy landscape is arranged hierarchically, with conformations nested in several tiers, according to the barriers separating the states. (A) The 3D structure of MbCO and an overall picture of the conformational energy  $E_c$  with the unique energy valley (B) (left) Three substates of Tier 0:  $A_0$ ,  $A_1$ , and  $A_3$ . (B) (right, at top) These three are due to the different orientation of the bound CO with respect to the heme, which make the different stretch band (Fe-CO). (B) (right, at down) Rebinding of CO to Mb after photodissociation, for the substates of tier 0 at pH 5.7,  $N(t)$  is the fraction of protein that have not rebound a CO at the time  $t$  after photodissociation. All three substates ( $A_0$ ,  $A_1$ , and  $A_3$ ) rebound nonexponentially in time. (C) Tier 1 is vastly oversimplified. In reality, the potential energy  $E_c$  of the protein as a function of conformational coordinate is a hypersurface in a conformational space of very high dimensions and the number of valleys is extremely large. Valleys and barriers can no longer be characterized individually but must be described by distributions. [Modified after <sup>88,89</sup>]

At low temperature, the protein is frozen and the CO cannot escape the protein. As the protein begin to relax (at  $T > 180$  K), the CO can move through the different protein internal cavity. At low temperature, in photodissociation a ligand molecule bound to the iron atom undergoes a series of steps to move finally to the outside of protein by thermally overcoming all barriers. Based on research by Frauenfelder,<sup>90</sup> a model consisting of four steps has been proposed for low-temperature photodissociation of MbCO.

In 1991, Steinbach and coworkers defined a dynamic three-well model. This model consists of three states: The bound state (A), the pocket state (B), and the solvent state (S) (Figure 2.12). When a photon breaks the Fe-CO bond, the system moves



Between 160 K and 210 K, the protein is no longer frozen, therefore the structure of the low-temperature photoproduct starts to relax into the deoxy-Mb structure. The Mb\*→Mb relaxation results in the g(H) distribution to shift toward higher enthalpies about 10 kJ/mol. The relaxation function  $\Phi^*(t, T)$  is nonexponential in time based on the following equation:

Moreover, the relaxation function  $\Phi^*(t, T)$  is non-Arrhenius in temperature (eq. 2.2) and essentially independent of the solvent viscosity

38

When temperature rises to above 210 K, due to the equilibrium fluctuations, the CO ligand escapes into solvent on the time scale of rebinding. The transitions between the solvent S and the heme pocket B ( $S \leftrightarrow B$ ) is formed by the fluctuations in the protein matrix. The  $\kappa_1(T)$  for these equilibrium fluctuations ( $E_{F1}$ ) shows a non-Arrhenius temperature dependence that depends strongly on the viscosity. At temperatures between 210 and 250 K and/or high solvent viscosity, the ligand binding kinetics is dominated by the outer barrier (between the solvent S and the heme pocket B). At room temperature the barrier  $H_{BA}$  is still distributed, but equilibrium fluctuations ( $E_{F1}$ ) result in average rate coefficients ( $\kappa_{BA}$ ).

In a flash photolysis experiment on the sperm whale MbCO sample with a pulse laser (480 nm), the bond between the CO and the heme iron is broken. Experiments on band (III), a charge-transfer band at 760 nm ( $213000 \text{ cm}^{-1}$ ) in deoxy-Mb (the photolyzed state of MbCO) which is absent in the bound form (MbCO). The difference in the absorption spectra at a selected wavelength,  $\Delta a(t)$ , for the bound and the dissociated species monitors the subsequent CO rebinding. The survival probability,  $N(t, T) \equiv \Delta a(t) / \Delta a(0)$ , is the fraction of Mb molecules at temperature T that have not rebound CO at the time t after the flash photolysis. The CO rebinding data to sperm whale myoglobin are shown in Figure 2.13. The faster process seen at all temperatures I for "internal"; it is nonexponential in time and independent of CO concentration. The slower process that appears above 200 K, denoted by S for "solvent", is exponential in time with a rate coefficient proportional to the CO concentration in the solvent.<sup>89</sup>

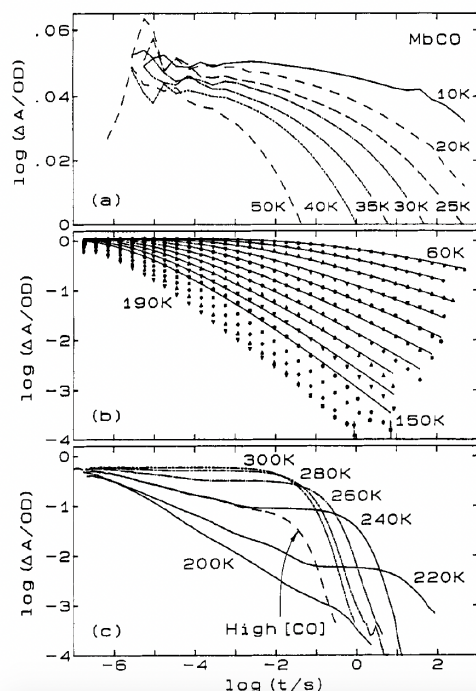


**Figure 2.13** Rebinding of CO to Mb after flash photolysis.  $\Delta a(t)$ , the absorbance change at the time t after photodissociation, measured at 440 nm, is plotted versus  $\log t$ .  $\Delta a(0) = 1.12 \text{ OD}$  below 200 K, pH 6.8. Solvent: 75% glycerol/buffer (v/v). CO pressure in (c): 1 bar for the high-[CO] curve and 0.05 bar for the solid curves. Note that the scale in panel a is expanded by a factor of approximately 100.<sup>89</sup>

In conclusion, the association coefficient for binding CO from the solvent at physiological temperatures to Mb is governed by the barrier at the heme. At low temperature, the CO rebinding rate depends on the conformational substate, which exhibit rate fluctuations, and make a non-exponential kinetics and heterogeneity of protein dynamics.

### 2.8 Outline

Myoglobin (Mb) has been used over decades as a model system for many experimental and theoretical studies particularly for kinetics-structural relationships. The heme, as a reaction center, is embedded within the protein and small ligands such as O<sub>2</sub>, CO, or NO can reversibly and covalently bind to the sixth coordination site on the distal side, of the heme. The binding and rebinding rate of such small molecules, for example CO, to the heme varies with temperature, pH, mutant, etc. and yield a lot of information about how structure, dynamics, and reactivity correlate to the environment conditions.  
43–51,58–64

Low-temperature experiments by Frauenfelder and coworkers in the 1970s demonstrated that, at cryogenic temperatures, rebinding of CO to myoglobin's heme cofactor after flash photolysis shows a strongly stretched exponential behavior, which is not observed at room temperature.<sup>69–72,84,87,90</sup> This behavior has been assigned to structural heterogeneity of myoglobin, resulting in different rebinding rates of CO, but no direct observation of this effect exists to date.

In recent years, the single-molecule methods for studying the kinetic behavior of individual molecular complexes have been developed in particular to determine heterogeneous behaviors in a system.<sup>91–92</sup> Moreover, dynamic heterogeneity, i.e. the dynamic switching of a protein between different states during the time of the experiment, makes it impossible to investigate an individual molecular dynamics in an ensemble measurement because may yield an average value for the experimental observables. Therefore, reducing the observed “ensemble” to a single molecule immediately solves the above-mentioned problems and make it possible to look individually the characteristics of each single molecule. Now, subpopulations can be easily resolved and also dynamic switching between different states can be observed. Recently, a new effort to take advantage of Förster Resonance Energy Transfer (FRET) technology to determine protein interaction and binding-rebinding reaction has emerged. In this approach, the donor emission is quenched through a non-fluorescent acceptor (protein) that can be used to study protein rebinding kinetics.<sup>93</sup> The method using quenched donor emission has more general applications as the acceptor can be a different state of myoglobin with different quenching effects for example deoxy-Mb, in which the CO is unbound to Mb, can act as a quencher and MbCO, where the CO is bound to Mb, has no quenching effects, or less. The binding and rebinding of diatomic molecules such as NO, and CO to the heme proteins have been studied through the change in the absorption of band III.<sup>94</sup>

The rebinding kinetics of CO can be measured precisely through quenching of a fluorescent dye attached to the myoglobin protein using FRET. Selection of the proper dye, position of labeling on the protein and the labelling method are crucial. For this purpose, not only an independent estimation of the FRET efficiency is needed to characterize protein re-binding but also the development of quantitative methodologies for steady-state and kinetic parameters of protein binding to the ligand is crucial. In the beginning of chapter 4, we focus on two different labelling methods,

different dye and different labeling sites on myoglobin. In the second part of Chapter 4, FRET experiments on dye-labelled Met-Mb, Deoxy-Mb and MbCO are reported. Chapter 4 describes ensemble FRET experiments of dye labeled -MbCO that demonstrate the feasibility of performing single molecule-FRET experiments.

Blue light breaks the Mb-CO bond with an efficiency of unity, which precludes FRET-based investigations of Mb-CO, as the bond between heme and CO would break after FRET. It means that before the carbonoxy state can be measured it has been already converted to the deoxy form. Therefore, the main question to be answered is whether the light emitted by the label can break the Mb-CO bond (due to the FRET) and with what efficiency it. Chapter 3 is about answering this question and proposing a new approach for the possibility of a FRET study of dye-labeled MbCO.

As discussed in Chapter 2, the myoglobin spectrum can be broadly split into three parts: the Soret band (300-500 nm), the Q-bands (500-700 nm) and the NIR bands (700-1000 nm). The quantum yield of breaking the Mb-CO bond is unity when it is illuminated by light with wavelengths below 600 nm. However, it is still unknown if illumination with light with a wavelength longer than 600 nm in particularly in the far red range breaks the MbCO bond or not and what its quantum yield would be?

In chapter 3, we describe experiments to determine the quantum yield of dissociation under far red illumination in order to determine if that region can be used for the FRET experiments.

In chapter 3, we propose an approach using the weak bands beyond 700 nm in the deoxy-Mb absorption spectrum to quench the fluorescence of a deep red dye. Crucially, these bands are absent in the spectrum of MbCO, preventing breakage of the CO bond due to resonant energy transfer from the excited dye. As the different states of Mb can be readily distinguished by their UV/Vis spectra, this method was selected to determine the dissociation quantum yield. To study photodissociation kinetics of MbCO, firstly Mb-CO was illuminated by near infra-red LED light. Then, following the absorption spectrum over time after each illumination cycle, we measure the kinetics of Mb-CO bond breaking. This experiment is repeated for blue light as a reference and the kinetics were compared.

The aim of Chapter 3 and 4 is to show the rebinding of CO to a protein at the single-molecule level can be done by performing single molecule-FRET experiments.

The histogram of FRET efficiencies and the corresponding donor-acceptor distances extracted from single-pair FRET data make it possible to follow the structural dynamics of biomolecules over time, and to distinguish the different surrounding environments of single molecules. However, in ensemble experiments, both the spatial and temporal heterogeneities are averaged out, and most of the information about the complexity of the system is lost. Therefore, in chapter 5, we study the FRET quenching in a system with a distribution of acceptors (ATTO575Q dye) around the donor (Azaoxatriangulenium, ADOTA dye) doped in thin polymeric layers at both ensemble and single molecule level at room temperature to measure and prove these heterogeneities in single molecule level which are averaged out in the ensemble.

## References

- (1) Wittenberg, B. A.; Wittenberg, J. B. Myoglobin-Mediated Oxygen Delivery to Mitochondria of Isolated Cardiac Myocytes. *Proc. Natl. Acad. Sci. U. S. A.* **1987**, *84* (21), 7503–7507.

- (2) Gros, G.; Wittenberg, B. A.; Jue, T. Myoglobin's Old and New Clothes: From Molecular Structure to Function in Living Cells. *J. Exp. Biol.* **2010**, 213 (16), 2713–2725.
- (3) Wittenberg, B. A.; Wittenberg, J. B. Transport of Oxygen in Muscle. *Annu. Rev. Physiol.* **1989**, 51, 857–878.
- (4) Gomez-Cambronero, J. THE OXYGEN DISSOCIATION CURVE OF HEMOGLOBIN: BRIDGING THE GAP BETWEEN BIOCHEMISTRY AND PHYSIOLOGY. *J. Chem. Educ.* **2001**, 78 (6), 757.
- (5) Antonini, E. INTERRELATIONSHIP BETWEEN STRUCTURE AND FUNCTION IN HEMOGLOBIN AND MYOGLOBIN. *Physiol. Rev.* **1965**, 45, 123–170.
- (6) Hemoglobin and Myoglobin | Integrative Medical Biochemistry Examination and Board Review | AccessPharmacy | McGraw Hill Medical <https://accesspharmacy.mhmedical.com/content.aspx?bookid=1696&sectionid=111398218> (accessed 2022 -01 -14).
- (7) Ryter, S. W.; Otterbein, L. E. Carbon Monoxide in Biology and Medicine. *BioEssays News Rev. Mol. Cell. Dev. Biol.* **2004**, 26 (3), 270–280.
- (8) Liu, Z.; Meng, H.; Huang, J.; Kwangwari, P.; Ma, K.; Xiao, B.; Li, L. Acute Carbon Monoxide Poisoning with Low Saturation of Carboxyhaemoglobin: A Forensic Retrospective Study in Shanghai, China. *Sci. Rep.* **2021**, 11 (1), 18554.
- (9) Bleecker, M. L. Carbon Monoxide Intoxication. *Handb. Clin. Neurol.* **2015**, 131, 191–203.
- (10) Miró, O.; Casademont, J.; Barrientos, A.; Urbano-Márquez, A.; Cardellach, F. Mitochondrial Cytochrome c Oxidase Inhibition during Acute Carbon Monoxide Poisoning. *Pharmacol. Toxicol.* **1998**, 82 (4), 199–202.
- (11) Kim, H. P.; Ryter, S. W.; Choi, A. M. K. CO as a Cellular Signaling Molecule. *Annu. Rev. Pharmacol. Toxicol.* **2006**, 46, 411–449.
- (12) Boehning, D.; Snyder, S. H. Circadian Rhythms. Carbon Monoxide and Clocks. *Science* **2002**, 298 (5602), 2339–2340.
- (13) Kobayashi, A.; Ishikawa, K.; Matsumoto, H.; Kimura, S.; Kamiyama, Y.; Maruyama, Y. Synergetic Antioxidant and Vasodilatory Action of Carbon Monoxide in Angiotensin II - Induced Cardiac Hypertrophy. *Hypertens. Dallas Tex* 1979 **2007**, 50 (6), 1040–1048.
- (14) Kendrew, J. C.; Bodo, G.; Dintzis, H. M.; Parrish, R. G.; Wyckoff, H.; Phillips, D. C. A Three-Dimensional Model of the Myoglobin Molecule Obtained by x-Ray Analysis. *Nature* **1958**, 181 (4610), 662–666.
- (15) Ordway, G. A.; Garry, D. J. Myoglobin: An Essential Hemoprotein in Striated Muscle. *J. Exp. Biol.* **2004**, 207 (Pt 20), 3441–3446.

- (16) Fleischer, E. B. Structure of Porphyrins and Metalloporphyrins. *Acc. Chem. Res.* **1970**, 3 (3), 105–112.
- (17) Porphyrin. *Wikipedia*; 2022.
- (18) Dolphin, D. *The Porphyrins V3: Physical Chemistry, Part A*; Elsevier, 2012.
- (19) Goldoni, A. Porphyrins: Fascinating Molecules with Biological Significance.
- (20) Eaton, W. A.; Hanson, L. K.; Stephens, P. J.; Sutherland, J. C.; Dunn, J. B. R. Optical Spectra of Oxy- and Deoxyhemoglobin. *J. Am. Chem. Soc.* **1978**, 100 (16), 4991–5003.
- (21) Bowen, W. J. The Absorption Spectra and Extinction Coefficients of Myoglobin. *J. Biol. Chem.* **1949**, 179 (1), 235–245.
- (22) Namuangruk, S.; Sirithip, K.; Rattanawan, R.; Keawin, T.; Kungwan, N.; Sudyodsuk, T.; Promarak, V.; Surakhot, Y.; Jungsuttiwong, S. Theoretical Investigation of the Charge-Transfer Properties in Different Meso-Linked Zinc Porphyrins for Highly Efficient Dye-Sensitized Solar Cells. *Dalton Trans. Camb. Engl.* 2003 **2014**, 43.
- (23) Gouterman, M. Spectra of Porphyrins. *J. Mol. Spectrosc.* **1961**, 6, 138–163.
- (24) Uddin, J. *Macro To Nano Spectroscopy*; BoD – Books on Demand, 2012.
- (25) Kingsbury, C. J.; Senge, M. O. The Shape of Porphyrins. *Coord. Chem. Rev.* **2021**, 431, 213760.
- (26) Cupane, A.; Leone, M.; Vitrano, E.; Cordone, L. Structural and Dynamic Properties of the Heme Pocket in Myoglobin Probed by Optical Spectroscopy. *Biopolymers* **1988**, 27 (12), 1977–1997.
- (27) Franzen, S.; Wallace-Williams, S. E.; Shreve, A. P. Heme Charge-Transfer Band III Is Vibronically Coupled to the Soret Band. *J. Am. Chem. Soc.* **2002**, 124 (24), 7146–7155.
- (28) Cordone, L.; Cupane, A.; Leone, M.; Vitrano, E. Thermal Behavior of the 760-Nm Absorption Band in Photodissociated Sperm Whale Carbonmonoxymyoglobin at Cryogenic Temperature: Dependence on External Medium. *Biopolymers* **1990**, 29 (3), 639–643.
- (29) Sharonov, Y. A.; Sharonova, N. A.; Figlovsky, V. A.; Grigorjev, V. A. A Comparison of the Heme Electronic States in Equilibrium and Nonequilibrium Protein Conformations of High-Spin Ferrous Hemoproteins Low Temperature Magnetic Circular Dichroism Studies. *Biochim. Biophys. Acta BBA - Protein Struct. Mol. Enzymol.* **1982**, 709 (2), 332–341.
- (30) Makinen, M. W.; Houtchens, R. A.; Caughey, W. S. Structure of Carboxymyoglobin in Crystals and in Solution. *Proc. Natl. Acad. Sci. U. S. A.* **1979**, 76 (12), 6042–6046.



- (31) Chance, B.; Lee, C.; Blasie, J. K. *Probes and Membrane Function*; Academic Press, 2013.
- (32) Olson, J. S.; Soman, J.; Phillips, G. N. Ligand Pathways in Myoglobin: A Review of Trp Cavity Mutations. *IUBMB Life* **2007**, *59* (8–9), 552–562.
- (33) Vos, M. H. Ultrafast Dynamics of Ligands within Heme Proteins. *Biochim. Biophys. Acta BBA - Bioenerg.* **2008**, *1777* (1), 15–31.
- (34) Shelby, M. L.; Wildman, A.; Hayes, D.; Mara, M. W.; Lestranger, P. J.; Cammarata, M.; Balducci, L.; Artamonov, M.; Lemke, H. T.; Zhu, D.; Seideman, T.; Hoffman, B. M.; Li, X.; Chen, L. X. Interplays of Electron and Nuclear Motions along CO Dissociation Trajectory in Myoglobin Revealed by Ultrafast X-Rays and Quantum Dynamics Calculations. *Proc. Natl. Acad. Sci.* **2021**, *118* (14), e2018966118.
- (35) Ionascu, D.; Gruia, F.; Ye, X.; Yu, A.; Rosca, F.; Beck, C.; Demidov, A.; Olson, J. S.; Champion, P. M. Temperature-Dependent Studies of NO Recombination to Heme and Heme Proteins. *J. Am. Chem. Soc.* **2005**, *127* (48), 16921–16934.
- (36) Sakakura, M.; Yamaguchi, S.; Hirota, N.; Terazima, M. Dynamics of Structure and Energy of Horse Carboxymyoglobin after Photodissociation of Carbon Monoxide. *J. Am. Chem. Soc.* **2001**, *123* (18), 4286–4294.
- (37) Sakakura, M.; Morishima, I.; Terazima, M. The Structural Dynamics and Ligand Releasing Process after the Photodissociation of Sperm Whale Carboxymyoglobin. *J. Phys. Chem. B* **2001**, *105* (42), 10424–10434.
- (38) Waleh, A.; Loew, G. H. Quantum Mechanical Studies of the Photodissociation of Carbonylheme Complexes. *J. Am. Chem. Soc.* **1982**, *104* (9), 2346–2351.
- (39) Barends, T. R. M.; Foucar, L.; Ardevol, A.; Nass, K.; Aquila, A.; Botha, S.; Doak, R. B.; Falahati, K.; Hartmann, E.; Hilpert, M.; Heinz, M.; Hoffmann, M. C.; Köfinger, J.; Koglin, J. E.; Kovacsova, G.; Liang, M.; Milathianaki, D.; Lemke, H. T.; Reinstein, J.; Roome, C. M.; Shoeman, R. L.; Williams, G. J.; Burghardt, I.; Hummer, G.; Boutet, S.; Schlichting, I. Direct Observation of Ultrafast Collective Motions in CO Myoglobin upon Ligand Dissociation. *Science* **2015**, *350* (6259), 445–450.
- (40) Harvey, J. N. DFT Computation of the Intrinsic Barrier to CO Geminate Recombination with Heme Compounds. *J. Am. Chem. Soc.* **2000**, *122* (49), 12401–12402.
- (41) Harvey, J. N. Spin-Forbidden CO Ligand Recombination in Myoglobin. *Faraday Discuss.* **2004**, *127* (0), 165–177.
- (42) Dunietz, B. D.; Dreuw, A.; Head-Gordon, M. Initial Steps of the Photodissociation of the CO Ligated Heme Group. *J. Phys. Chem. B* **2003**, *107* (23), 5623–5629.

- (43) Petrich, J. W.; Poyart, C.; Martin, J. L. Photophysics and Reactivity of Heme Proteins: A Femtosecond Absorption Study of Hemoglobin, Myoglobin, and Protoheme. *Biochemistry* **1988**, 27 (11), 4049–4060.
- (44) Srajer, V.; Teng, T.; Ursby, T.; Pradervand, C.; Ren, Z.; Adachi, S.; Schildkamp, W.; Bourgeois, D.; Wulff, M.; Moffat, K. Photolysis of the Carbon Monoxide Complex of Myoglobin: Nanosecond Time-Resolved Crystallography. *Science* **1996**, 274 (5293), 1726–1729.
- (45) Henry, E. R.; Sommer, J. H.; Hofrichter, J.; Eaton, W. A. Geminate Recombination of Carbon Monoxide to Myoglobin. *J. Mol. Biol.* **1983**, 166 (3), 443–451.
- (46) Levantino, M.; Schirò, G.; Lemke, H. T.; Cottone, G.; Glowina, J. M.; Zhu, D.; Chollet, M.; Ihee, H.; Cupane, A.; Cammarata, M. Ultrafast Myoglobin Structural Dynamics Observed with an X-Ray Free-Electron Laser. *Nat. Commun.* **2015**, 6 (1), 6772.
- (47) Levantino, M.; Lemke, H. T.; Schirò, G.; Glowina, M.; Cupane, A.; Cammarata, M. Observing Heme Doming in Myoglobin with Femtosecond X-Ray Absorption Spectroscopy. *Struct. Dyn.* **2015**, 2 (4), 041713.
- (48) Dartigalongue, T.; Hache, F. Observation of Sub-100 Ps Conformational Changes in Photolyzed Carbonmonoxy-Myoglobin Probed by Time-Resolved Circular Dichroism. In *11th Congress of the European Society for Photobiology*; oral; Aix les Bains, France, 2005.
- (49) Findsen, E. W.; Scott, T. W.; Chance, M. R.; Friedman, J. M.; Ondrias, M. R. Picosecond Time-Resolved Raman Studies of Photodissociated Carboxymyoglobin. *J. Am. Chem. Soc.* **1985**, 107 (11), 3355–3357.
- (50) Ferrante, C.; Pontecorvo, E.; Cerullo, G.; Vos, M. H.; Scopigno, T. Direct Observation of Subpicosecond Vibrational Dynamics in Photoexcited Myoglobin. *Nat. Chem.* **2016**, 8 (12), 1137–1143.
- (51) Franzen, S.; Bohn, B.; Poyart, C.; Martin, J. L. Evidence for Sub-Picosecond Heme Doming in Hemoglobin and Myoglobin: A Time-Resolved Resonance Raman Comparison of Carbonmonoxy and Deoxy Species. *Biochemistry* **1995**, 34 (4), 1224–1237.
- (52) Ostermann, A.; Waschipky, R.; Parak, F. G.; Nienhaus, G. U. Ligand Binding and Conformational Motions in Myoglobin. *Nature* **2000**, 404 (6774), 205–208.
- (53) Schoenborn, B. P.; Watson, H. C.; Kendrew, J. C. Binding of Xenon to Sperm Whale Myoglobin. *Nature* **1965**, 207 (4992), 28–30.
- (54) Bossa, C.; Anselmi, M.; Roccatano, D.; Amadei, A.; Vallone, B.; Brunori, M.; Di Nola, A. Extended Molecular Dynamics Simulation of the Carbon Monoxide Migration in Sperm Whale Myoglobin. *Biophys. J.* **2004**, 86 (6), 3855–3862.
- (55) Schmidt, M.; Nienhaus, K.; Pahl, R.; Krasselt, A.; Anderson, S.; Parak, F.; Nienhaus, G. U.; Šrajer, V. Ligand Migration Pathway and Protein Dynamics in

- Myoglobin: A Time-Resolved Crystallographic Study on L29W MbCO. *Proc. Natl. Acad. Sci.* **2005**, 102 (33), 11704–11709.
- (56) Samuni, U.; Dantsker, D.; Roche, C. J.; Friedman, J. M. Ligand Recombination and a Hierarchy of Solvent Slaved Dynamics: The Origin of Kinetic Phases in Hemeproteins. *Gene* **2007**, 398 (1), 234–248.
- (57) Falahati, K.; Tamura, H.; Burghardt, I.; Huix-Rotllant, M. Ultrafast Carbon Monoxide Photolysis and Heme Spin-Crossover in Myoglobin via Nonadiabatic Quantum Dynamics. *Nat. Commun.* **2018**, 9 (1), 4502.
- (58) Murray, L. P.; Hofrichter, J.; Henry, E. R.; Eaton, W. A. Time-Resolved Optical Spectroscopy and Structural Dynamics Following Photodissociation of Carbonmonoxyhemoglobin. *Biophys. Chem.* **1988**, 29 (1–2), 63–76.
- (59) Hamdane, D.; Kiger, L.; Hui-Bon-Hoa, G.; Marden, M. C. Kinetics inside the Protein: Shape of the Geminate Kinetics in Myoglobin. *J. Phys. Chem. B* **2011**, 115 (14), 3919–3923.
- (60) Kleinert, T.; Doster, W.; Leyser, H.; Petry, W.; Schwarz, V.; Settles, M. Solvent Composition and Viscosity Effects on the Kinetics of CO Binding to Horse Myoglobin. *Biochemistry* **1998**, 37 (2), 717–733. <https://doi.org/10.1021/bi971508q>.
- (61) Angeloni, L.; Feis, A. Protein Relaxation in the Photodissociation of Myoglobin–CO Complexes. *Photochem. Photobiol. Sci.* **2003**, 2 (7), 730–740.
- (62) Ansari, A.; Jones, C. M.; Henry, E. R.; Hofrichter, J.; Eaton, W. A. Conformational Relaxation and Ligand Binding in Myoglobin. *Biochemistry* **1994**, 33 (17), 5128–5145.
- (63) Jongeward, K. A.; Magde, Douglas.; Taube, D. J.; Marsters, J. C.; Traylor, T. G.; Sharma, V. S. Picosecond and Nanosecond Geminate Recombination of Myoglobin with Carbon Monoxide, Oxygen, Nitric Oxide and Isocyanides. *J. Am. Chem. Soc.* **1988**, 110 (2), 380–387.
- (64) Dartigalongue, T.; Niezborala, C.; Hache, F. Subpicosecond UV Spectroscopy of Carbonmonoxy-Myoglobin: Absorption and Circular Dichroism Studies. *Phys. Chem. Chem. Phys. PCCP* **2007**, 9, 1611–1615.
- (65) Schmidt, M.; Nienhaus, K.; Pahl, R.; Krasselt, A.; Anderson, S.; Parak, F.; Nienhaus, G. U.; Srajer, V. Ligand Migration Pathway and Protein Dynamics in Myoglobin: A Time-Resolved Crystallographic Study on L29W MbCO. *Proc. Natl. Acad. Sci. U. S. A.* **2005**, 102 (33), 11704–11709.
- (66) Maragliano, L.; Cottone, G.; Ciccotti, G.; Vanden-Eijnden, E. Mapping the Network of Pathways of CO Diffusion in Myoglobin. *J. Am. Chem. Soc.* **2010**, 132 (3), 1010–1017.
- (67) Brunori, M.; Bourgeois, D.; Vallone, B. The Structural Dynamics of Myoglobin. *J. Struct. Biol.* **2004**, 147 (3), 223–234. <https://doi.org/10.1016/j.jsb.2004.04.008>.

- 
- (68) Tetreau, C.; Lavalette, D. Dominant Features of Protein Reaction Dynamics: Conformational Relaxation and Ligand Migration. *Biochim. Biophys. Acta BBA - Gen. Subj.* **2005**, 1724 (3), 411–424.
- (69) Austin, R. H.; Beeson, K. W.; Eisenstein, L.; Frauenfelder, H.; Gunsalus, I. C. Dynamics of Ligand Binding to Myoglobin. *Biochemistry* **1975**, 14 (24), 5355–5373.
- (70) Frauenfelder, H.; Wolynes, P. G.; Austin, R. H. Biological Physics. *Rev. Mod. Phys.* **1999**, 71 (2), S419–S430.
- (71) Frauenfelder, H.; Wolynes, P. G. Rate Theories and Puzzles of Hemeprotein Kinetics. *Science* **1985**, 229 (4711), 337–345.
- (72) Frauenfelder, H.; Sligar, S. G.; Wolynes, P. G. The Energy Landscapes and Motions of Proteins. *Science* **1991**, 254 (5038), 1598–1603.
- (73) Reynolds, A. H.; Rentzepis, P. M. Kinetics and Temperature Dependence of Carboxymyoglobin Ligand Photodissociation. *Biophys. J.* **1982**, 38 (1), 15–18.
- (74) Ansari, A.; Berendzen, J.; Bowne, S. F.; Frauenfelder, H.; Iben, I. E.; Sauke, T. B.; Shyamsunder, E.; Young, R. D. Protein States and Proteinquakes. *Proc. Natl. Acad. Sci.* **1985**, 82 (15), 5000–5004.
- (75) Tomita, A.; Sato, T.; Nozawa, S.; Koshihara, S.; Adachi, S. Tracking Ligand-Migration Pathways of Carbonmonoxy Myoglobin in Crystals at Cryogenic Temperatures. *Acta Crystallogr. A* **2010**, 66 (Pt 2), 220–228.
- (76) Tian, W. D.; Sage, J. T.; Champion, P. M.; Chien, E.; Sligar, S. G. Probing Heme Protein Conformational Equilibration Rates with Kinetic Selection. *Biochemistry* **1996**, 35 (11), 3487–3502. <https://doi.org/10.1021/bi952474u>.
- (77) Olson, J. S.; Phillips, G. N. Kinetic Pathways and Barriers for Ligand Binding to Myoglobin. *J. Biol. Chem.* **1996**, 271 (30), 17593–17596.
- (78) Nienhaus, K.; Deng, P.; Kriegl, J. M.; Nienhaus, G. U. Structural Dynamics of Myoglobin: Effect of Internal Cavities on Ligand Migration and Binding. *Biochemistry* **2003**, 42 (32), 9647–9658.
- (79) Reynolds, A. H.; Rand, S. D.; Rentzepis, P. M. Mechanisms for Excited State Relaxation and Dissociation of Oxymyoglobin and Carboxymyoglobin. *Proc. Natl. Acad. Sci. U. S. A.* **1981**, 78 (4), 2292–2296.
- (80) Henry, E. R.; Sommer, J. H.; Hofrichter, J.; Eaton, W. A. Geminate Recombination of Carbon Monoxide to Myoglobin. *J. Mol. Biol.* **1983**, 166 (3), 443–451.
- (81) Bredenbeck, J.; Helbing, J.; Nienhaus, K.; Nienhaus, G. U.; Hamm, P. Protein Ligand Migration Mapped by Nonequilibrium 2D-IR Exchange Spectroscopy. *Proc. Natl. Acad. Sci.* **2007**, 104 (36), 14243–14248.

- (82) Nienhaus, K.; Olson, J. S.; Franzen, S.; Nienhaus, G. U. The Origin of Stark Splitting in the Initial Photoproduct State of MbCO. *J. Am. Chem. Soc.* **2005**, *127* (1), 40–41.
- (83) Ansari, A.; Berendzen, J.; Braunstein, D.; Cowen, B. R.; Frauenfelder, H.; Hong, M. K.; Iben, I. E.; Johnson, J. B.; Ormos, P.; Sauke, T. B. Rebinding and Relaxation in the Myoglobin Pocket. *Biophys. Chem.* **1987**, *26* (2–3), 337–355.
- (84) Sakakura, M.; Yamaguchi, S.; Hirota, N.; Terazima, M. Dynamics of Structure and Energy of Horse Carboxymyoglobin after Photodissociation of Carbon Monoxide. *J. Am. Chem. Soc.* **2001**, *123* (18), 4286–4294.
- (85) Agmon, N.; Hopfield, J. J. CO Binding to Heme Proteins: A Model for Barrier Height Distributions and Slow Conformational Changes. *J. Chem. Phys.* **1983**, *79* (4), 2042.
- (86) [https://en.wikipedia.org/wiki/Hans\\_Frauenfelder](https://en.wikipedia.org/wiki/Hans_Frauenfelder)
- (87) Frauenfelder, H.; Sligar, S. G.; Wolynes, P. G. The Energy Landscapes and Motions of Proteins. *Science, New Series*, *254* (5038), 1598–1603.
- (88) Manz, C.; Kobitski, A. Y.; Samanta, A.; Nienhaus, K.; Jäschke, A.; Nienhaus, G. U. Exploring the energy landscape of a SAM-I riboswitch. *J. Biol. Phys.* **2021**, *47*, 371–386.
- (89) Steinbach P. J.; Ansari, A.; Berendzen, J.; Braunstein, D.; Chu, K.; Cowen, B. R.; Ehrenstein, D.; Frauenfelder, H.; Johnson, J. B. Ligand binding to heme proteins: connection between dynamics and function. *Biochemistry* **1991**, *30* (16), 3988–4001.
- (90) Austin, R. H.; Beeson, K. W.; Eisenstein, L.; Frauenfelder, H.; Gunsalus, I. C. Dynamics of Ligand Binding to Myoglobin. *Biochemistry* **1975**, *14* (24), 5355–5373.
- (91) Sustarsic, M.; Kapanidis, A. N. Taking the Ruler to the Jungle: Single-Molecule FRET for Understanding Biomolecular Structure and Dynamics in Live Cells. *Curr. Opin. Struct. Biol.* **2015**, *34*, 52–59.
- (92) Pradhan, B.; Engelhard, C.; Mulken, S. V.; Miao, X.; Canters, G. W.; Orrit, M. Single Electron Transfer Events and Dynamical Heterogeneity in the Small Protein Azurin from *Pseudomonas Aeruginosa*. *Chem. Sci.* **2020**, *11* (3), 763–771.
- (93) Penjweini, R.; Andreoni, A.; Rosales, T.; Kim, J.; Brenner, M. D.; Sackett, D. L.; Chung, J. H.; Knutson, J. R. Intracellular Oxygen Mapping Using a Myoglobin-MCherry Probe with Fluorescence Lifetime Imaging. *J. Biomed. Opt.* **2018**, *23* (10), 1–14.
- (94) Yoo, B.-K.; Kruglik, S. G.; Lamarre, I.; Martin, J.-L.; Negrier, M. Absorption band III kinetics probe the picosecond heme iron motion triggered by nitric oxide binding to hemoglobin and myoglobin. *J. Phys. Chem. B* **2012**, *116* (13), 4106–4114.

# 3

## Estimation of the dissociation quantum yield of the Mb-CO bond

*In this chapter, we describe experiments to estimate the quantum yield of MbCO dissociation using far red illumination in order to determine if that region can be used for an FRET experiments. The aim of Chapter 3 and 4 is to show that the rebinding of CO to protein at the single-molecule level can be done by performing single molecule-FRET experiments. In Chapter 3, we propose an approach using the weak bands beyond 700 nm in the deoxy-Mb absorption spectrum to quench the fluorescence of a deep red dye. Crucially, these bands are absent in the spectrum of MbCO, preventing breakage of the CO bond due to resonant energy transfer from the excited dye. As the different states of Mb can be readily distinguished by their UV/Vis spectra, this method was selected to determine the dissociation quantum yield.*

### 3.1 Introduction

In order to detect the activity of proteins, fluorescence spectroscopy is a reliable detection method. For example, azurin is a metalloprotein containing a copper center that can actively participate in electron transfer reactions. This copper site determines the redox property of azurin. The oxidized copper site ( $\text{Cu}^{2+}$ ) has a specific absorption spectrum in the area of 590-650 nm originating from  $\pi \rightarrow \pi^*$  transitions (Figure 3.1A). When the redox state of the prosthetic group switches to another state ( $\text{Cu}^{2+} \leftrightarrow \text{Cu}^+$ ) absorption in the visible part of the spectrum disappears. Because of the weakness of absorption spectrum for the oxidized copper site ( $\text{Cu}^{2+}$ ) in the area of 590-650 nm, it is difficult to follow the change of the oxidation state of Cu in azurin by monitoring the change of absorption spectra. However, this change on the absorption spectrum is key to monitoring the oxidation state of azurin by fluorescence spectroscopy. For example, attachment of a fluorescent molecule to the protein surface at a specific distance makes it possible to monitor the fluorescence emission of a single-dye-labeled azurin molecule by means of Förster Resonance Energy Transfer (FRET).<sup>1</sup> In fact, the oxidized form of azurin has more overlap with the emission spectra of a dye (for example Atto 655) compared to the reduced form of azurin, thus more fluorescence quenching is monitored due to the energy transfer from the labeled dye to the Cu-center (Figure 3.1B).<sup>2</sup>

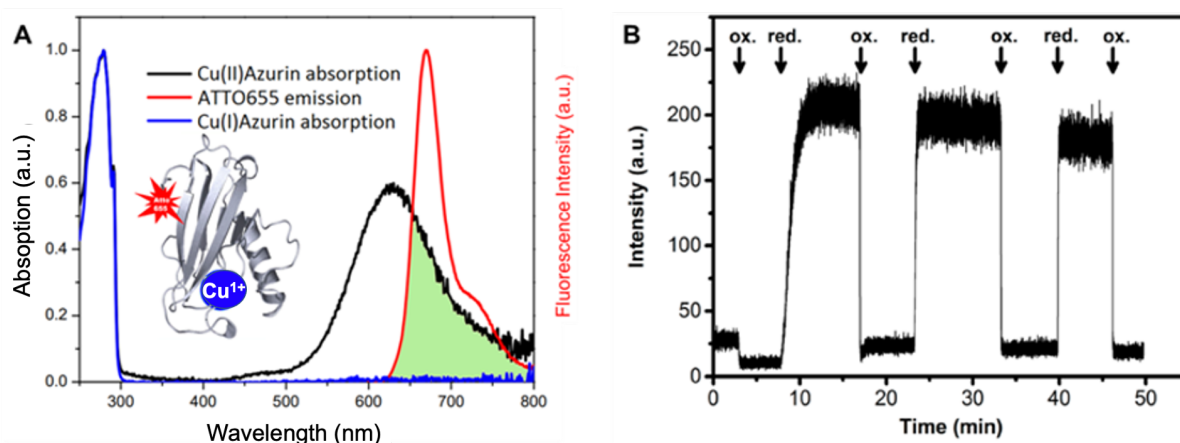


**Figure 3.1** (A) Absorption spectrum (black curve) of the oxidized form of azurin ( $\text{Cu}^{2+}$ ), emission spectra of Atto 655 dye (red curve), and the green colour area is a visualization of the overlap between the absorption spectrum of the oxidized form of azurin ( $\text{Cu}^{2+}$ ) and the emission spectrum of Atto 655 (B) The fluorescence intensity of azurin labeled with Atto 655 in solution (25 nM), the oxidized state ( $\text{Cu}^{2+}$ ) is quenched due to FRET and the reduced state ( $\text{Cu}^+$ ) has high fluorescence intensity of the Atto655 dye due to the absence of FRET.<sup>2</sup>

In the same way, we will explore the use of FRET to monitor the kinetics of rebinding of small molecules to proteins. For example, myoglobin is another metalloprotein (Mb) that has been used as a model system for many experiments, particularly for kinetics-structural relationships. It has a heme containing an iron reaction center that can bind to small ligands such as  $\text{O}_2$ , CO, or NO reversibly.

In the case of myoglobin, the binding or unbinding of CO ligand to the heme reaction center gives rise to a different absorption spectrum (Figure 3.2). Thus, by labeling myoglobin with a proper dye, the overlap between the emission spectrum of the dye-labeled myoglobin with the absorption spectrum of these different states (with bound

or unbound CO) is changed and, due to the different FRET efficiency, it is possible to study the CO binding and rebinding kinetics. When the CO molecule in the heme pocket of myoglobin dissociates, the fluorescence intensity of the dye attached to the MbCO is quenched due to the stronger energy transfer from the dye label to the heme center of deoxy-Mb (Figure 3.3).

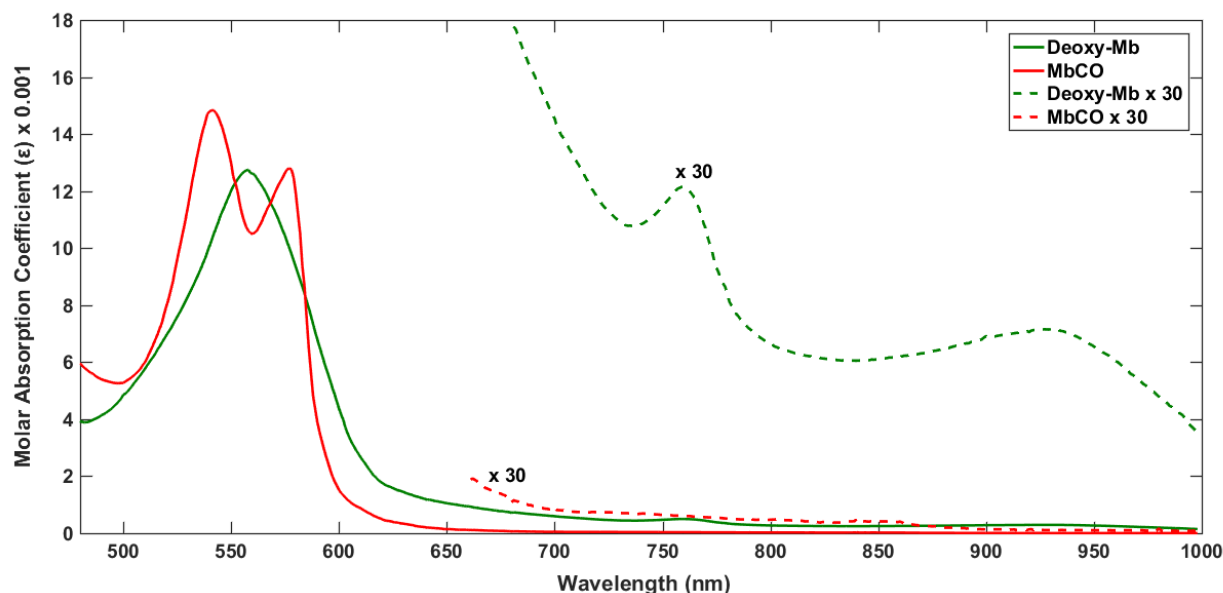


**Figure 3.2** Absorption spectrum of the Q-bands (500-700 nm) and NIR bands (700-1000 nm) for two Mb states: deoxy-Mb (green), and MbCO (red) from horse heart Mb at room temperature, in Sørensen's phosphate buffer (0.05 mM) with pH 6.8-8. The dashed lines represent the 30x enlarged spectra. <sup>3</sup>

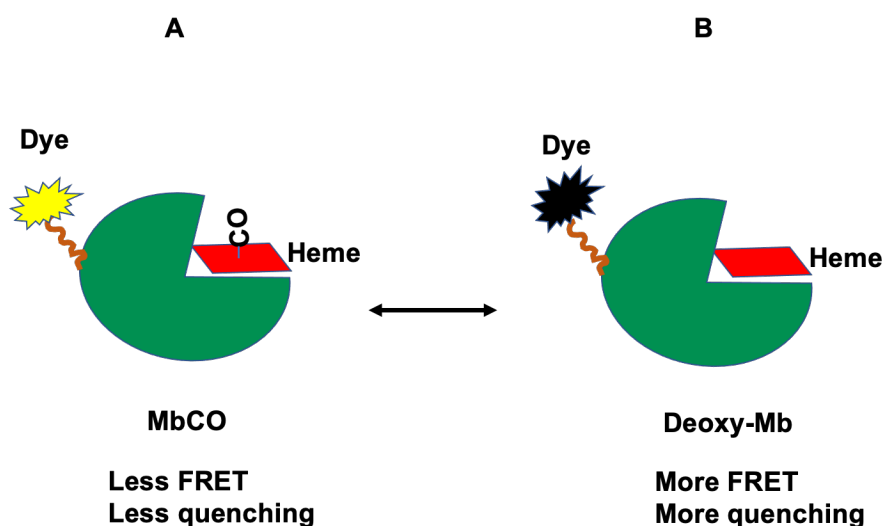


**Figure 3.3** A schematic illustration of MbCO containing CO bound to the heme (red) (A), and deoxy-Mb in which CO is unbound to the heme (B). The fluorescence intensity of a suitable dye attached to MbCO is quenched due to stronger FRET when the CO molecule detaches from the heme, due to energy transfer to the heme center of deoxy-Mb.

The single-molecule FRET (smFRET) approach has been widely used to determine kinetic rates of protein reactions. Proteins can be specifically labeled by a dye enabling



smFRET measurements. The ability to measure accurate distances and kinetics with smFRET enables studies of dynamics and structural biology and monitoring the biomolecular heterogeneities through the behavior of individual molecules.<sup>1</sup>

#### 3.1.1 Does near infra-red light ( $\lambda > 700$ nm) break the Mb-CO bond?

It is well known that a wide spectral range of visible light, particularly  $400 < \lambda < 550$  nm, breaks the Mb-CO bond with high efficiency, which precludes using FRET-based investigations of CO dissociation in this spectral region. We therefore investigated a strategy involving the near infra-red spectral region,  $\lambda > 700$  nm. If a labeled MbCO under red-light illumination breaks the Mb-CO with high efficiency, probing the absorption of MbCO with red light would dissociate the complex to regenerate deoxy-Mb, making it difficult to monitor CO rebinding by fluorescence spectroscopy using FRET spectroscopy. For this reason, it is essential to estimate the quantum yield for photodissociation of the Mb-CO bond under red-light illumination.

As discussed in Chapter 2, the myoglobin spectrum can be broadly split into three regions: the Soret band (300-500 nm), the Q-bands (500-700 nm) and the NIR bands I, II, and III (700-1000 nm) (Figure 3.4). The quantum yield of Mb-CO bond breaking is close to unity when under illumination by light with a wavelength shorter than 600 nm, but it is still unknown whether illumination with  $\lambda > 700$  nm (Figure 1) breaks the MbCO bond, and with which quantum yield. In this chapter, we report our measurements of the dissociation quantum yield of Mb-CO in the near infra-red.

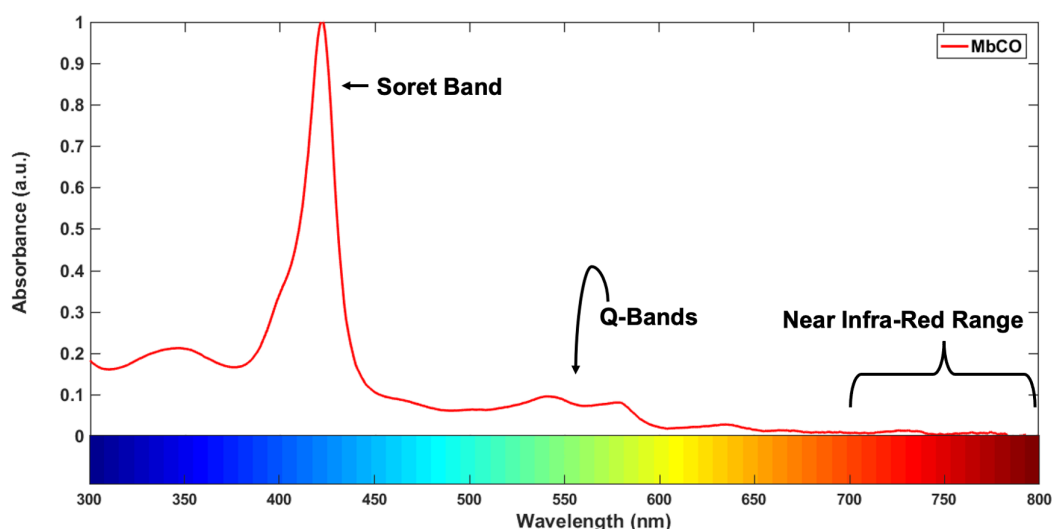


**Figure 3.4** Absorption spectrum of MbCO from the uV to the near infra-red

If the quantum yield in this far-red area would be significantly less than 1, it might be possible to detect the signal of the dye label emitting in the far red (700-1000 nm). It would thus enable us to distinguish between the carboxy and deoxy forms and thereby to monitor the kinetics of the CO rebinding to a single myoglobin molecule. In this chapter, we focus on ensemble experiments only.

#### 3.1.2 Preparation of MbCO and deoxy-Mb from Met-Mb

The first step is the preparation of MbCO from the commercially available form of myoglobin, met-Mb, in which the heme contains the ferric iron ( $\text{Fe}^{3+}$ ). Met-Mb ( $\text{Fe}^{3+}$ ) is

reduced to the deoxy form in which the iron is in the  $\text{Fe}^{2+}$  oxidation state. Incubation with CO then yields MbCO (Figure 3.5).

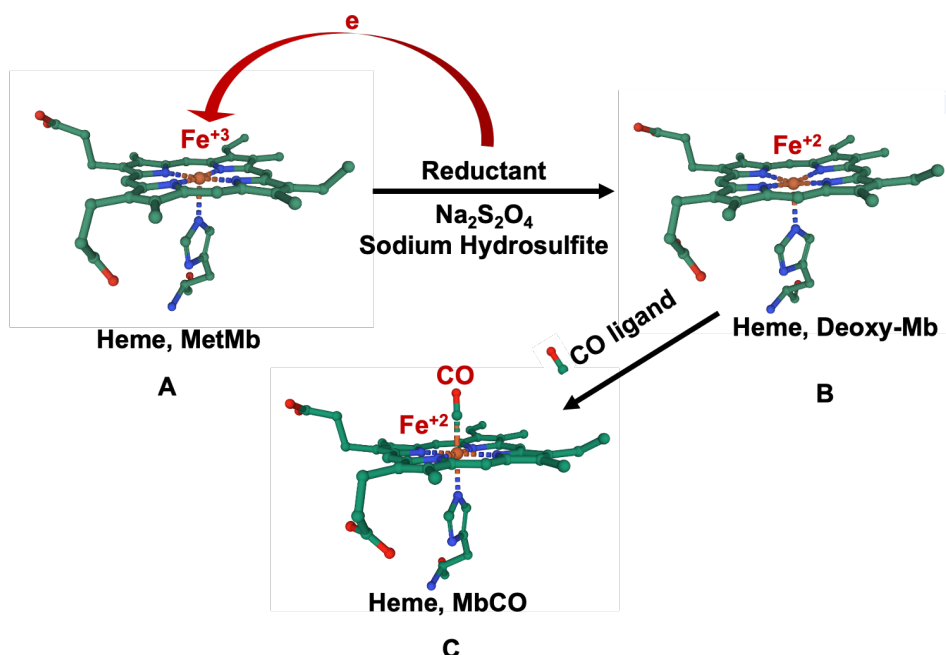


**Figure 3.5** Schematics of MbCO preparation from met-Mb. (A) The heme in met-Mb is reduced with sodium hydrosulfite, making (B) deoxy-mb with ferrous iron. (C) Incubation with CO yields MbCO. The images of hemes have been exported from the PDB (Horse heart 1WLA, 5D5R, and 1A6G for met-Mb, deoxy-Mb, and MbCO respectively)

### 3.1.3 Photodissociation methods

The three standard methods for the measurement of ligand photolysis are: (i) the kinetic method, (ii) the steady-state method, and (iii) the pulse photolysis method. The first two focus on bimolecular rebinding and use constant illumination so that either the rates of transition between the photostationary states, or the equilibrium ligand binding curves are measured. The measured rate is the sum of the association and dissociation rates and the yield is the overall “bimolecular dissociation yield”. The pulse photodissociation method relates to the rebinding kinetics and utilizes a pulse that is short compared to the ligand recombination time. Pulse widths in the millisecond to microsecond range are sufficient to measure bimolecular dissociation yields. Studies with nanosecond or faster time resolution found that a photodissociated ligand can remain in the heme pocket and recombine geminately. The bimolecular dissociation yield is then expressed as  $\eta_b = Y\eta_0$ , where  $\eta_0$  is the ( $t = 0$ ) photodissociation yield (sometimes referred to as the intrinsic quantum yield of photodissociation) and  $Y$  is the fraction of ligands that escape to the solution and do not undergo geminate rebinding. As the different states of Mb can be readily distinguished by their UV/Vis spectra, UV-Vis spectroscopy was selected to measure the dissociation rate of MbCO and to determine the dissociation quantum yield.

## 3.2 Results

### 3.2.1 Preparation of deoxy-Mb and MbCO from met-Mb

To reduce met-Mb to deoxy-Mb, it is important to prepare the sample in an oxygen-free environment. Therefore, first, the met-Mb solution was degassed in an absorption cell (cuvette). In this study, two different methods have been tested to prepare an oxygen-free solution and to prepare deoxy-Mb and MbCO: glass-apparatus and the nitrogen-box.

The home-made glass apparatus is shown in Figure 3.6. The sample cell was connected to a glass setup (Figure 3.6 B, and C) to remove oxygen by alternating  $N_2$  bubbling and evacuating during 10 min. Sodium hydrosulfite crystals (sodium dithiote, DTT) as reducing agent were placed in a side arm of a modified glass tube (Figure 3.6 A) and phosphate buffer was added to the mixing chamber. The modified glass tube was connected to the same glass setup the buffer was degassed and the glass were tilted to add the sodium hydrosulfite in the side arm to the solution, producing an oxygen-free sodium hydrosulfite reducing agent. Using a Hamilton syringe, the reducing solution of sodium hydrosulfite was transferred anaerobically to the met-Mb absorption cell to produce deoxy-Mb. MbCO was prepared by a similar treatment starting from deoxy-Mb, omitting the addition of the reducing agent and replacing  $N_2$  with CO.

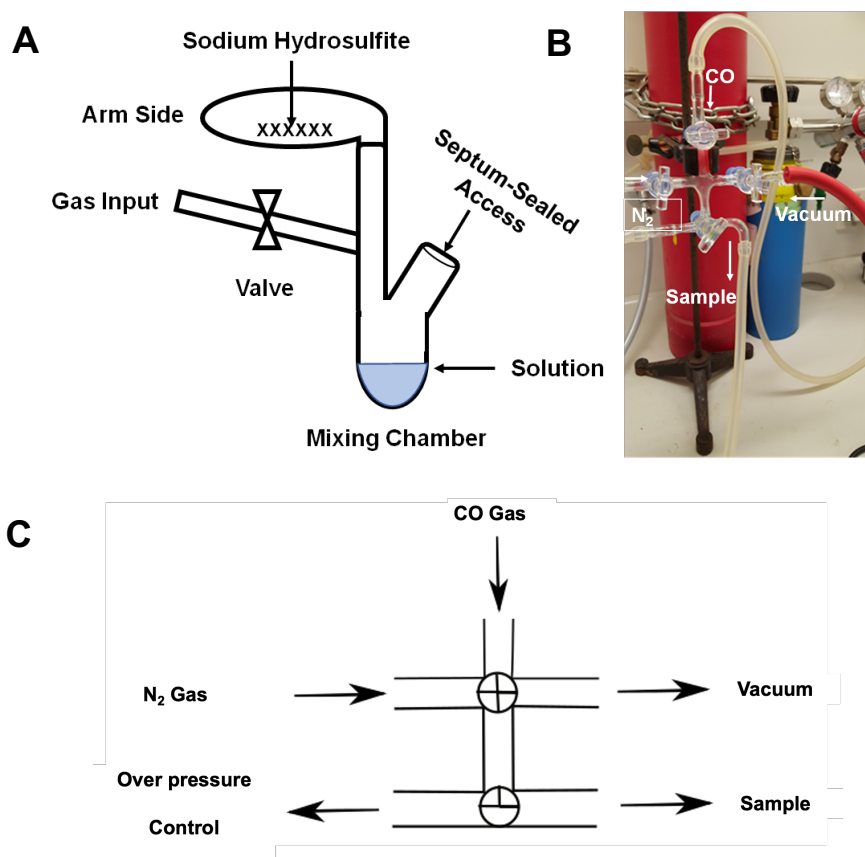


**Figure 3.6** Scheme of setup for preparation of deoxy-Mb and MbCO; (A) Modified glass tube for met-Mb reduction shows the side arm, gas input, valve, mixing chamber and septum-sealed access, (B) CO gas setup, (C) Sketch of CO gas setup shows the CO and  $N_2$  gas entrances, vacuum, sample position, and  $N_2$  overpressure control.

The second method to prepare deoxy-Mb and MbCO samples consists of bubbling the buffer solution with  $N_2$  inside a cuvette sealed with a septum, using nitrogen from a gas cylinder and then performing the reactions inside a nitrogen-filled dry box. Dissolving met-Mb in the buffer results in a brown-colored solution (Figure 3.7, A). Met-Mb is then reacted with DTT in an oxygen-free atmosphere producing deoxy-Mb with a purple color (Figure 3.7, B). Then bubbling the solution in the cuvette with CO from a Minican for 10 min converts deoxy-Mb to MbCO resulting in a red-colored solution (Figure 3.7, C).

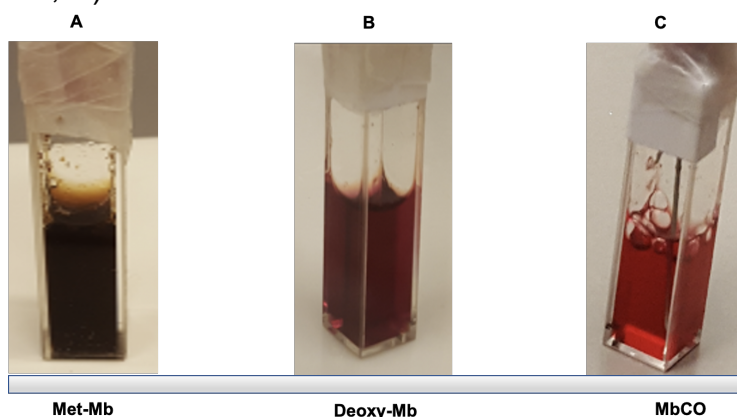


**Figure 3.7** The sealed cuvette. (A) brown solution of met-Mb, (B) deoxy-Mb solution with purple color, and (C) MbCO solution with red color.

Both methods produced pure MbCO samples but the second procedure is more straightforward and safer although it takes more time. All MbCO used in the experiments in this chapter was prepared using the nitrogen box system.

The changes in absorption spectra (Chapter 2, section 2.1) of Mb can be used to determine the state of the myoglobin present in the solution. The successful preparation of deoxy-Mb and MbCO was verified by measuring the absorption spectra with a UV-Vis spectrophotometer (Figures 3.8 and 3.9). It should be noted that because of the low extinction coefficient of band III in deoxy-Mb, it was only observed at high concentrations of deoxy-Mb (1 mM).

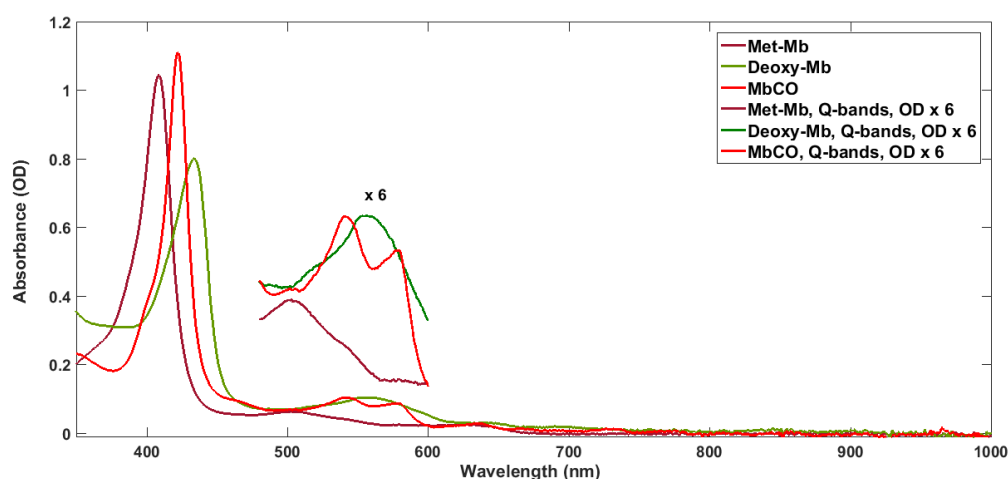


**Figure 3.8** Absorption spectrum of met-Mb (brown) (Soret band at 409 nm), deoxy-Mb (green) (Soret band at 433 nm), and MbCO (red) (Soret band at 423 nm). These spectra all are results of our experiments.

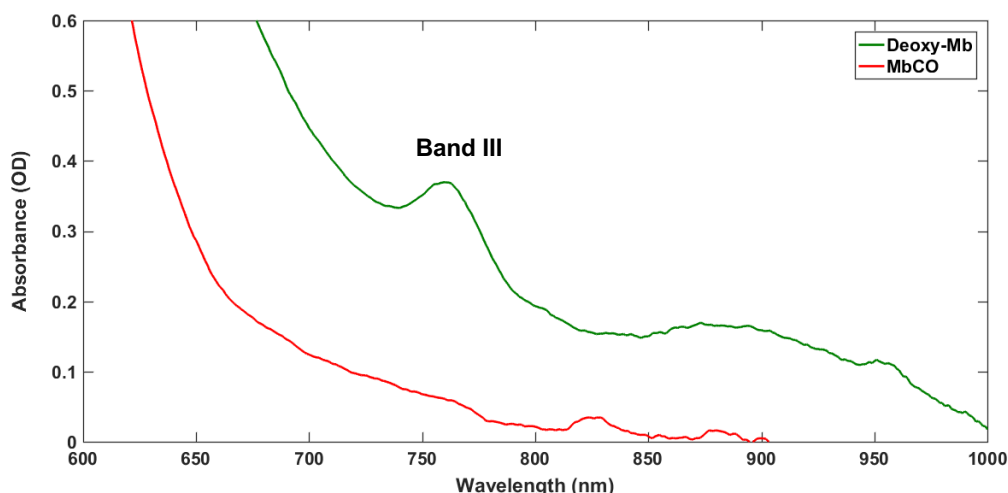


**Figure 3.9** Absorption spectra of 1mM deoxy-Mb (blue) (Band III occurs at 760 nm) and MbCO (red) (1mM) in PBS, pH=7.2, at room temperature. These spectra are the results of our experiments.

#### 3.2.2 Design of the setup

To study the photodissociation kinetics of Mb-CO, a UV-Vis cell holder was used consisting of a cuvette, a blue or red filter, and blue or near infra-red LEDs. This cell allows for illumination inside the UV-Vis spectrometer with high illumination efficiency of the sample. The cell allows the use of the UV-Vis spectrometer to measure the absorption spectrum of the solution in the cuvette and to follow the kinetics of dissociation/rebinding (Figure 3.10).

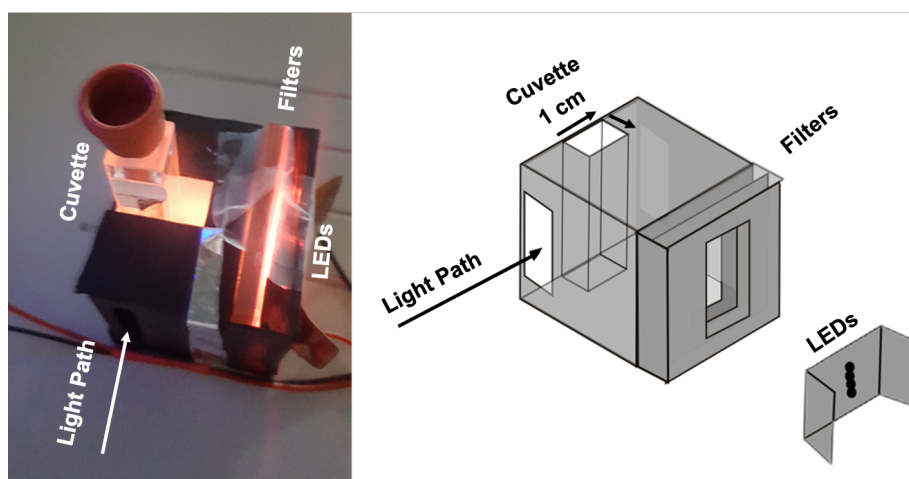


**Figure 3.10** The UV-Vis sample holder consists of a cuvette positioner, filters, a LED holder. The light path of the spectrophotometer is indicated. Irradiation of the sample in the cuvette by LED light follows a perpendicular path.

#### 3.2.3 Study of photodissociation kinetics of Mb-CO and designed experiment

The geminate rebinding of photodissociated CO in the vicinity of the heme at room temperature is fast compared to the recombination of CO from solution to the heme. Therefore, we ignore the geminate rebinding and only focus on the recombination of

CO from solution to the heme pocket. To study the kinetics of MbCO photodissociation, it is essential to slow down the recombination kinetics of the escaped CO molecule in solution to the heme. In this regard, CO molecules after escaping from the protein should be removed from the vicinity of the formed deoxy-Mb. In our first attempts, pure nitrogen gas was bubbled during illumination to remove any dissociated CO near the myoglobin protein. It appeared that even removing of CO molecule in solution during photodissociation by bubbling pure nitrogen gas does not completely prevent the recombination of CO that has escaped to the solution. Moreover, bubbling nitrogen gas removed some amount of protein from the detection area and caused an error in the measurement of absorption spectra. Alternatively, the bubbling may have caused denaturation of some of the protein during the experiment. A different approach to prevent CO recombination to the heme is to control this reaction chemically. During photodissociation of MbCO, deoxy-Mb is formed. Thus if an oxidant with a fast rate converts the deoxy-Mb to another form, for example met-Mb, not only is the recombination reaction prevented, but we also reach a simpler mixture solution after illumination, which facilitates the determination of the exact amount of MbCO converted to deoxy-Mb. We can thus more easily calculate the photodissociation quantum yield of MbCO with red-LED illumination by comparing it to that with blue-LED illumination measured in a control experiment.  $\text{H}_2\text{O}_2$  is an oxidant which is small enough to enter the iron cavity in the protein and to convert deoxy-Mb (containing iron (II)) by supplying an electron to met-Mb (containing iron (III)) (Figure 3.11 B,  $B \rightarrow C$ ).

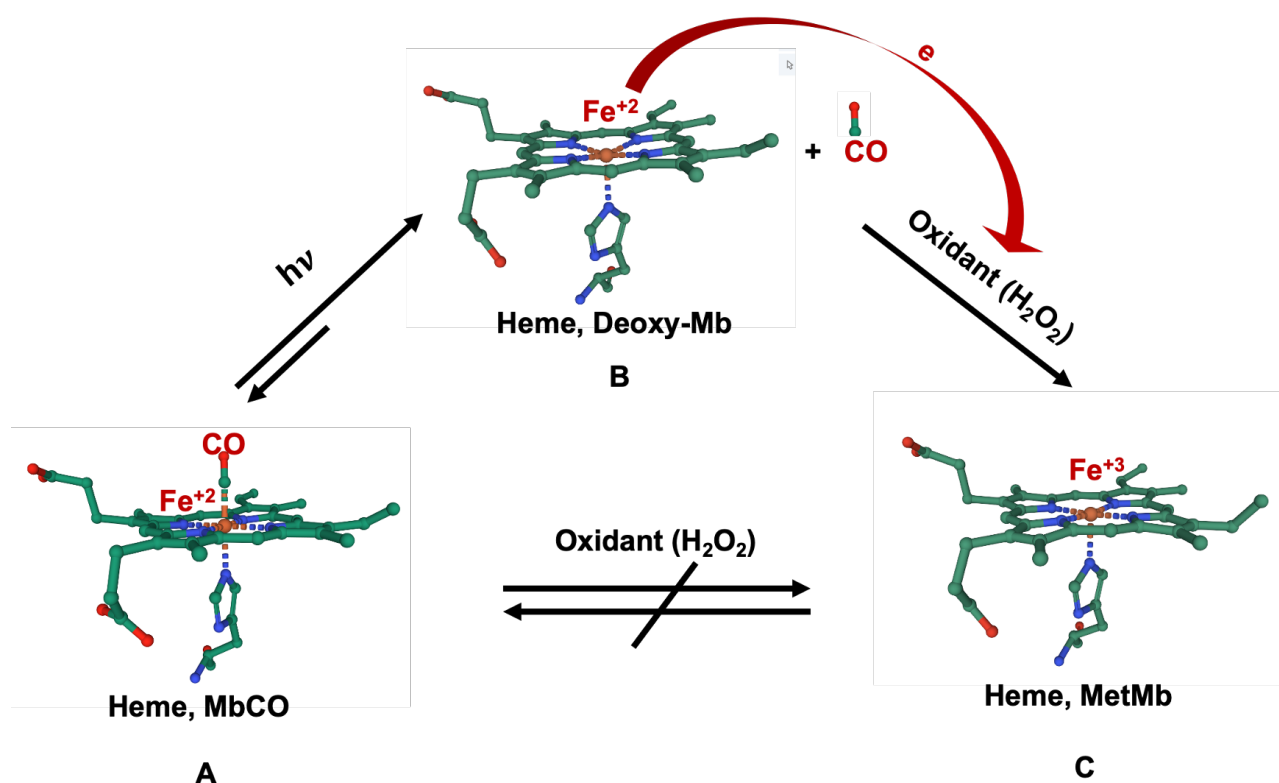


**Figure 3.11** A schematics of the experimental design to measure the quantum yield of MbCO photodissociation (A) MbCO is photodissociated to deoxy-Mb ( $A \leftrightarrow B$ ), (B) The heme in deoxy-Mb is oxidized with  $\text{H}_2\text{O}_2$  ( $B \leftrightarrow C$ ), (C) Met-Mb and MbCO do not convert to each other in presence of  $\text{H}_2\text{O}_2$  (A, C). The images of hemes have been exported from PDB (The Horse heart 1A6G, 5D5R, and 1WLA for MbCO, deoxy-Mb, and met-Mb respectively)



### 3.2.4 Control experiment

We want to be sure that in the following MbCO photodissociation experiments under oxidizing conditions, MbCO itself is not oxidized by  $\text{H}_2\text{O}_2$  (Figures 3.11 C, and 3.12) and only deoxy-Mb (the product of Mb-CO dissociation) reacts with  $\text{H}_2\text{O}_2$  and produces met-Mb (Figure 3.11 A).

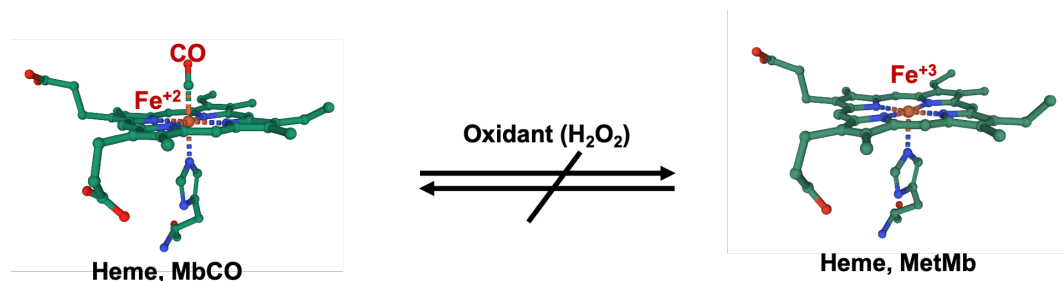


**Figure 3.12** A schematics of control experiment. MbCO does not convert to met-Mb, even in the presence of  $\text{H}_2\text{O}_2$ , and the inverse reaction doesn't occur either. The images of the heme groups have been exported from the PDB (Horse heart 1A6G, and 1WLA for MbCO, and met-Mb respectively)

As a control experiment, the absorption spectrum of MbCO in the presence of oxidant ( $\text{H}_2\text{O}_2$ ) without illumination was followed over time to check for any possible changes because of the presence of the oxidant (Figure 3.13). Before that, the excess of CO in the solution was removed by bubbling the sample with pure  $\text{N}_2$ .

As it can be seen in Figure 3.13, there is not any change in the absorption spectrum of MbCO mixed with  $\text{H}_2\text{O}_2$ , even in the presence of an excess of  $\text{H}_2\text{O}_2$  and after a long incubation time of 2 hours. It should be noted that met-Mb cannot be reduced in our oxidizing conditions. Therefore, the reverse reaction, the conversion of met-Mb to MbCO, cannot occur.

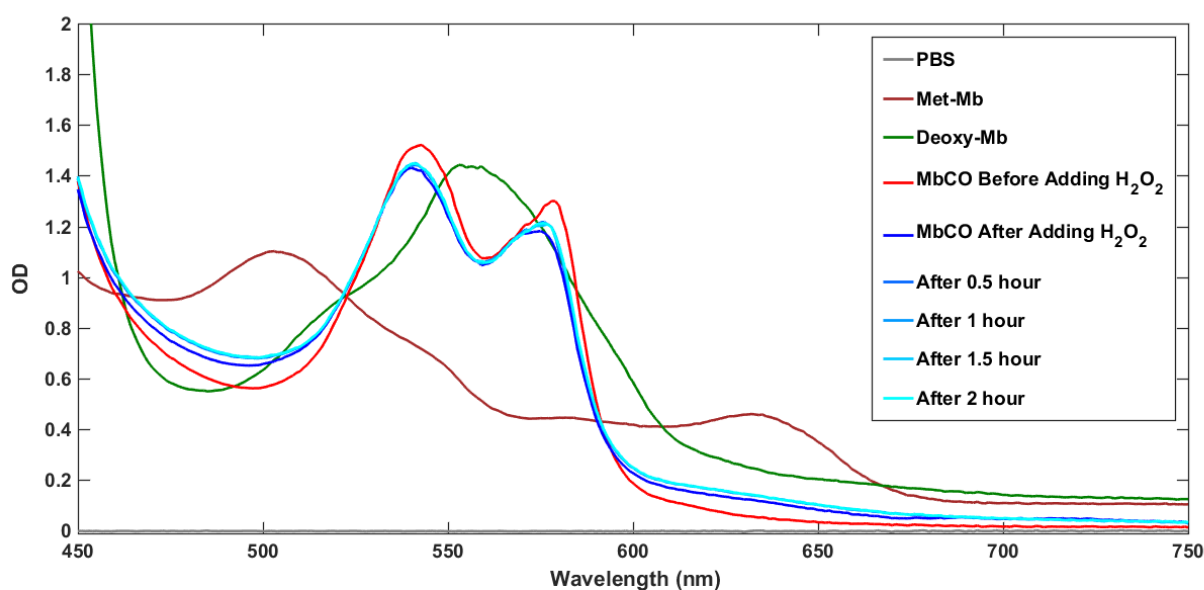


**Figure 3.13** Absorption spectra of MbCO before (red) and after adding an excess amount of oxidant ( $\text{H}_2\text{O}_2$ ) (dark blue) and followed over time (lighter blue) without illumination, in PBS,  $\text{pH}=7.2$ , at room temperature.

In our designed experiment (Figure 3.11) to calculate the quantum yield of MbCO photodissociation, it is essential that after each MbCO is dissociated with a photon and CO escapes to the solution, the deoxy-Mb is efficiently and quickly oxidized by  $\text{H}_2\text{O}_2$ , producing met-Mb with high yield, and also that the produced met-Mb should not revert back to deoxy-Mb (Figures 3.11 B, and 3.14). Therefore, by measuring the amount of met-Mb as a function of time, the quantum yield of Mb-CO bond breaking can be determined. Thus, the reaction of deoxy-Mb with  $\text{H}_2\text{O}_2$  was monitored by following the absorption spectra over time under our oxidizing conditions.

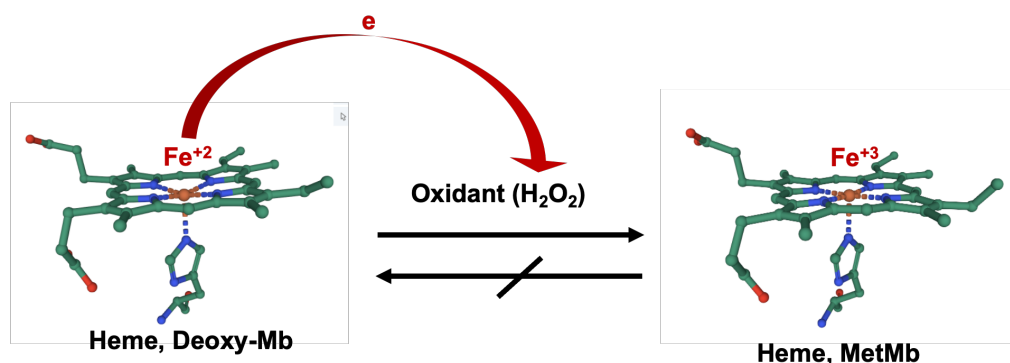


**Figure 3.14** A schematics of control experiment. Deoxy-Mb quickly converts to met-Mb in the presence of  $\text{H}_2\text{O}_2$ , whereas the reverse reaction is impossible. The images of hemes have been exported from the PDB (Horse heart 1A6G, and 1WLA for deoxy-Mb, and met-Mb respectively)

Figure 3.14 shows the schematic conversion of deoxy-Mb to met-Mb. It should be noted that some articles mention that met-Mb can convert to the intermediate named ferryl oxide in the presence of an excess (2 M) of  $\text{H}_2\text{O}_2$ .<sup>4</sup> Possible binding of oxygen from the solution to deoxy-Mb is of no concern, as it cannot displace CO. Figure 3.15 shows our measured absorption spectra of deoxy-Mb after adding an excess amount of oxidant ( $\text{H}_2\text{O}_2$ ), which yields a mixture of met-Mb and ferryl-Mb.

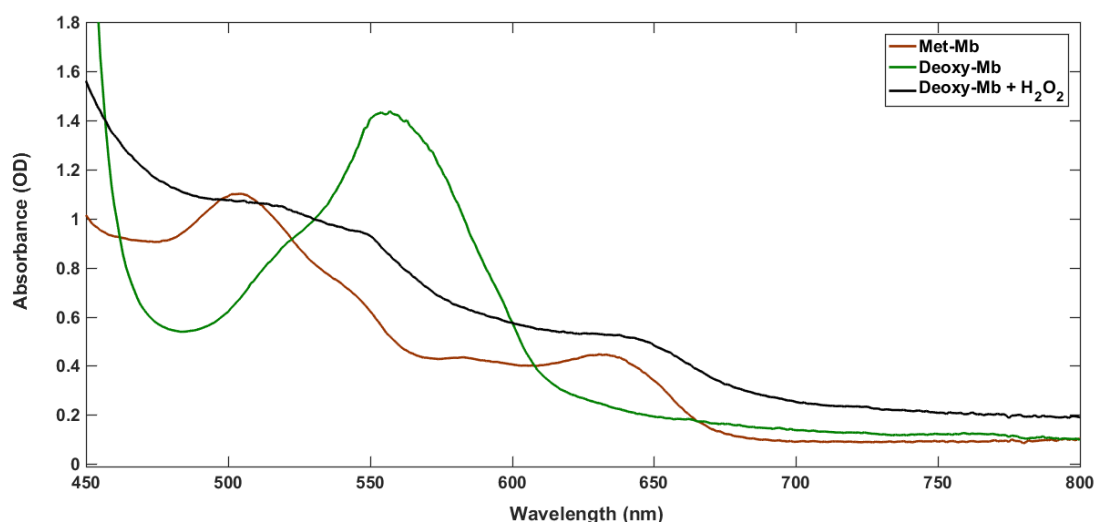


**Figure 3.15** Absorption spectra of met-Mb (brown), deoxy-Mb (green) and deoxy-Mb after adding an excess amount of oxidant ( $\text{H}_2\text{O}_2$ ) (black) in PBS, pH=7.2, at room temperature. Deoxy-Mb converts to a mixture of met-Mb and ferryl-Mb.<sup>4</sup>

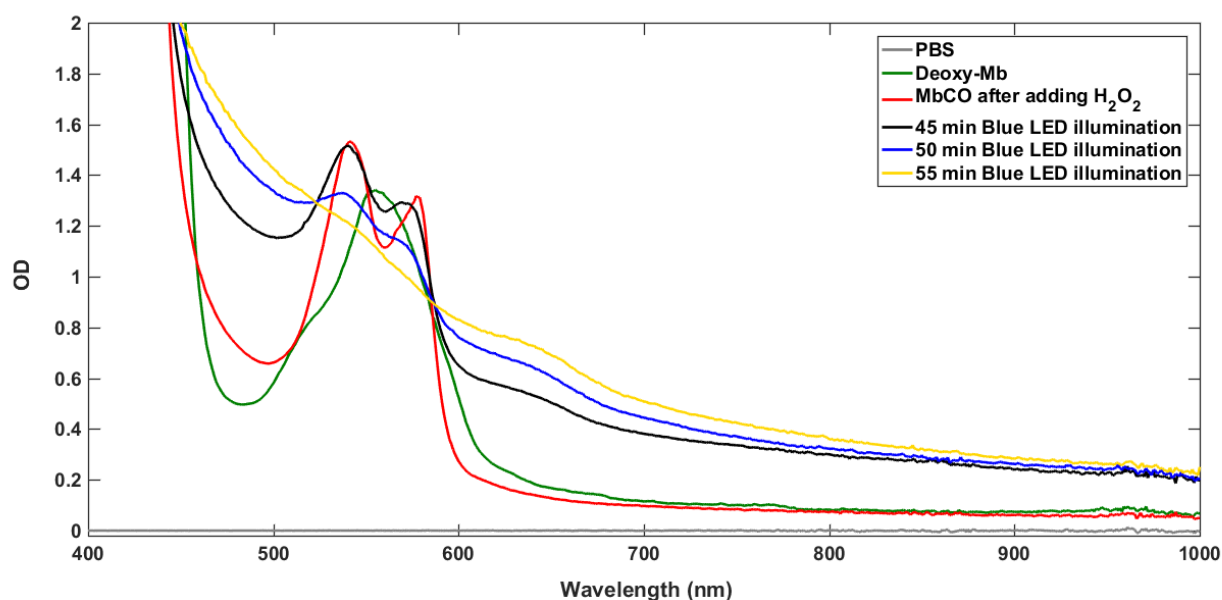


### 3.2.5 Study of the photodissociation kinetics of Mb-CO in the presence of $H_2O_2$ under blue LED illumination ( $\lambda = 450$ nm)

As the quantum yield of MbCO bond breaking by blue light is close to 1, we can use this photoreaction as a reference. Photodissociation of MbCO will lead to deoxy-Mb, which under our oxidizing conditions will immediately be converted to met-Mb, enabling us to titrate the dissociated MbCO quantitatively. To study the photodissociation kinetics of MbCO, we illuminated the protein solution in the presence of oxidant using a near infra-red LED ( $\lambda = 730$  nm) and the absorption at 540 nm (Q-band) was followed over time to measure the kinetics of the Mb-CO bond breaking. This experiment was repeated with blue LED light ( $\lambda = 450$  nm) as a reference. Therefore, later we will compare illumination by blue light ( $\lambda = 450$  nm) (reference experiment) with illumination by red light ( $\lambda = 730$  nm), both in the presence of oxidant. One requirement to measure the quantum yield of the MbCO bond breaking is the precise determination of the excitation efficiencies at the emission wavelengths of the red and blue LEDs.

The LED experiments will be compared to a control experiment with no illumination to eliminate unknown factors that may influence the results of control and LED illumination experiments, provided these influences are identical (Figures 3.13).

The reference experiment includes 12 cycles of blue-light illumination of MbCO in the presence of oxidant,  $H_2O_2$ . The duration of each cycle is 5 minutes Blue LED illumination. After each cycle, the absorption spectrum of the sample was recorded while the blue LED was turned off. Figure 3.16 shows the absorption spectrum changes of MbCO under blue LED light ( $\lambda = 450$  nm) over time.



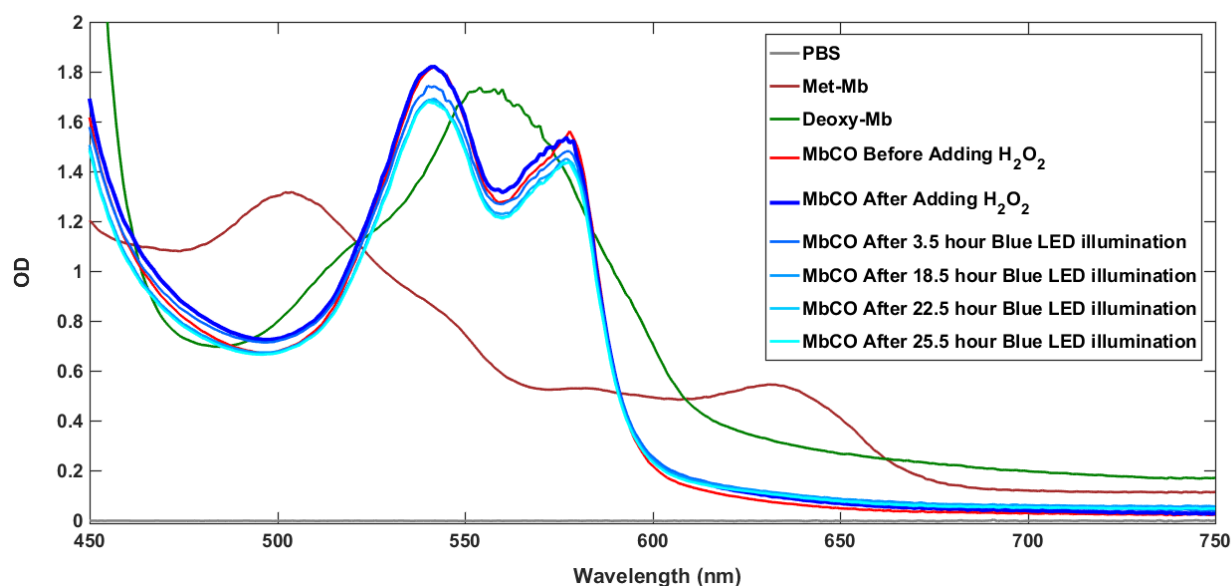
**Figure 3.16** Absorption spectra of MbCO in the presence of an excess amount of oxidant ( $H_2O_2$ ) (red) and after blue-light illumination ( $\lambda = 450$  nm) over time at room temperature. Under blue-light illumination, MbCO dissociates to form deoxy-Mb, which immediately converts to met-Mb or ferryl forms.

Figure 3.16 clearly shows the change in the absorption spectrum in the Q-bands regions of MbCO before and after illumination with blue light. As can be seen, before illumination there are two peaks at 542 nm and 579 nm which are absorption characteristic for MbCO. After around 1 hour of illumination with blue light, they completely disappear. This is consistent with the conversion of MbCO to deoxy-Mb by blue light and full conversion of deoxy-Mb to met-Mb and ferryl forms.

Moreover, the rate of MbCO breaking is very fast and, after 60 min, a full conversion of MbCO to deoxy-Mb by blue-light illumination occurred, followed by the fast oxidation of deoxy-Mb to met-Mb by  $\text{H}_2\text{O}_2$ .

### 3.2.6 Study of photodissociation kinetics of the Mb-CO in the presence of $\text{H}_2\text{O}_2$ and near infra-red LED illumination ( $\lambda = 730 \text{ nm}$ )

To study photodissociation kinetics of MbCO in the near infra-red region, we illuminated a myoglobin solution containing an excess amount of oxidant ( $\text{H}_2\text{O}_2$ ) with near infra-red LED light ( $\lambda = 730 \text{ nm}$ ). The absorption at 540 nm (Q-band) was followed over time to measure the kinetics of the Mb-CO bond breaking. As can be seen in Figure 3.17, even over a long time (25.5 hours) no change in the absorption spectrum of MbCO was observed, which clearly shows that near infra-red LED light ( $\lambda = 730 \text{ nm}$ ) is much less efficient than blue light in breaking the MbCO bond. Figure 3.18 shows the change of the OD of MbCO solution at a wavelength 540 nm over time.



**Figure 3.17** The absorption spectra of MbCO before (red) and after adding an excess amount of oxidant ( $\text{H}_2\text{O}_2$ ) (dark blue) and following over time (lighter blue) under near infra-red LED illumination ( $\lambda = 730 \text{ nm}$ ) in PBS,  $\text{pH}=7.2$ , at room temperature.

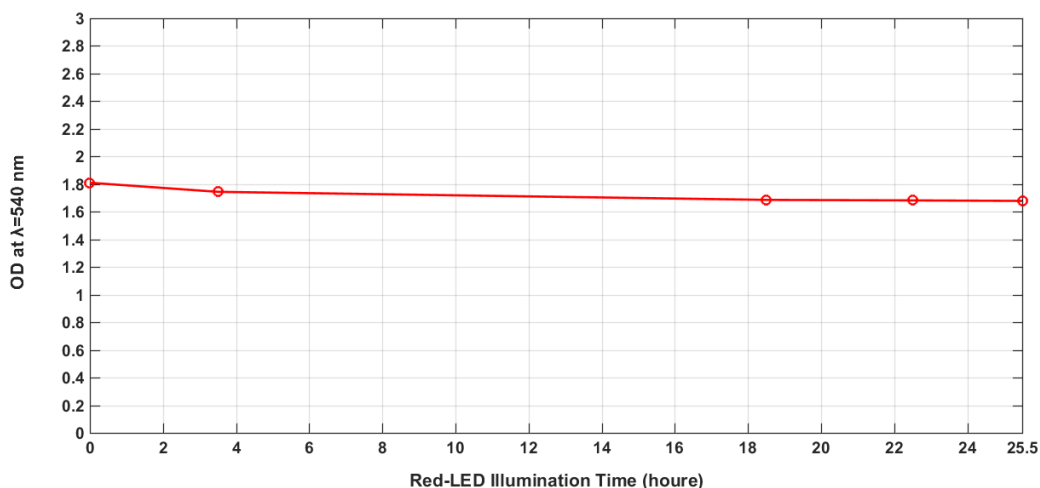


**Figure 3.18** The OD of a MbCO solution at wavelength 540 nm was measured after 3.5, 18.5, 22.5, and 25.5 hours) under near infra-red LED illumination ( $\lambda = 730$  nm) in PBS, pH=7.2, at room temperature.

#### 3.2.7 Estimation of photon rate

Another challenge is that MbCO has a very low absorbance in the near infra-red spectral region so the excitation efficiency is very low. To solve this problem, a highly efficient illumination is needed. Moreover, it is difficult to determine the excitation efficiency by the LEDs precisely. In addition, the possibility of CO rebinding may complicate the kinetics of rebinding.

To estimate the quantum yield, it is first necessary to determine the relative photon absorption rate of red versus blue photons. Here, the ( $t = 0$ ) photodissociation quantum yield ( $\eta_0$ ) of MbCO with the near infra-red LED ( $\lambda_{\max} = 730$  nm,  $\eta_0(R)$ ) is estimated compared to the photodissociation quantum yield of MbCO with blue LED ( $\lambda_{\max} = 450$  nm) which we assume is unity, ( $\eta_0(B) = 1$ ) taken as a reference.

The ratio of the number of Mb-CO bonds broken with near infra-red LED compared to blue LED can be calculated by the estimation of the probability of MbCO bond breaking (the efficiency of MbCO photodissociation), the probability of photon absorption photon and the number of absorbed photons by the MbCO molecules (eq 3.1).

$$\frac{N_{\text{broken bonds}}_{\text{-RED}}}{N_{\text{broken bonds}}_{\text{-BLUE}}} = \left( \frac{\eta_0(R)}{\eta_0(B)} \right) \cdot \left( \frac{N_{\text{Incident photon per second}}_{\text{-RED}}}{N_{\text{Incident photon per second}}_{\text{-BLUE}}} \right) \cdot \left( \frac{\text{Time Incident photon}_{\text{-RED}}}{\text{Time Incident photon}_{\text{-BLUE}}} \right) \cdot \left( \frac{P_{\text{Incident photon}}_{\text{-RED}}}{P_{\text{Incident photon}}_{\text{-BLUE}}} \right) \quad 3.1$$

The number of incident photons per second emitted from the near infra-red and blue LEDs are obtained by measuring the power of illumination light passing through the filters into the MbCO solution inside the cuvette, and by taking into account the energy of blue and red photons which have a different energy per photon. The power of blue

LED and near infra-red LED were measured to be 0.5, and 2 mW, respectively, with a photon energy ratio of 1.62. The ratio of the number of incident photons per second emitted from red and blue LEDs was calculated to be 6.48. Finally, the ratio of the numbers of incident photons over the whole duration of the experiments (25.5 hours for the near infra-red LED illumination and around 1 hour for the blue LED illumination) is 165.2.

The number of absorbed photons depends on three factors including the brightness of the LEDs, the transmission of excitation light through the filters between the LEDs and the samples, as well as the absorptivity of the MbCO molecules at the respective wavelengths. It should be noted that based ref. 3, the ratio of absorptivity of MbCO at 450 nm, and 730 nm is 82 ( $\frac{\epsilon_{730 \text{ nm}}}{\epsilon_{450 \text{ nm}}} = 82$ ). The number of absorbed photons was obtained by multiplying the LED intensity, the transmission of the filter used (see Figures 3.19, 3.20) and the absorbance of MbCO at each wavelength (Figure 3.21). Based on our calculation, the ratio of the numbers of absorbed photons for red to blue LED illumination is 0.0978.

The illumination efficiency of red to blue is calculated as 16.1 according to eq 3.1.

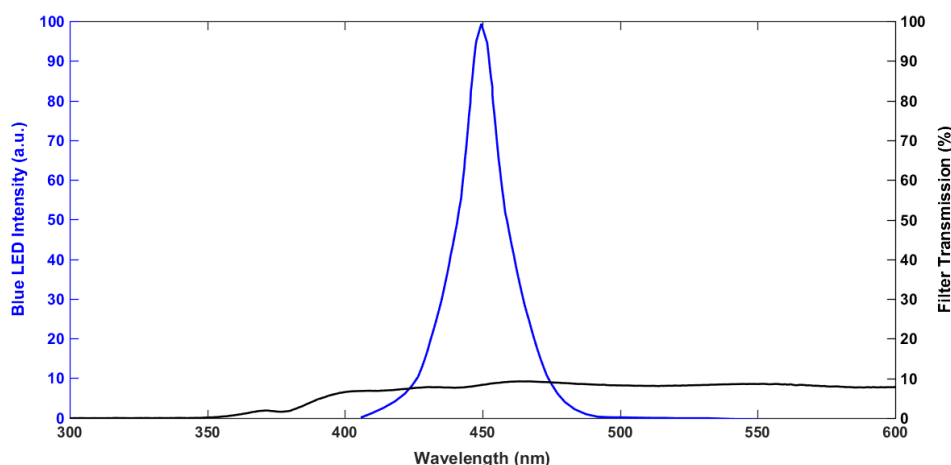


**Figure 3.19** Blue LED illumination intensity profile with maximum intensity at wavelength 450 nm (blue), and transmission spectrum of Neutral Density filter (black)

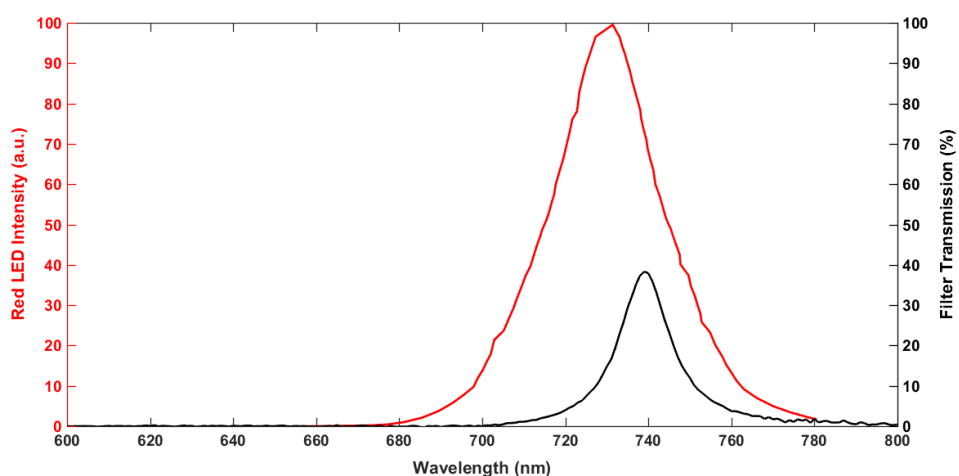


**Figure 3.20** Near infra-red LED illumination intensity profile with maximum intensity at wavelength 730 nm (red), and transmission spectrum of the filter (black).

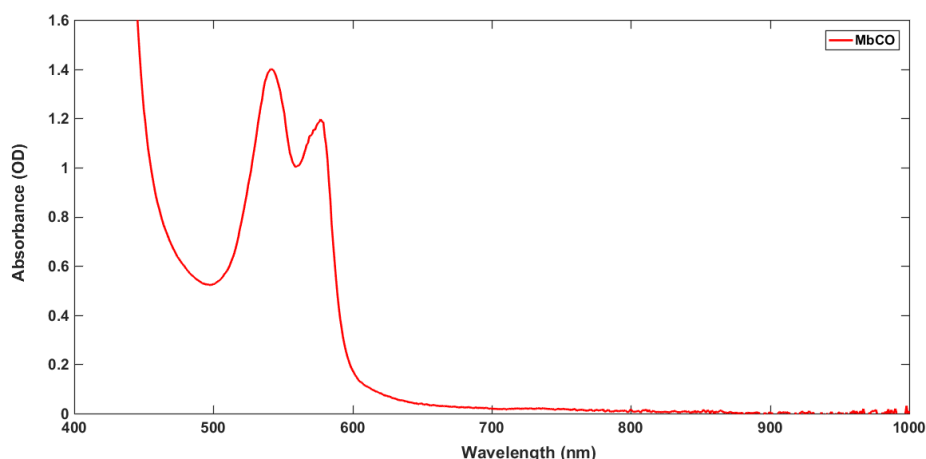


**Figure 3.21** Absorption Spectra of MbCO sample solution

#### 3.2.8 Comparison and calculation of quantum yield efficiency for photodissociation of unlabeled Mb-CO by near infra-red and blue LEDs

The ratio of illumination efficiencies of red to blue was obtained as 16.1. Observing the same effect under both blue and red illumination in our experiment, would indicate a quantum yield for the red illumination of around 6%. Since the illumination of MbCO experiments showed no significant effect for red, the quantum yield in the red has to be in fact be much less than unity.

$$\frac{N_{\text{breaking bond}_{\text{RED}}}}{N_{\text{breaking bond}_{\text{BLUE}}}} = \left( \frac{\eta_0(R)}{\eta_0(B)} \right) \cdot 16.1 \quad 3.2$$

$$\eta_0(R) < 0.06 \eta_0(B)$$

However, the quantum yield of blue LED is 1 ( $\eta_0(B) = 1$ ), so as upper estimation the quantum yield of photodissociation of MbCO with near infra-red LED should be significantly below 1;  $\eta_0(R) < 0.06$ . It should be noted that we should also consider an error for the value of absorbability of MbCO at the wavelength of 730 nm, because the OD at this wavelength is close to the noise of spectrometer at the used concentration in this experiment.

Finally, we could not precisely determine the dissociation quantum yield of MbCO under far red light because of the complicated mixture of products. However, we can have an upper bound quantum yield, it has to be less than 6%.

### 3.3 Conclusion and outlook

Based on the experiment results from the MbCO illumination by the near infra-red LED in the presence of  $\text{H}_2\text{O}_2$  and comparing to the blue LED illumination results as the reference experiment, we could estimate an upper bound quantum yield of MbCO photodissociation, and it has to be less than 6%.

For an improved estimate of the dissociation yield and to test the possibility to monitor CO binding with red-excited fluorescence, we propose the following experiment, using

MbCO labeled with the red-emitting dye ATTO740. Excitation of this dye provides a much more efficient excitation mechanism of Mb through FRET from the ATTO740 donor. By monitoring the deoxy-Mb and met-Mb produced by dye illumination (still under oxidative conditions to prevent CO rebinding), we will determine the number of dye excitations required to photodissociate MbCO with red light. At the same time, the number of absorbed photons by ATTO740 before dissociation will give us the number of fluorescence photons which we can expect from each labeled MbCO before it gets split by a red excitation. If this number is larger than about 100, the inverse detection yield of our microscope, it will be possible to follow the binding state of Mb in real time at the single-molecule level. Another possible way to improve this experiment to reach better estimation of quantum yield is to use the sample cuvette with a path length of 10 mm for the monitoring beam (as before) and a path length of less than 1 mm (in contrast to before that was 10 mm) for the photolyzing light, which helps to illuminate more efficiently the MbCO molecules in the shorter path as the absorbability of MbCO at 730 nm is small.

## References

- (1) Pradhan, B.; Engelhard, C.; Mulken, S. V.; Miao, X.; Canters, G. W.; Orrit, M. Single Electron Transfer Events and Dynamical Heterogeneity in the Small Protein Azurin from *Pseudomonas Aeruginosa*. *Chem. Sci.* **2020**, *11* (3), 763–771.
- (2) Tabares, L. C.; Gupta, A.; Aartsma, T. J.; Canters, G. W. Tracking Electrons in Biological Macromolecules: From Ensemble to Single Molecule. *Molecules* **2014**, *19* (8), 11660–11678.
- (3) Bowen, W. J. The Absorption Spectra and Extinction Coefficients of Myoglobin. *J. Biol. Chem.* **1949**, *179* (1), 235–245.
- (4) Yusa, K.; Shikama, K. Oxidation of Oxymyoglobin to Metmyoglobin with Hydrogen Peroxide: Involvement of Ferryl Intermediate. *Biochemistry* **1987**, *26* (21), 6684–6688.



# 4

## **FRET study of CO binding to fluorescently labeled myoglobin**

*Based on the estimated quantum yield of bond breaking in the chapter 3, we believe that the MbCO complex should be stable enough to monitor FRET from the near infra-red donor to the heme group, with enough donor fluorescence photons being emitted before photodissociation of the MbCO occurs. The FRET measurement of the donor fluorescence intensity of fluorescence lifetime.*

*In this chapter, our aim is to prepare a properly labeled MbCO with a dye that can be excited and emits in the near infra-red, and to study the energy transfer from the dye to Mb and to MbCO when illuminating with  $\lambda > 700$  nm. Would it be possible to distinguish between the two Mb states; MbCO and deoxy-Mb, and to use this fluorescence signal to study the kinetics of CO rebinding?*



### 4.1 Introduction

Fluorescence spectroscopy is a reliable method for detecting the activity of proteins.<sup>1,2</sup> The single-molecule FRET (smFRET) approach has been widely used to determine kinetic rates of proteins.<sup>3-4</sup> Proteins can be specifically labeled using one or more dyes for smFRET measurements. For example, as I discussed in chapter 3, azurin is a redox protein which has a redox cofactor copper atom to carry out specific redox reactions. The absorption spectrum of azurin changes when the redox state of the prosthetic group changes ( $\text{Cu}^+ \leftrightarrow \text{Cu}^{2+}$ ). Therefore, the attachment of a fluorescent molecule to the protein surface makes it possible to monitor the fluorescence emission of single-dye-labeled azurin molecules by means of Förster Resonance Energy Transfer (FRET) spectroscopy.<sup>5</sup>

Inspired by the FRET-based probing of the redox state of azurin, we explore whether the kinetics ligand to binding to myoglobin (Mb) could be measured using FRET. In the case of Mb a change of the absorption spectrum is observed when CO binds to or dissociates from the heme. Thus, by labeling Mb with the proper dye, we can monitor the fluorescence emission of the dye-labeled-Mb in different states by mean of Förster Resonance Energy Transfer (FRET). In this way, we hope to determine the rebinding kinetics of CO at the single-molecule level.

In Chapter 2, we showed that the Mb spectrum consists of three main parts: the Soret band (300-500 nm), the Q-band(s) (500-700 nm) and the NIR bands (700-1000 nm). When the Mb-CO bond is illuminated in the area of the Soret band or the Q-band, the quantum yield of breaking the Mb-CO bond is unity. Therefore, monitoring the absorption spectrum of a single molecule in those spectral ranges would unavoidably lead to CO dissociation and could not be used for monitoring CO binding. What about the NIR spectral range? The interesting question is whether illumination with near infra-red light with a wavelength beyond 700 nm breaks the MbCO bond or not and if yes, with which photodissociation quantum yield?. And answer this question whether FRET to MbCO will dissociate the bond when measured in the near infra-red region. In chapter 3, we described experiments to determine the quantum yield of photodissociation under near infra-red illumination in order to determine if that region can be used for FRET. We proposed in chapter 3 an approach using a weak band beyond 700 nm (band III at 760 nm) in the deoxy-Mb absorption spectrum to quench the fluorescence of a dye donor fluorescing in the near infra-red range. As band III is absent from the spectrum of MbCO, breakage of the CO bond due to resonant energy transfer from the excited dye to the heme excited states seemed unlikely, but this has to be checked. Although the absorption coefficient of Band (III) is very small, however, as the Forster radius;  $R_0$  depends on the sixth root (eq. 4.1), make it possible to use this system for FRET study by control of the distance between the donor and acceptor. Our results of chapter 3 show that illumination of MbCO with near infra-red light (700-800 nm) does not break the Mb-CO bond efficiently. Based on the estimated quantum yield of bond breaking, we believe that the MbCO complex should be stable enough to monitor FRET from the near infra-red donor to the heme, with enough donor fluorescence photons emitted before dissociating MbCO during the FRET measurement. Although lifetime measurements are more sensitive than the fluorescence intensity, our FRET study is based on the both fluorescent intensity and lifetime measurement.

In this chapter, our aim is to prepare a properly labeled MbCO with a dye that can be excited and which emits in the near infra-red, and to study the energy transfer from the dye to Mb and to MbCO when illuminating with  $\lambda > 700$  nm. Would it be possible

to distinguish between two Mb states; MbCO and deoxy-Mb, and to use this fluorescence signal to study the kinetics of CO rebinding?

It should be noted that this chapter focuses on the FRET study of labeled MbCO at room temperature. However, to study the kinetic rebinding of CO to myoglobin at low temperature, in future, it is essential to measure absorption spectra of MbCO and deoxy-Mb in near infra-red region at low temperature (120-140 K) because the absorption spectra in particular absorption spectrum of deoxy-Mb will change when the temperature decreased.<sup>6</sup>

#### 4.1.1 Can we measure the FRET efficiency of different states of labeled Mb (deoxy-Mb and MbCO)?

In FRET, energy transfer occurs from a donor fluorophore to an acceptor molecule, by which the fluorescence emission of the donor is quenched and the fluorescence of the acceptor is sensitized. In some metallo-proteins, the donor can be a fluorescent dye attached to a specific site of the protein, whereas the acceptor can be a center inside the protein such as the redox copper center in azurin or the heme in Mb. As the heme in Mb displays several electronic absorption bands between 350 and 1000 nm, it can act as an acceptor for a fluorescent dye attached to Mb. The FRET efficiency is sensitive to the position of the dye with respect to the heme. The smaller the distance to the heme, the more efficient the energy transfer. Moreover, the larger the spectral overlap between the absorption spectrum of the Mb and the emission spectrum of the donor dye, the stronger the energy transfer from dye to heme. The FRET efficiency can be quantified by fluorescence intensity or, more reliably, by the fluorescence lifetime of the donor dye.

The two relevant states of Mb, deoxy-Mb and MbCO, have very different absorption spectra in the near infra-red spectral range (700-1000 nm) (Figure 4.1). Therefore, the FRET efficiency for dye labeled-deoxy-Mb must be different from that of the dye-labeled-MbCO. However, The FRET efficiency difference between deoxy-Mb and MbCO has to be large enough to be readily observable on the fluorescence intensity and/or lifetime.

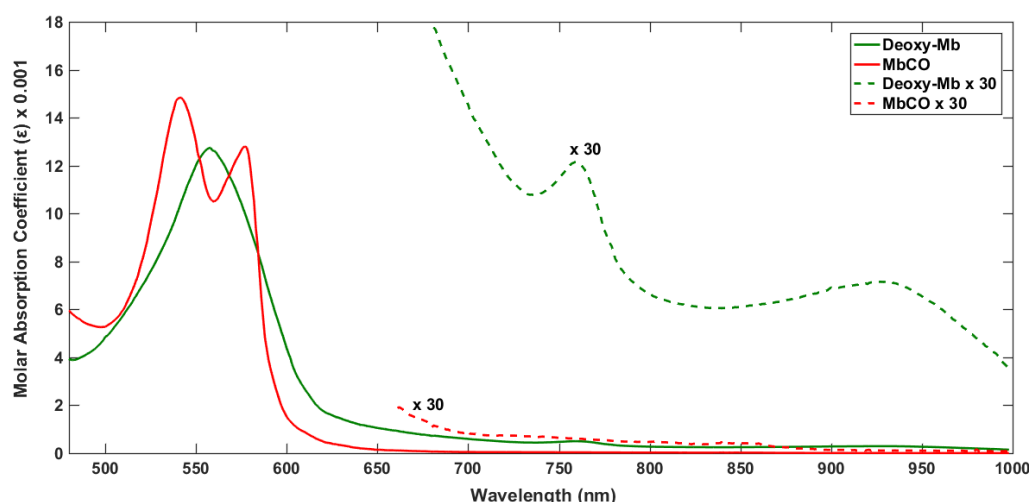


**Figure 4.1** Absorption spectrum of the Q-bands (500-700 nm) and NIR bands (700-1000 nm) for two Mb states: deoxy-Mb (green), and MbCO (red) from horse heart Mb at room temperature, in Sørensen's phosphate buffer (0.05 mM) with pH 6.8-8. The stippled lines represent the 30x enlarged spectra.<sup>7</sup>

### 4.1.2 Investigating rebinding kinetics of CO to Mb with FRET

FRET strategies are often used to investigate molecular interactions when the distance between partners is 1-10 nm, for example between a donor (dye label on a protein) and an acceptor (heme in Mb).

The FRET efficiency is related to fluorescence lifetime, and additional information can be extracted by analyzing the fluorescence intensity and lifetime together. Time-dependent FRET measurements have been developed to characterize the reaction kinetics of enzymes<sup>8,9</sup> and ligand-receptor interactions.<sup>10</sup> Fluorescence lifetime correlation analyses have also been used to distinguish different species in a mixture<sup>11</sup> or to probe fast molecular processes on the microsecond to millisecond time scale.<sup>12</sup> Importantly, different species can be more reliably identified by analyzing the lifetime data than by analyzing intensity data because intensity will vary depending on the instrumentation and experimental setup whereas lifetime does not.

Utilizing fluorescence lifetime information appears as an attractive method to study the re-binding of small molecules such as CO to the heme. However, if the binding-unbinding process is too fast, individual states will not be well separated in a lifetime trajectory, and it will not be easy to obtain the lifetime information. In this chapter, our aim is to optimize the FRET efficiency in a labeled Mb by a proper choice of dye and of the labeling position. Then, we will have to show that the different Mb states can be identified reliably on the basis of their fluorescence lifetime and/or fluorescence intensity.

In other words, our aim is to prove that it is possible to distinguish FRET rates in Mb and MbCO, and to study the kinetics of rebinding of CO to Mb by means of fluorescence lifetime measurements, and it may also be possible by fluorescence intensity measurements.

## 4.2. Results

### 4.2.1 Labeling position and fluorescent dye selection

Selection of the proper dye is crucial. A range of available and photostable dyes with their fluorescent properties including wavelength of maximum emission, lifetime, quantum yield and calculated  $R_0$  related to deoxy-Mb and MbCO are given in Table 4.1.  $R_0$ 's have been calculated based on Eq (1.1) in Chapter 1 in which the donor is the fluorescent dye and the acceptor is the heme center of deoxy-Mb and MbCO.  $R_0$  (in Å) is given by:<sup>13</sup>

$$R_0 = 0.2108 \left( \frac{\kappa^2 \phi_D}{n^4} \int \bar{F}_D(\lambda) \epsilon_A(\lambda) \lambda^4 d\lambda \right)^{\frac{1}{6}} \quad 4.1$$

where  $\phi_D$  is the fluorescence quantum yield of the donor in the absence of the acceptor,  $\kappa^2$  is the dipole orientation factor and can vary between 0 and 4 (here we assume an isotropic angular distribution of the dye, thus the average orientational factor is  $\kappa^2 = \frac{2}{3}$ ),  $n$  is the refractive index of the medium (here we assume a water medium thus the refractive index is  $n = 1.33$  and more appropriate is to use 1.4; a mixture between buffer ( $n = 1.33$ ) and protein  $n = 1.5$ ),  $\epsilon_A(\lambda)$  is the acceptor molar extinction coefficient ( $M^{-1}cm^{-1}$ ). In this work, the acceptors are deoxy-Mb and MbCO

and their molar extinction coefficient values were extracted from ref. [7], and  $\bar{F}_D$  is the donor emission spectrum normalized to an area of 1 ( $\int_0^\infty F_D(\lambda) d\lambda = 1$ ). In this work,  $\bar{F}_D$  is calculated based on the donor emission spectra of the fluorescent dyes (Table 4.1) obtained from ref. <sup>14,15</sup> The fluorescence emission spectra corresponding to these dyes are shown in Figure 4.2.

**Table 4.1** Photostable dyes with their fluorescent properties including wavelength of maximum emission ( $\lambda_{em}$ ), quantum yield ( $\phi_D$ ), lifetime ( $\tau$ ),<sup>14,15</sup> and calculated  $R_0$  for deoxy-Mb and MbCO.

Dye <sup>a</sup>	$\lambda_{em}$	$\phi_D$	$\tau$	$R_0^b$	$R_0^b$
				MbCO	deoxy-Mb
ATTO Rho14	646 nm	80%	3.7 ns	2.72 nm	3.73 nm
ATTO 633	651 nm	64%	3.4 ns	2.53 nm	3.56 nm
ATTO 647	667 nm	20%	2.4 ns	1.98 nm	2.89 nm
<b>ATTO 643</b>	<b>664 nm</b>	<b>65%</b>	<b>3.5 ns</b>	<b>2.46 nm</b>	<b>3.54 nm</b>
ATTO 655	680 nm	30%	1.8 ns	2.08 nm	3.07 nm
ATTO Oxa12	681 nm	30%	1.8 ns	2.09 nm	3.07 nm
ATTO 680	698 nm	30%	1.7 ns	2.02 nm	3.04 nm
ATTO 700	716 nm	25%	1.6 ns	1.95 nm	2.93 nm
ATTO 725	751 nm	10%	0.5 ns	1.66 nm	2.53 nm
<b>ATTO 740</b>	<b>763 nm</b>	<b>10%</b>	<b>0.6 ns</b>	<b>1.66 nm</b>	<b>2.54 nm</b>
<b>Cy7</b>	<b>773 nm</b>	<b>30%</b>	<b>0.5 ns</b>	<b>2.00 nm</b>	<b>2.99 nm</b>

<sup>a</sup> All fluorescent properties of the dyes reported based on the manufacturer's data <sup>14,15</sup>

<sup>b</sup> The  $R_0$  values for the deoxy-Mb and MbCO were calculated based on equation 4.1, the room temperature spectra of Mb, and the assumptions mentioned in section 4.2.1.

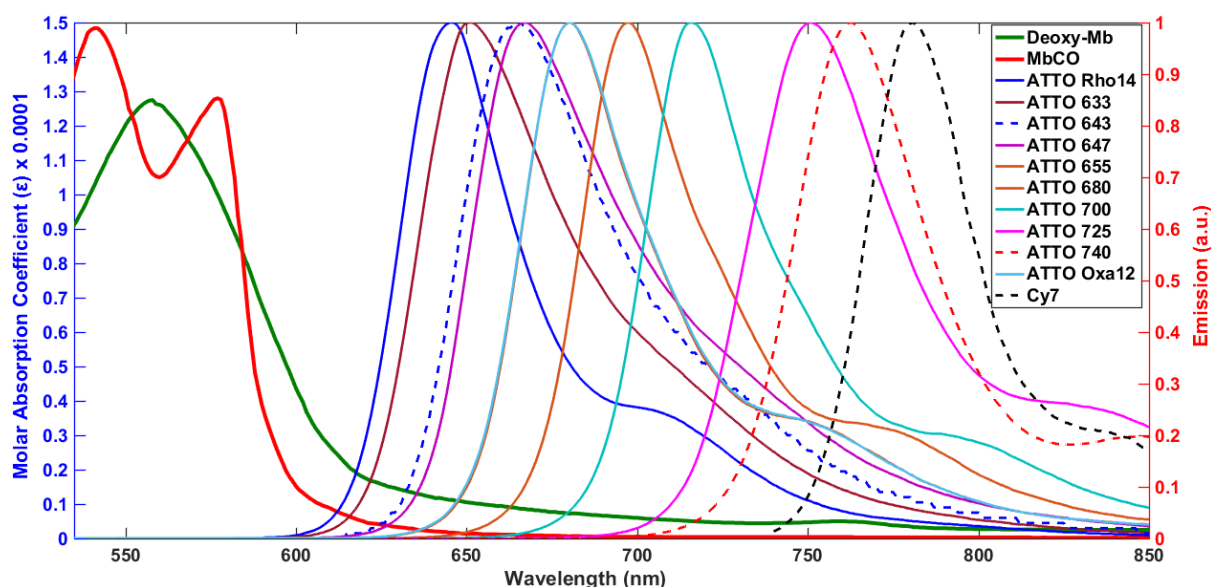


**Figure 4.2** The absorption spectra of deoxy-Mb (solid green) and MbCO (solid red) (left axis), <sup>7</sup> and fluorescence emission spectra of various dyes listed in table 1 as donors in phosphate buffer, pH=7 (right axis). <sup>14,15</sup> ATTO 643 (dashed blue), Cy7 (dashed black), and ATTO 740 (dashed red) are the fluorescent dyes selected as donors for our FRET experiments.

While there are many fluorophores available for protein labeling, few are suitable for estimating the quantum yield of MbCO bond breaking by NIR excitation.

We have selected ATTO 643 dye as the donor in this FRET study of Mb. Atto643 dye has a maximum absorption at 643 nm (Figure 4.2) and it emits with a maximum intensity at 664 nm with a quantum yield of 65% (Table 4.1). It is a standard dye; it is easily available and it is a safe dye with neutral charge when attached to the protein. It might minimize specific dye-protein interaction. It has also a long fluorescence lifetime (compare to NIR dyes).

To study the quantum efficiency of breaking the Mb-CO bond with light in the NIR area, a dye is needed that absorbs and emits in this region of the spectrum. For this purpose, we have selected Cy7 and ATTO 740 as photostable dyes which are excited at the wavelengths of 750 nm and 743 nm respectively, and which are far enough from the Q-bands of Mb-CO (500-700 nm) that their fluorescence cannot excite the Q-bands. Therefore, when attached to the protein, these dyes cannot excite the  $\pi$  electrons of the heme, but they only excite transitions of the iron itself. The wavelengths of maximum emission for Cy7 and ATTO 740 are 773 nm and 763 nm respectively, in a region where the absorbances of deoxy-Mb and MbCO are very different.

The main parameter that influences the FRET efficiency is the distance between donor and acceptor (see Chapter 1). Different positions of the dye on the protein provide different distances between donor and acceptor. Apart from the N-terminus, proper labeling positions can be achieved by site-directed mutagenesis (SDM).

Among the 20 amino acids, cysteine is uniquely reactive and engineered cysteine residues are common targets for specific labeling of proteins. The thiol group of cysteine reacts efficiently with the maleimide functional group of a fluorescent dye via the Munich reaction. Mb has no cysteines but cysteines can be engineered in Mb by SDM.

In this study, we used the Mb variant S3C from sperm whale (*Physeter macrocephalus*), in which serine 3 has been replaced by cysteine. The plasmid for this mutant was kindly provided by Prof. G. Ulrich Nienhaus (Karlsruhe Institute of Technology). The mutant protein was expressed in *Escherichia coli*.

Although labeling at a position closer to the heme provides higher FRET efficiency, the local steric and electrostatic characteristics around an engineered cysteine and its accessibility are also important. Moreover, keeping the labeling position away from the heme avoids disturbing the protein reaction center. The mutation at serine 3 (Figure 4.3) satisfies these considerations and provides a distance of approximately 27.4 Å from the heme center.

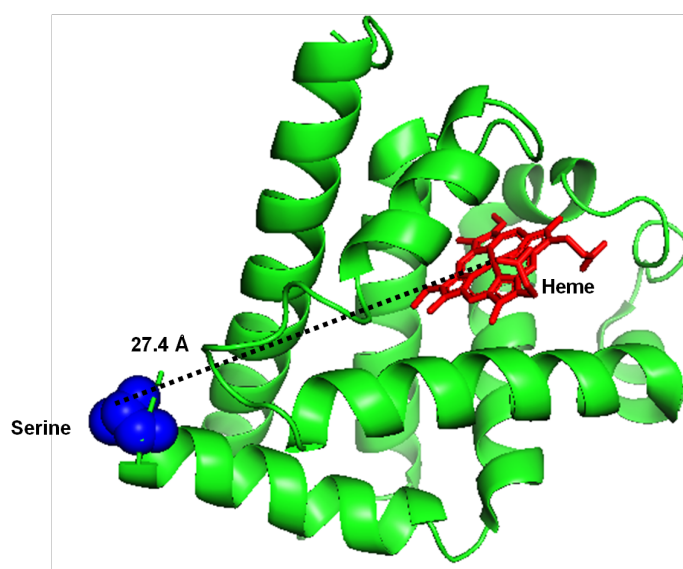


**Figure 4.3** Scheme of native sperm whale met-Mb from the Protein Data Bank (PDB: 1VXA5) indicating the heme (red), and amino acid serine 3 (site of mutation for labeling) is shown as spheres (blue). Estimation of the distance between dye and heme based on PyMOL<sup>16</sup> distance calculations. The distance between serine 3 and the center of the heme was calculated to be 27.4 Å.

An alternative, non-mutagenic labelling method is targeting the N-terminus of Mb. This allows for more free space of the dye and diminishes the electrostatic interaction with the protein. The general systematic strategy in this case is to react the free amine of the amino acid in the protein with the reactive functional group (carboxylic or N-hydroxy succinimide (NHS)) of the modified dye. By controlling pH, and the concentrations of dye and protein, we could achieve specific N-terminal labeling with high efficiency. This labeling strategy provides an easy way to install a label on the N-terminal glycine 1 in commercially available horse heart Mb. Figure 4.4 shows horse heart met-Mb which is slightly different from sperm whale met-Mb particularly in the N-terminus. The distance between the N-terminus and the heme in horse heart met-Mb is slightly shorter (24.2 Å, Figure 4.4) than between heme and serine 3 (27.4 Å). Labeling with cysteine, however, is site specific and clean.

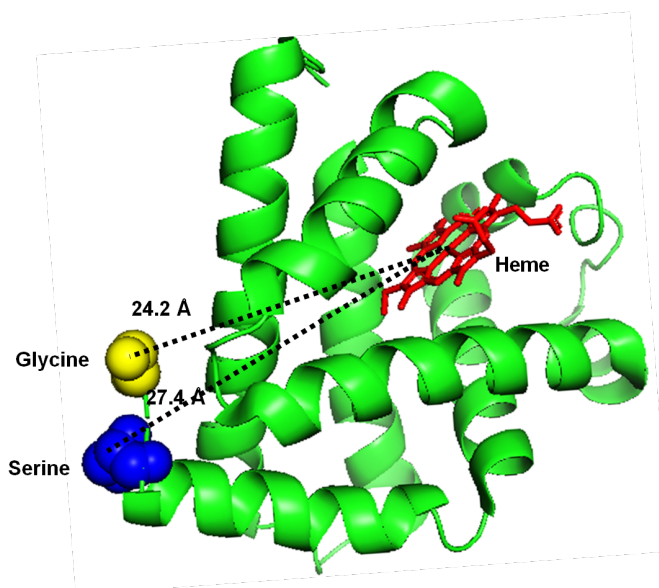


**Figure 4.4** Scheme of horse heart met-Mb from the Protein Data Bank (PDB: 1WLA) indicating the heme (red), and the N-terminal glycine 1 (site of labeling) is shown as spheres (yellow). Estimation of the distance between dye and heme based on PyMOL<sup>16</sup> distance calculations. The distance was calculated based on the distance from glycine 1 to the center of heme (24.2 Å) and compared to the distance of the heme center to the serine 3 (blue) (27.4 Å).

### 4.2.2 Preparation of labeled Mb variants

Met-Mb was labeled with the selected dyes of the previous section (ATTO 643, Cy7, and ATTO 740). Labeling of met-Mb was performed using two approaches specifically at position cysteine 3 (mutagenesis serine 3) and by N-terminal labeling. Then, as discussed in Chapter 3 (section 3.2.1), labeled met-Mb was converted to dye-labeled deoxy-Mb and to MbCO.

### 4.2.3 Materials and equipment

All chemicals were commercial products with the best quality available and, unless indicated otherwise, they were used without further purification. All solvents were purchased from Sigma-Aldrich with high purity and directly used for the experiments except DMF, which was dehydrated with Molecular Sieves (Sigma-Aldrich) before use. *Physeter macrocephalus* (sperm whale) Mb variant S3C was expressed in *Escherichia coli* and purified. The plasmid for this mutant was kindly provided by Prof. G. Ulrich Nienhaus (Karlsruhe Institute of Technology). Horse heart Mb was purchased from Sigma-Aldrich with a molecular weight of 17.7 kD.

UV-Vis absorption spectra were obtained using a droplet spectrophotometer with a light path of 1 mm and a UV-Vis spectrophotometer (Cary 50, Variant Inc., Agilent Technology, USA) with a light path of 10 mm.

### 4.2.4 Labeling and characterization of met-Mb

Labeling was performed as recommended by the research group of Prof. Don C. Lamb at the Ludwig-Maximilians-Universität, München (LUM). Mutated sperm whale met-Mb



variant S3C was labeled using commercially available ATTO 643 maleimide (ATTO-TEC GmbH, Siegen, Germany) and Cy7 maleimide, which reacts with a high yield to the thiol group of cysteine. Labeling was performed in two steps: First, unreactive disulfide bonds of mutated Mb were reduced with a ten-fold molar excess per cysteine of DTT (1,4-Dithiothreitol, Sigma-Aldrich) in potassium phosphate buffer (100 mM) at pH 7.2. To increase the efficiency of reduction, in addition, a 5-fold molar excess of TCEP (Tris(2-carboxyethyl)phosphine) per cysteine was added to the protein solution, and then the solution was flushed with Argon gas (Ar) in a desiccator. The mixture was kept for 20–30 minutes at room temperature. Removal of DTT before dye conjugation was done by four runs in a Vivaspin centrifugal concentrator (Sartorius VS0111, MWCO 10000, 500 uL) for 10 minutes with an acceleration of 10,000 g at 10 °C. Secondly, the mutated met-Mb in potassium phosphate buffer (100 mM) was allowed to react with a 3–3.5 molar excess of label dissolved in fresh DMSO solvent (Sigma-Aldrich), and incubated overnight in the dark at room temperature. To remove the unbound dye (Figure 4.5), the solution was washed repeatedly by centrifugation to a final dilution of  $10^{-6}$ . Separation of the labeled protein from free dye was established firstly by using a Corning® Spin-X® UF 20 concentrator (polyethersulfone membrane (PES), Molecular weight cut-off (MWCO) 10 k, 20 ml) twice for 10 mins at 10 °C with acceleration 1,200 g and then further purification was done with an ultrafiltration centrifugal micro-concentrator (Sartorius VS0111, MWCO 10000, 500 uL) for 10 min at 10 °C with an acceleration of 10,000 g to a final dilution of  $10^{-6}$ . Washing was performed for each run at 10 °C to prevent denaturation, the concentrated protein was diluted with phosphate buffer (pH=7.2) and subjected to centrifugation cycles. For long-term storage, labeled Mb was divided into aliquots and frozen at -80 °C.

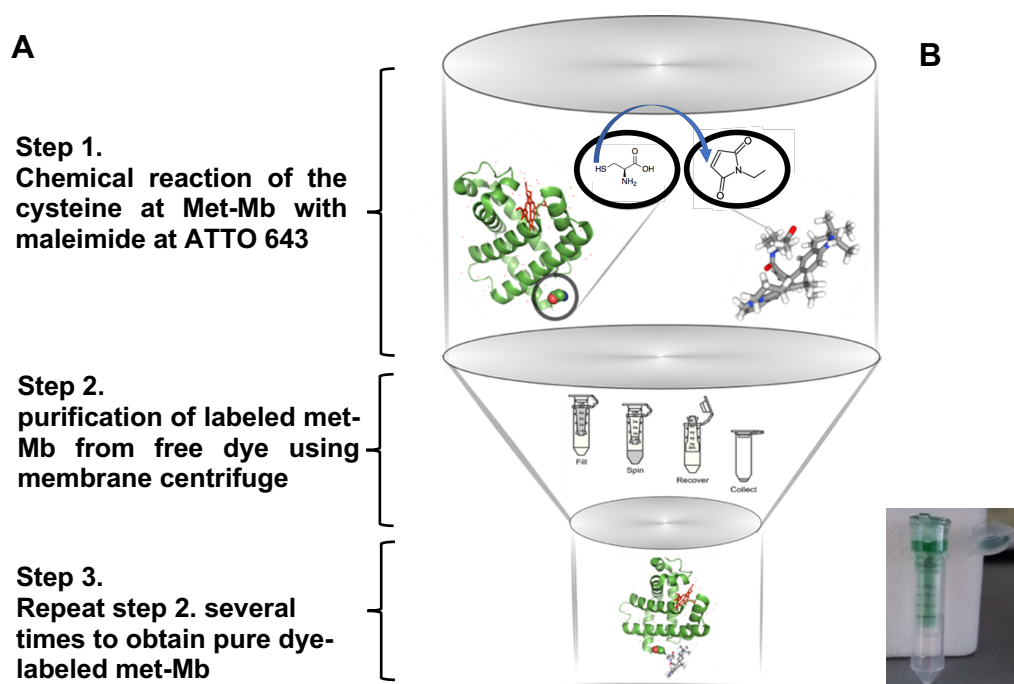


**Figure 4.5** (A) A schematic for labeling of cysteine-mutated met-Mb with ATTO 643 maleimide and purification of labeled met-Mb from the free dye using membrane centrifugation. (B) membrane centrifuge MWCO of 10 k used for separation of free dye after labeling of met-Mb.



N-terminal labeling was performed by the same protocol as for the cysteine 3 (mutagenesis serine 3) Mb except without the addition of DTT and TCEP. The N-terminus labeling protocol as recommended by Jena Bioscience GmbH was followed.<sup>17</sup> According to this method, horse heart met-Mb (Sigma-Aldrich) was N-terminally labeled with ATTO 740 NHS (N-Hydroxy succinimide) (ATTO-TEC GmbH, Siegen, Germany), which reacts with the NH<sub>2</sub> group of the N-terminus in PBS buffer (Sigma-Aldrich) at pH=7.2. However, before this reaction, the N-terminus was activated by adding sodium bicarbonate (1 M) (Sigma-Aldrich) to the protein solution to reach a final concentration of 100 mM and the mixture was vortexed shortly. Then, ATTO 740 label dissolved in dehydrated DMF solvent (Sigma Aldrich) was reacted with met-Mb in PBS (10 mM) with a dye to protein ratio of 3-3.5 for 2-3 hours at room temperature in the dark. The free unbound dye was removed through several centrifugation steps by the Vivaspin centrifugal concentrator (Sartorius VS0111, MWCO 10000, 500 uL) for 10 minutes at 10 °C to reach a final dilution of 10<sup>-6</sup>. The purified labeled Mb was stored in aliquots at -80 °C.

The degree of labeling (DOL) specifies the average number of fluorophore molecules per molecule of conjugate. The DOL was determined for the cysteine 3 met-Mb from UV-Vis absorption spectra (Figures 4.6, and 4.7) obtained from a droplet spectrophotometer with a light path of 1 mm. For N-terminally labeled met-Mb the absorption spectra (Figure 4.8) were measured on a UV-Vis spectrophotometer (Cary 50, Variant Inc., Agilent Technology, USA) with light path of 10 mm.

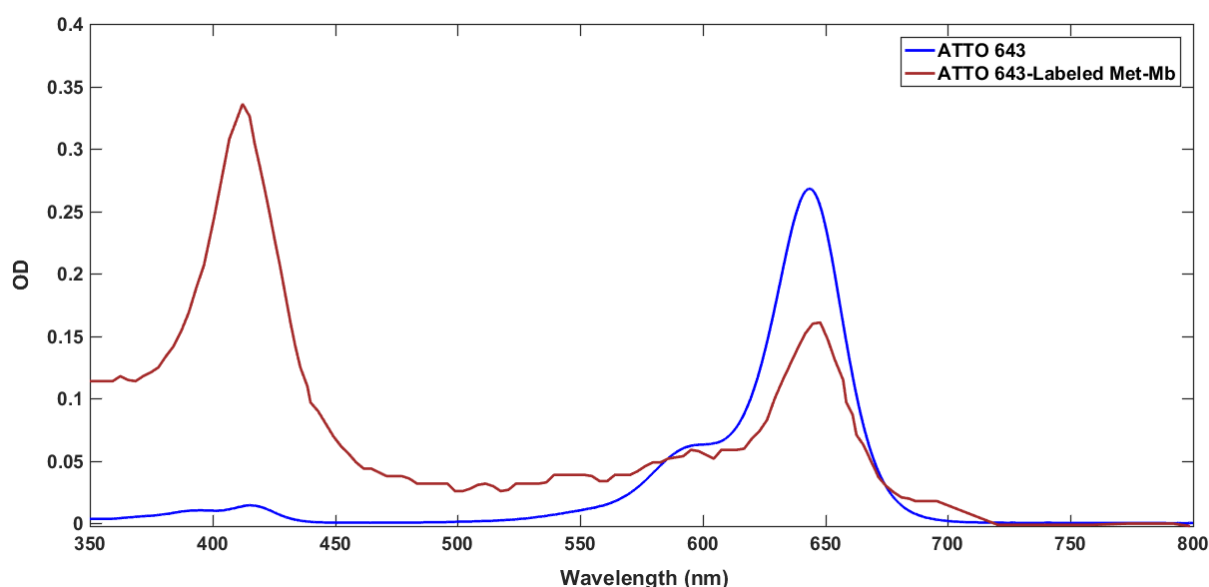


**Figure 4.6** Absorption spectrum of free ATTO 643 maleimide dye (blue) and ATTO 643-labeled mutated met-Mb (red) in potassium phosphate buffer (100 mM) at pH 7.2. Absorption at 409 nm arises from the Soret band of met-Mb, while the peak at 646 nm is due to the ATTO 643 dye.

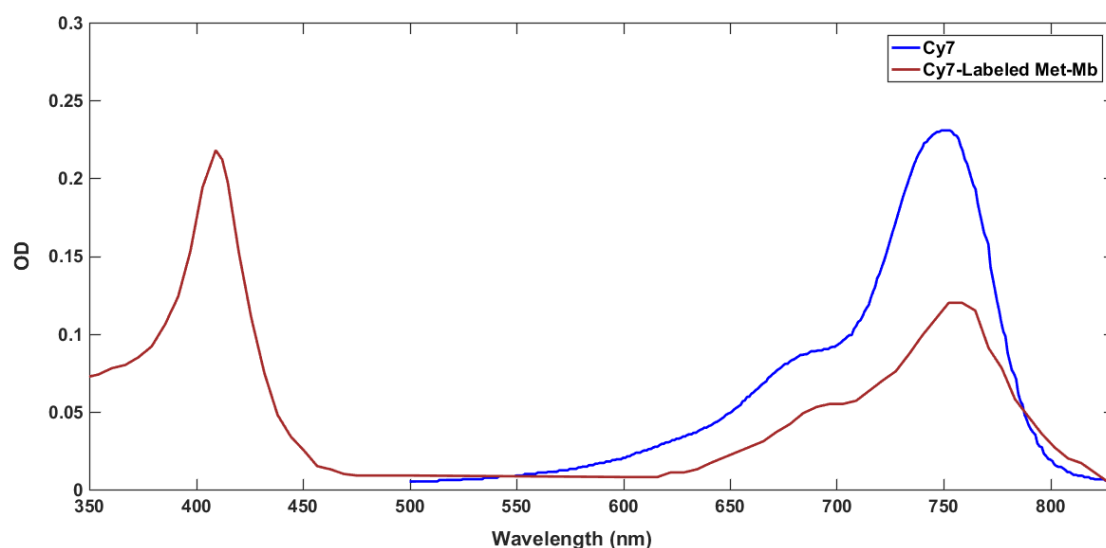


**Figure 4.7** Absorption spectrum of free Cy7 maleimide dye (blue) and Cy7 labeled-mutated met-Mb (red) in potassium phosphate buffer (100 mM). Absorption at 409 nm arises from the Soret band of met-Mb, while the peak at 751 nm is due to the labeled Cy7 dye.

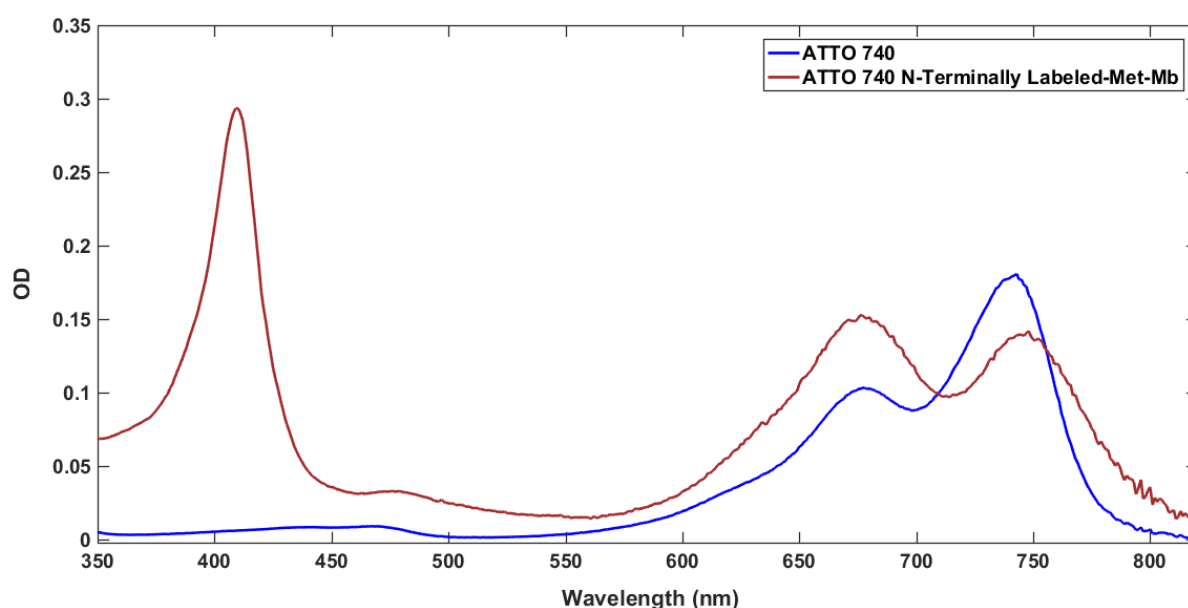


**Figure 4.8** Absorption spectrum of free ATTO 740 NHS dye (blue) and N-terminally labeled-met-Mb (brown) in PBS buffer (10 mM) at pH 7.2. Absorption at 409 nm arises from the Soret band of met-Mb while the peaks at 680 nm and 740 nm are due to the labeled ATTO 740 dye.

The concentration of bound dye and labeled protein are given by:  $c = A_{\max} / (\epsilon_{\max} \times d)$ , where  $\epsilon_{\max}$  is the extinction coefficient of the dye or protein at the absorption maximum and  $d$  is the path length of light in solution. The maximum absorption ( $A_{\max}$ ) of met-Mb, ATTO 643, Cy7, and ATTO 740 are at the wavelengths of 409 nm, 646 nm, 751 nm, and 740 nm ( $\lambda_{\max}$ ) respectively. The CF (Correction Factor), which is the ratio of  $\epsilon_{280} / \epsilon_{\max}$  for DOL calculation, have been reported (Table 4.2).

The DOL is calculated according to following formula: <sup>17</sup>

$$\text{DOL} = (A_{\text{max}} / \epsilon_{\text{max}}) / (A_{\text{protein}} / \epsilon_{\text{protein}}) \quad 4.2$$

$$\text{DOL} = (A_{\text{max}} \times \epsilon_{280}) / ((A_{280} - A_{\text{max}} \times \text{CF}_{280}) \times \epsilon_{\text{max}}), \quad 4.3$$

where  $A_{280}$  is the absorbance of the conjugate solution measured at 280 nm,  $A_{\text{max}}$  is the absorbance of the conjugate solution measured at  $\lambda_{\text{exc}}$ , the  $\lambda_{\text{exc}}$ ,  $\epsilon_{\text{max}}$ , and  $\text{CF}_{280}$  are intrinsic properties of the fluorescent dye, and  $\epsilon_{280}$ ,  $M_w$  are intrinsic properties of the used protein.

**Table 4.2** Spectral information of Met-Mb, ATTO 643, Cy7, and ATTO 740 in PBS at pH= 7.4 at 22 °C.

Sample	$\lambda_{\text{max}}$ (nm)	Maximum molar extinction coefficient ( $\epsilon_{\text{max}}$ ) <sup>a</sup> $\text{M}^{-1} \text{cm}^{-1}$	Correction Factor ( $\text{CF}_{280}$ ) <sup>a</sup> ( $\epsilon_{280} / \epsilon_{\text{max}}$ )
Met-Mb	280	43900	-
Met-Mb	409	188000	-
ATTO 643	646	150000	0.04
Cy7	751	199000	0.029
ATTO 740	740	120000	0.07

<sup>a</sup> as specified by the manufacturer

The ratio of bound dye and the amount of reacted protein yields the DOL by eliminating the absorbance of the dye coupled to the protein. Regarding calculation of the protein concentration, there are two options: using the absorption of conjugate met-Mb at the Soret-band (409 nm), or the absorption of conjugate met-Mb at 280 nm. The two possibilities have been tried to calculate the DOL for met-Mb labeled at the N-terminus with ATTO 740. The DOL calculated on the basis of formula (Eq. 4.3) was 69.1% and the calculated DOL based on the absorption of conjugate protein at Soret-band (409 nm) was 73.1% (Eq. 4.2). Calculation by the first method for ATTO 643 and Cy7 labeled met-Mb (Table 1), yielded DOL's of 61.6%, and 51.7%, respectively.

#### 4.2.5 Preparation of ATTO 643-, Cy7-, and ATTO 740 -labeled deoxy-Mb and MbCO

We labeled S3C sperm whale met-Mb with ATTO 643 and Cy7. We labeled horse heart met-Mb with ATTO740. From those, we obtained labeled deoxy-Mb and MbCO as described in Chapter 3, section 3.2.1. Figure 4.9 shows one example, the absorption spectrum of ATTO 643-labeled S3C MbCO in phosphate buffer (pH=7.2).

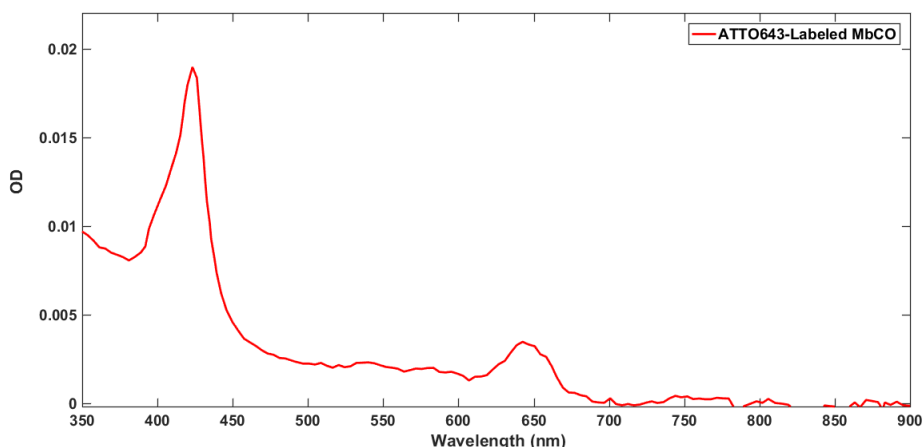


**Figure 4.9** Absorption spectrum of ATTO 643-labeled S3C MbCO in potassium phosphate buffer (100 mM) at pH 7.2. The band at 422 nm is the Soret band of MbCO, while the peak at 646 nm is due to the ATTO 643 dye label.

#### 4.2.6 Ensemble fluorescence lifetime measurements of ATTO 643-, Cy7-, and ATTO 740-labeled Mb

Two setups for fluorescence lifetime measurement have been used. One experiment has been done in Munich at the laboratory of Prof. Don C. Lamb in LMU and the other setup was a homemade microscope in Leiden University.

The setup in Munich for fluorescence lifetimes was an Edinburgh FLS1000 (Edinburgh Instruments, Livingston, United Kingdom) fluorescence lifetime spectrometer (Figure 4.10). Decay measurements were performed using time-correlated single-photon counting (TCSPC). The dyes were excited using 640 nm and 730 nm lasers for ATTO 643 and Cy7, respectively.

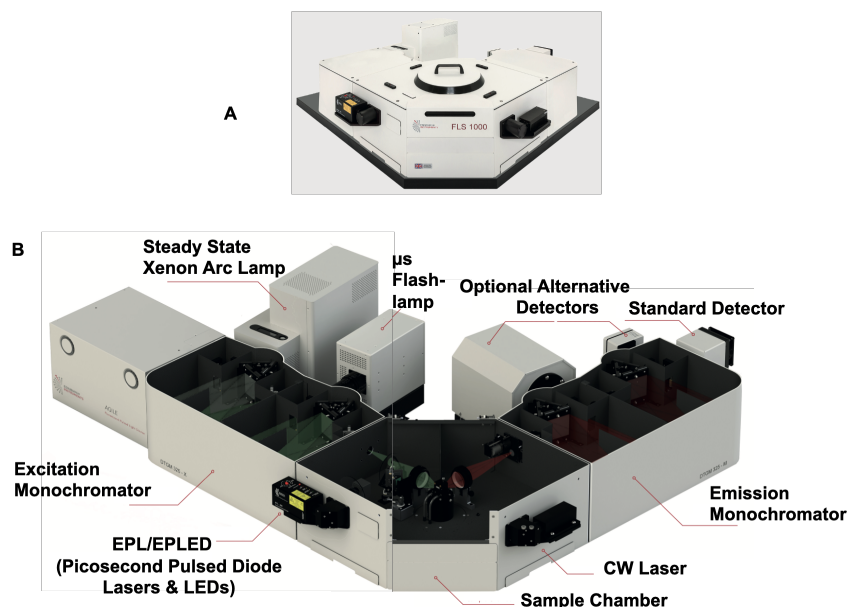


**Figure 4.10** (A) Schematic of the fluorescence lifetime spectrometer FLS 1000 at the LMU, (B) Details of the FLS 1000 setup for lifetime measurement of ATTO 643, Cy7, and labeled protein [after <sup>18</sup>].

The setup in Leiden university was a homemade microscope in which ATTO 740 is excited with a pulsed laser at 636 nm with a pulse repetition rate of 26 MHz, which was the red-most laser available but was not optimal for ATTO740 excitation. The schematic illustration of the setup is shown in Figure 4.12. The collected photons were quantified with time-correlated single-photon counting (TCSPC) and converted by the SymphoTime software to lifetime data. Figure 4.13 shows the designed mini-cuvette with an inlet and outlet for bubbling gas inside the solution on top of the microscope for the preparation of deoxy-Mb and MbCO from met-Mb state as described in Chapter 3, section 3.2.1.

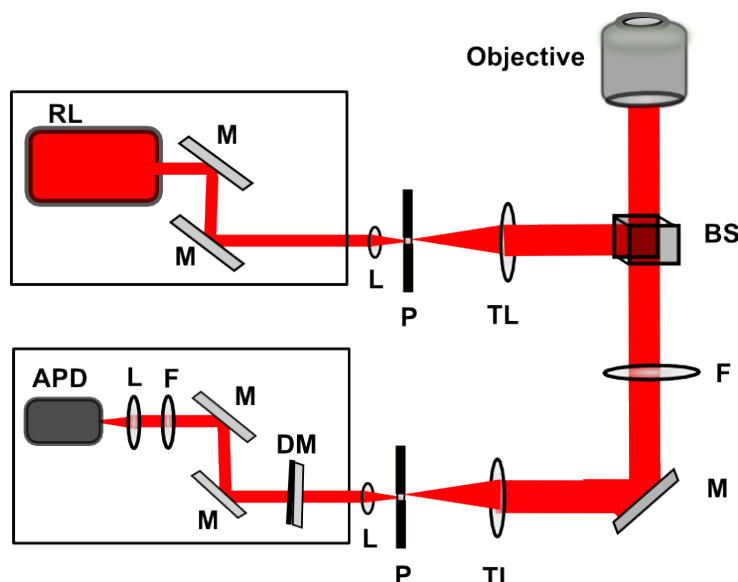


**Figure 4.12.** A schematic of the home-made confocal microscope setup of Leiden University used for the lifetime measurement of ATTO 740 and ATTO 740-labeled protein. RL=Red Laser, M=Mirror, L=Lens, P=Pinhole, TL=Telescope (Beam Expander), BS=Beam splitter, F=Filter, DM=Dichroic Mirror, APD=Avalanche Photodiode Detector.

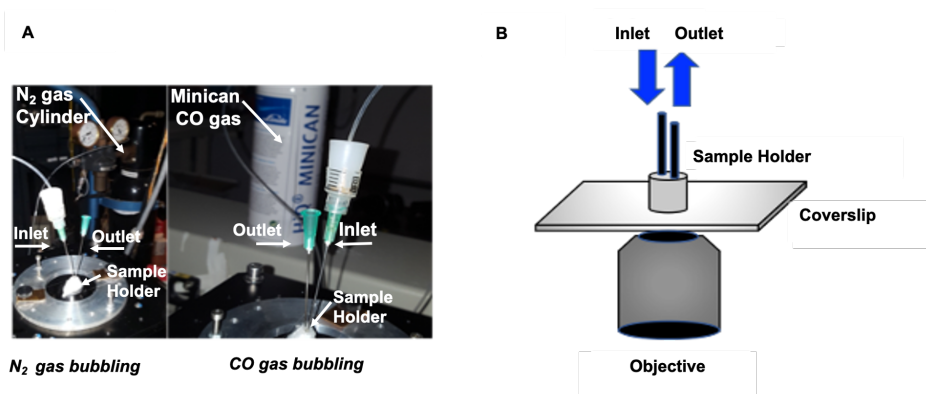


**Figure 4.13** (A) A picture of the microscope used for lifetime measurement showing the sample holder on top of microscope with inlet and outlet paths for N<sub>2</sub> or CO gas bubbling. Lifetime measurements were performed in the solution while focusing the laser beam 5-10 microns above the glass. (B) The designed sample holder (volume 10  $\mu$ L) with inlet and outlet pathways for gas bubbling to prepare deoxy-Mb and MbCO from met-Mb on the microscope.

#### 4.2.7 Comparison of ensemble fluorescence lifetime measurement of ATTO 643-, Cy7-, and ATTO 740-labeled deoxy-Mb, MbCO, and met-Mb

First, we measured the fluorescence lifetimes of ATTO 643 (170 nM), Cy7 (177 nM) dyes alone and of ATTO 643-(170 nM), and Cy7-labeled (177 nM) deoxy-Mb, MbCO, and met-Mb in potassium phosphate buffer; pH=7.2 using the Edinburgh FLS1000 instrument for 5 minutes and exciting with a pulsed laser at 640 nm with a pulse rate of 21 MHz. The photons collected using TCSPC were converted by the SymphoTime software to lifetime data. Figures 4.10, and 4.11 and Table 4.3 show the results of fluorescence lifetime measurements for ATTO 643 and Cy7 dyes and ATTO 643-, and Cy7-labeled deoxy-Mb, MbCO, and met-Mb.

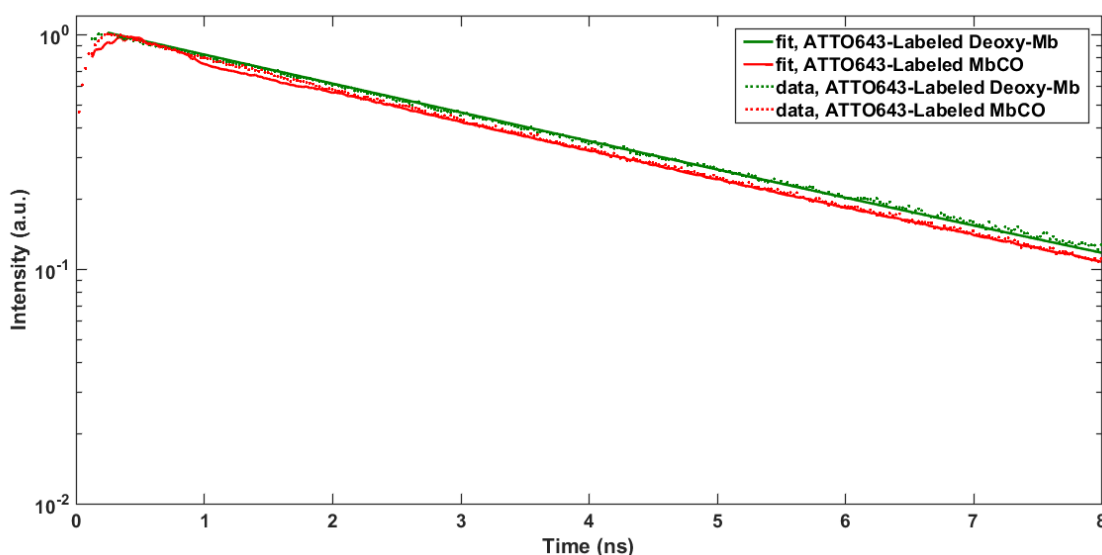


**Figure 4.10** Fluorescence decays of ATTO 643-labeled deoxy-Mb (green), and MbCO (red) in potassium phosphate buffer (100 mM) at pH 7.2. Experimental data (dotted lines) and single-exponential fits (solid lines).

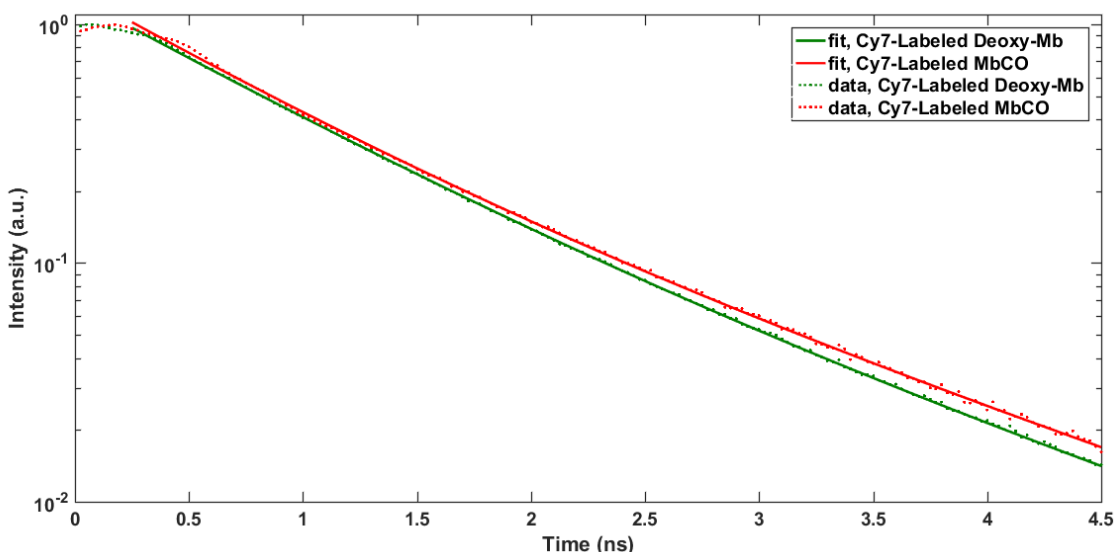


**Figure 4.11** Fluorescence decays of Cy7-labeled deoxy-Mb (green) and MbCO (red) in potassium phosphate buffer (100 mM) at pH 7.2. Experimental data (dotted lines) and bi-exponential fits (solid lines).

**Table 4.3** Comparison of the fluorescence lifetimes of ATTO 643 dye (170 nM) and Cy7 (177 nM) and ATTO 643, and Cy7-labeled deoxy-Mb, MbCO, and met-Mb in potassium phosphate buffer (100 mM), pH=7.2, at room temperature. Excitation was performed using a pulsed laser at 640 nm and 21 MHz repetition rate.

Sample	Experimental Lifetime (ns)
ATTO 643 dye	3.6 <sup>a</sup>
ATTO 643 -deoxy-Mb	3.54
ATTO 643 -MbCO	3.30
ATTO 643 -met-Mb	2.75
Cy7 dye	0.45 <sup>b</sup>
Cy7-deoxy-Mb	0.84
Cy7-MbCO	0.81
Cy7 -met-Mb	0.70

<sup>a</sup> lifetime specified by the manufacturer as 3.5 ns in PBS buffer, pH =7.4 and 22 ° C

<sup>b</sup> lifetime as specified in literature is 0.43 ns<sup>19</sup>

As can be seen, there is a quenching effect in the ATTO 643 and Cy7-labeled met-Mb form compared to ATTO 643 and Cy7-labeled deoxy-Mb forms. In contrast, there is almost no difference between the lifetimes of the ATTO 643, and Cy7-labeled deoxy-Mb and MbCO forms of Mb. For the Cy7 label, the measured lifetime of the free dye is significantly shorter (0.45 ns) than of the attached dye, which may be because of the environmental sensitivity of Cy7 fluorophore, for example, by limiting dye distortions and conformational fluctuations. It should be noted that in fitting the data, the decays were considered to be mono-exponential.

Secondly, we measured the fluorescence lifetimes of free ATTO 740, and ATTO 740-labeled deoxy-Mb, MbCO, and met-Mb using our homemade setup in Leiden University. The sample was in PBS buffer, pH=7.2, in a cuvette and was excited with a pulsed laser at 636 nm with a repetition rate of 26 MHz for 4 minutes. The collected photons were quantified using TCSPC and converted by the SymphoTime software to lifetime data. Figures 4.14, 4.15, 4.16 and Table 4.5 show the results of the fluorescence lifetime measurements.

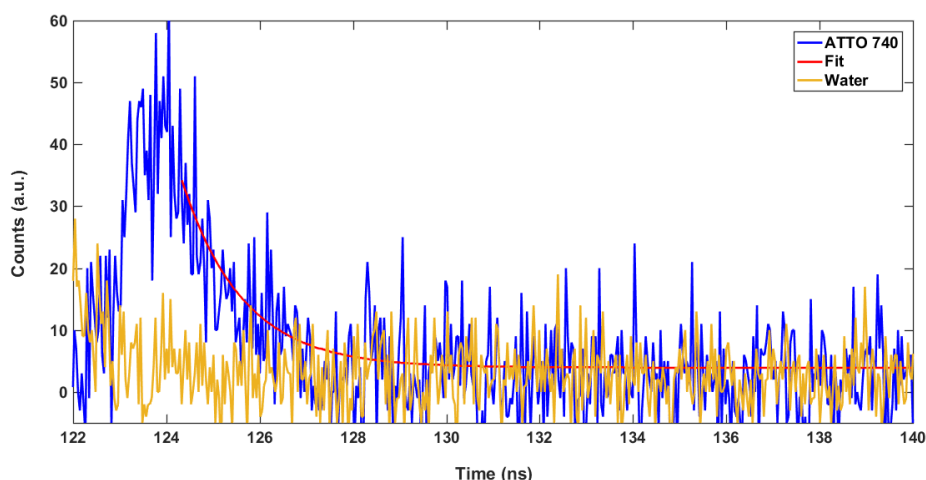


**Figure 4.14** Fluorescence decays of free ATTO 740 dye (blue), the fit (red), and water (yellow).



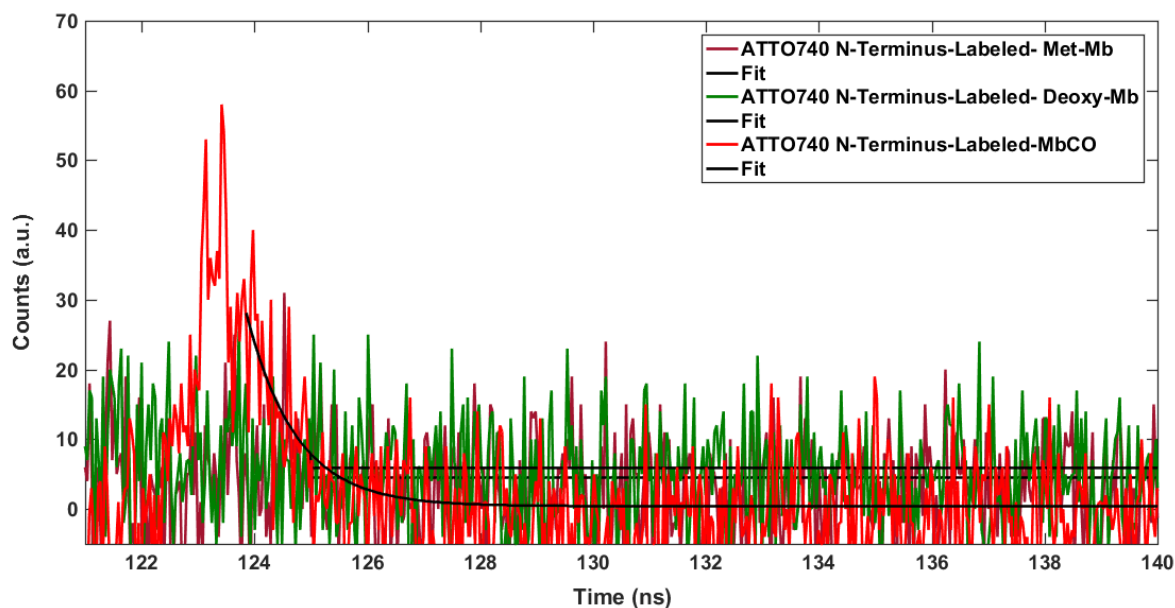


**Figure 4.15** Fluorescence decays of ATTO 740 -labeled met-Mb (purple), ATTO 740 -labeled deoxy-Mb (green), ATTO 740 -labeled MbCO (red), and the respective fits (black).

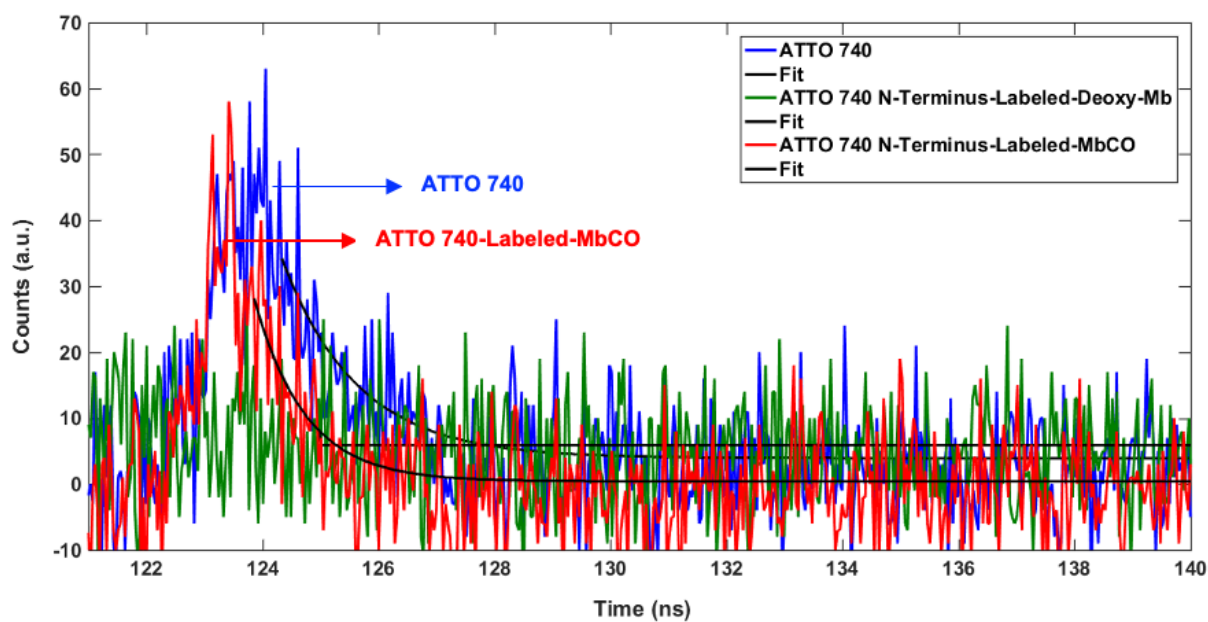


**Figure 4.16** Comparison of the fluorescence decays of free ATTO 740 (blue), ATTO 740 -labeled-deoxy-Mb (green), ATTO 740 -labeled-MbCO (red), and the respective fits (black).



**Table 4.5** Fluorescence lifetimes of ATTO 740 and ATTO 740-labeled deoxy-Mb, MbCO, and met-Mb.

Sample	Experimental Lifetime (ns)
ATTO 740 dye	1.2 <sup>a</sup>
ATTO740 labeled-deoxy-Mb	N.A.
ATTO740 labeled-MbCO	0.87
ATTO740 labeled-met-Mb	N.A.

<sup>a</sup> lifetime specified by the manufacturer as 0.65 ns in PBS buffer, pH =7.4 and 22 ° C

Figure 4.14 demonstrates the decay of free ATTO 740 dye (177  $\mu$ M) compared to a blank sample (water). The measured lifetime was 1.2 ns. The fluorescence trace of a solution of met-Mb N-terminally labeled with ATTO 740 (234  $\mu$ M, containing 177  $\mu$ M dye based on a calculated 75% DOL) was measured for 4 minutes before and after reduction with sodium dithionite under oxygen-free atmosphere and N<sub>2</sub> bubbling to produce the deoxy form. Finally, the sample was bubbled with CO gas for 10 minutes and the fluorescence decay was followed for 4 minutes under the same conditions as for the dye labeled-deoxy and met-Mb samples. Figure 4.15 shows the fluorescence decays of ATTO 740 -labeled-met-Mb (intensity close to background)), ATTO 740 -labeled deoxy-Mb (intensity close to background)), and ATTO 740-labeled MbCO (Intensity of 40 counts, lifetime 0.87 ns). In Figure 4.16, the fluorescence decay of free ATTO 740 (intensity of 50 counts, lifetime 1.2 ns) has been compared to the ATTO 740 N-terminus-labeled-deoxy-Mb and ATTO 740 -labeled-MbCO (red), and fit (black). The measured lifetimes are collected in Table 4.5.

For the ATTO 740-labeled met-Mb and deoxy-Mb forms, the fluorescence intensity is low because of quenching by the absorption bands of met-Mb and deoxy-Mb, whereas a higher intensity is observed for ATTO 740 labeled-MbCO, which has much less absorption in the near infra-red region.

Because of low intensity, low signal-to-noise ratio, and interference with the IRF ( $\tau \sim 0.6$  ns), the data collected in this experiment can be interpreted based on only the difference in intensities and not on measured lifetime data.

## 4.3 Discussion

### 4.3.1 Fluorescent labelling and preparation of the different states of Mb

In summary, the purification and dye-labeling of Mb yielded a degree of labeling of 50-65% for sperm whale Mb variants and 65-75% for N-terminus labeling of horse heart Mb (Figures 4.6-4.8).

ATTO643-, Cy7-, and ATTO740-deoxy-Mb, and -MbCO (Figures 4.9) were prepared with the same protocol as used for the preparation of unlabeled deoxy-Mb and MbCO and the preparations exhibited the expected absorption spectrum containing the respective Soret-band, Q-bands and NIR bands.

### 4.3.2 Comparison of calculated Förster resonance energy transfer parameters and experimental lifetime

In this section, we calculate the Förster resonance energy transfer parameters such as Förster radius ( $R_0$ ), energy transfer rate ( $k_{ET}$ ), and energy transfer efficiency ( $E$ )

for ATTO643-, Cy7-, and ATTO740-deoxy-Mb, and MbCO and then compare the calculated results with the experimental data and the lifetimes of the corresponding free dyes.

### 4.3.3 Förster resonance energy transfer radius ( $R_0$ )

The Förster resonance energy transfer (FRET) efficiency and  $R_0$  have been calculated using equation (1.1) in chapter 1.

The Förster radii of deoxy-Mb and MbCO labeled with ATTO 643 and Cy7 were calculated in MatLab (The MathWorks, Inc., Natick, Massachusetts, United States.) using the spectra published by Bowen [7]. For all calculations,  $\kappa^2$  was assumed to be 2/3 and the refractive index was set at  $n=1.33$ . The results are given in Table 4.1.

### 4.3.4 Förster Resonance Energy Transfer Rate ( $k_{ET}$ ) and Energy Transfer Efficiency ( $E$ )

The rate of energy transfer ( $k_{ET}$ ) has been calculated with the following equation:

$$k_{ET} = \left(\frac{R_0}{r}\right)^6 \left(\frac{1}{\tau_D}\right) \quad 4.4$$

To estimate the rates of energy transfer in dye-labeled Mb, the distance  $r$  between heme and dye was estimated based on two hypotheses. Hypothesis A is that the distance between dye and heme center is maximum (Figure 4.17A) and  $r$  is the distance of the heme center to the attachment position of the dye to the protein, including the full extended linker length ( $r = r_P + r_{Linker}$ ). The other hypothesis, B, is that the two dipole moments are at the minimum distance (Figure 4.17B) and  $r$  is equal to the distance from the heme center to the attachment position of the dye to the protein, subtracting the linker length ( $r = |r_P - r_{Linker}|$ ). Other possible positions will lie between these two above-mentioned extreme hypotheses. For example, by ignoring the linker length of dye  $r$  is equal to  $r_P$  (Figure 4.17C). It should be noted that the hypothesis of ( $r = |r_P - r_{Linker}|$ ) in the reality is not true and can be ignored. It is depicted for comparison with other two possible hypothesis about  $r$ .

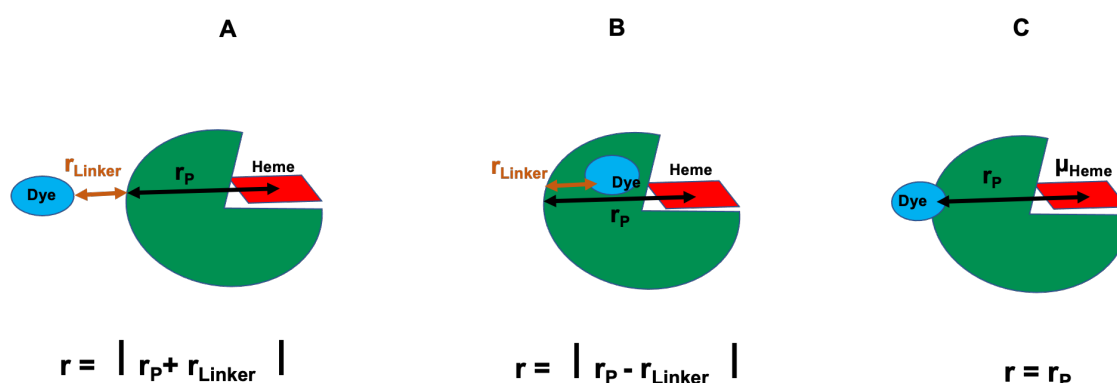


**Figure 4.17** Illustrative schema for  $r$  assumption in which  $r_P$  is the distance of heme center to the attachment position of dye to the protein and  $r_{Linker}$  is the linker length that connects the dye to the protein: (A) The dye is at the maximum distance to the center of heme ( $r = |r_P + r_{Linkers}|$ ), (B) The dye is at the minimum distance to the center of heme ( $r = |r_P - r_{Linkers}|$ ), (C) Ignoring the linker length of dye and  $r$  is equal to  $r_P$ .

The distance between serine 3 and the center of the heme ( $r_P$ ) is 27.4 Å (Figure 4.18A) in the crystal structure of sperm whale Mb (PDB: 1VXA) and the linker lengths to the core of the dye ( $r_{\text{Linker}}$ ) are 11.3 Å (Figure 4.18B) and 15.7 Å (Figure 4.18C) for ATTO 643 and Cy7, respectively. All distance measurements were performed in PyMol. For the calculation of  $k_{ET}$  and  $E$ , we assume maximum distance between dye and the center of the heme (Figure 4.17A,  $r = |r_P + r_{\text{Linker}}|$ ) which is estimated to be 38.7 Å and 43.1 Å for ATTO 643 and Cy7-labeled sperm whale Mb respectively (Figure 4.18).

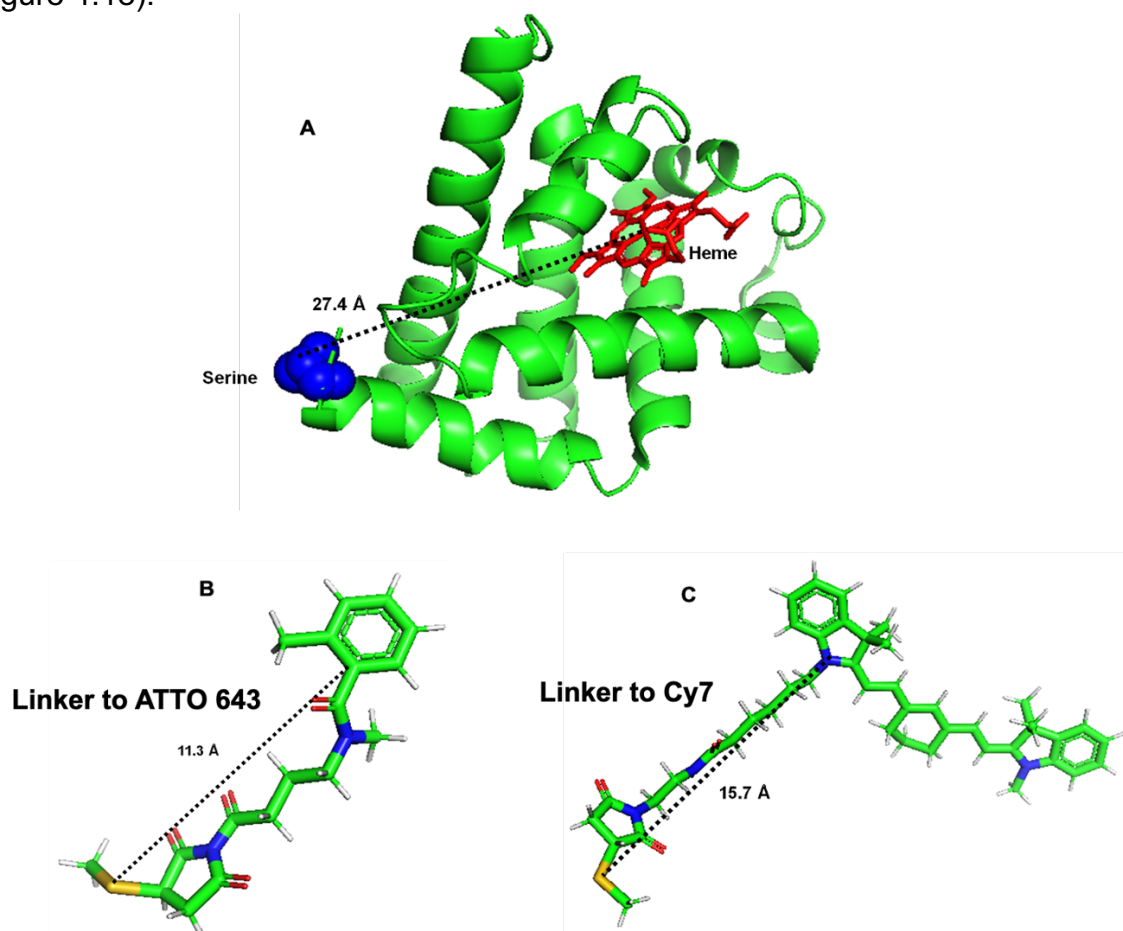


**Figure 4.18** Distance between dye and heme based on PyMOL distance calculations. The distance was calculated as the sum of (A) the distance from attachment position of dye on the serine 3 to the center of the heme (27.4 Å) in native sperm whale Mb (PDB: 1VXA) plus (B) the linker length to the ATTO 643 dye (11.3 Å), or (C) the linker length to the Cy7 dye (15.7 Å).

The fluorescence lifetime of ATTO740-N-terminally labeled horse heart Mb in deoxy and carboxy was calculated by using equation (4.6) (Table 4.12).

The distance from attachment position of dye to the Glycine 1 to the center of the heme ( $r_P$ ) is 24.2 Å (Figure 4.19A) in the crystal structure of horse heart Mb (PDB: 1WLA). The linker length to the dye is 11.3 Å (Figure 4.19B) for ATTO 740. All distance measurements were performed in PyMol. For calculation of  $k_{ET}$  and  $E$ , we assume  $r = |r_P + r_{\text{Linker}}|$  which is estimated to be 35.5 Å for ATTO 740-labeled horse heart Mb (Figure 4.18).

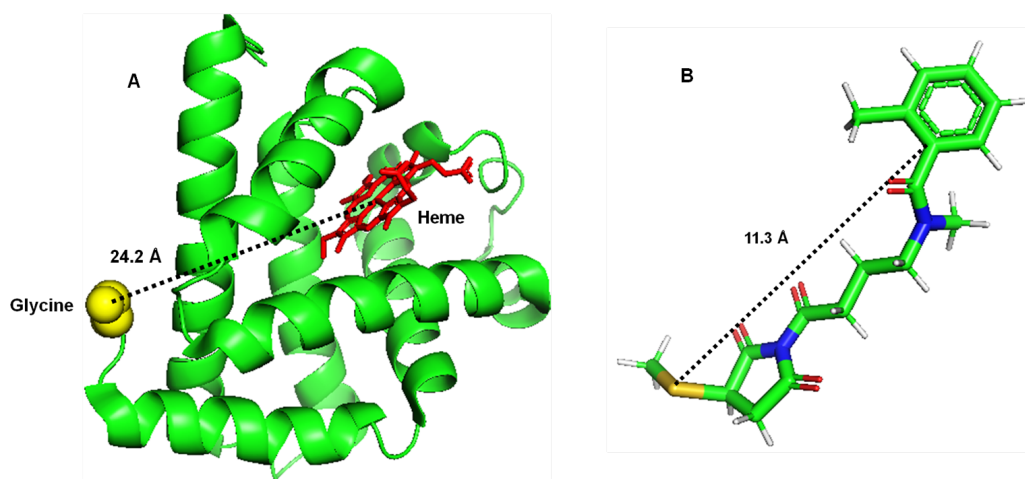


**Figure 4.19** Estimation of the distance between dye and heme based on PyMOL distance calculations. The distance was calculated as the distance from the attachment position of dye on the glycine 1 to the center of the heme (24.2 Å) in horse heart Mb (PDB: 1WLA) plus the linker length to the dye (ATTO 740: 11.3 Å).

The  $k_{ET}$  values were then calculated and the results shown in Table 4.12 for ATTO 643- and Cy7-labeled sperm whale deoxy-Mb, and MbCO, and ATTO 740-labeled horse heart deoxy-Mb, MbCO based on the value of  $R_0$  (Table 4.1),  $\tau_D$  (lifetime of free dyes as specified by the manufacturer, and in the case of Cy7, the lifetime as specified in literature <sup>19</sup>) and the assumed distances  $r$  ( $|r_P + r_{Linker}|$ ) (Figures 4.18A, and 4.19A).

The energy transfer efficiency ( $E$ ) depends on the distance ( $r$ ) between the donor and acceptor with an inverse 6th-power law due to the dipole–dipole coupling mechanism:

$$E = \frac{1}{1 + \left(\frac{r}{R_0}\right)^6} \quad 4.5$$

Calculated  $E$  values for ATTO 643, Cy7, and ATTO 740 dye labeled deoxy-Mb, and MbCO are given in Table 4.12.

#### 4.3.2.3 Calculation of the fluorescence lifetimes of the dyes bound to Mb ( $\tau_{DA}$ )

The lifetime of dyes attached to Mb ( $\tau_{DA}$ ) can be calculated by the following formula:

$$\tau_{DA} = \frac{\tau_D}{1 + \left(\frac{R_0}{r}\right)^6} \quad 4.6$$

In this formula  $\tau_D$ ,  $r$ , and  $R_0$  are the lifetime of the dye in absence of an acceptor, the donor-acceptor distance, and the Förster radius, respectively.

The values of  $\tau_{DA}$  were calculated for ATTO 643 and Cy7, and ATTO 740 dye labeled deoxy-Mb, MbCO (Table 4.12).

**Table 4.12** Calculated  $R_0$  (Eq 4.1), FRET rate ( $k_{ET}$ ) (Eq 4.4) and Energy Transfer Efficiency ( $E$ ) (Eq 4.5), lifetime (Eq 4.6) and experimental lifetime for ATTO 643-, Cy7-, and ATTO 740-deoxy-Mb, and MbCO and lifetimes of corresponding three free dyes.

Sample	$R_0$ (nm)	$k_{ET}$ (ns <sup>-1</sup> )	$E$	Calculated Lifetime <sup>c</sup> (ns)			Experimental Lifetime (ns)
				$r =$ $r_P + r_{Linker}$	$r =$ $r_P$	$r^d =$ $r_P - r_{Linker}$	
<b>ATTO643</b>	-	-	-	-			3.5
<b>ATTO643 - deoxy-Mb<sup>a</sup></b>	3.54	0.16	0.36	2.24	0.63	0.031	3.54
<b>ATTO643- MbCO<sup>a</sup></b>	2.46	0.018	0.06	3.29	2.28	0.25	3.30
<b>Cy7</b>	-	-	-	-			0.43
<b>Cy7 - deoxy-Mb<sup>a</sup></b>	2.99	0.23	0.1	0.39	0.2	0.001	0.84
<b>Cy7 - MbCO<sup>a</sup></b>	2.00	0.02	0.01	0.43	0.37	0.017	0.81
<b>ATTO 740</b>	-	-	-	-			0.65
<b>ATTO 740 - deoxy-Mb<sup>b</sup></b>	2.54	0.21	0.11	0.57	0.33	0.01	N.A.
<b>ATTO 740- MbCO<sup>b</sup></b>	1.66	0.016	0.01	0.64	0.59	0.11	0.87

<sup>a</sup> Dye labeled-mutated Mb (sperm whale)

<sup>b</sup> N-terminus-labeled Mb (Horse Heart)

<sup>c</sup> The lifetimes were calculated based on the  $\tau_D$  that has been reported by the manufacturer except for Cy7 that the lifetime has been used from ref. <sup>19</sup>.

<sup>d</sup> As mentioned before the hypothesis of  $r = r_P - r_{Linker}$  in the reality is not true and is ignored, however, the data is reported for comparison to other two calculated  $r$ .

Based on the calculated  $k_{ET}$  and  $E$ , the energy transfer probability for ATTO 643-labeled deoxy-Mb compared to ATTO 643-labeled-MbCO, is six times more efficient and almost nine times faster while for Cy7 labeled deoxy-Mb compared to Cy7 labeled-MbCO, energy transfer efficiency is ten times faster and  $k_{ET}$  is almost twelve times larger. In addition, based on equation 4.4 and 4.5, the calculated  $k_{ET}$ , and  $E$  values for ATTO 740 labeled deoxy-Mb, and MbCO are: 0.21 ns<sup>-1</sup>, 0.01 ns<sup>-1</sup> and, 0.11, 0.01 respectively (Table 4.11), and the calculated  $k_{ET}$  and  $E$ , the energy transfer for ATTO 740-labeled deoxy-Mb compared to ATTO 740-labeled-MbCO, is around 10 times more efficient and almost 13 times faster, which is approximately similar to what we have calculated for Cy7.

This considerable difference in  $k_{ET}$  and  $E$  between ATTO 643 and both Cy7 and ATTO 740 is mainly due to the better spectral overlap of the emission of Cy7 and ATTO 740 with the absorption of deoxy-Mb with respect to MbCO than for ATTO 643.

In the case of ATTO 643, the calculated lifetime of the labeled-MbCO is close to the experimentally measured lifetime, however, for the deoxy-Mb form, there is a large difference between calculated and experimental results (Table 4.12). This discrepancy may be due to the significant simplification inherent in the calculated distance, e.g., by the fact that it ignores any orientational effects.

For Cy7 attached to Mb, both forms showed significantly longer lifetimes than those predicted by the calculations, possibly due to the dye attachment on the protein having changed the fluorescent properties of the dye. However, the fact that no significant change in lifetime between the two forms could be observed experimentally is in line with the calculated lifetime differences (Table 4.12).

Regarding the ensemble experimental fluorescence lifetimes of S3C Mb variants, we could not see a difference in lifetime between ATTO 643- and Cy7-labeled deoxy-Mb and -MbCO. However, for ATTO 643- and Cy7-labeled met-Mb, some quenching due to FRET has been observed possibly because of the improved overlap between emission spectra of Cy7 and ATTO 643 dyes with absorption spectrum of met-Mb compared to the other two forms. In the case of deoxy-Mb and MbCO, one possible explanation for this result, is that the dyes have been attached too far away from the heme.

For Cy7, not only the experimental decays show no difference between deoxy-Mb and MbCO but also the highly idealized calculations predict only a relatively small lifetime change. It should be noted that the experimental results showed that binding Cy7 to the Mb is accompanied by a significant change in lifetime (longer) compared to the free dye which is due to the environmental sensitivity of this fluorophore, particularly by limiting dye distortions and conformational fluctuations. The longer lifetime of the dye after attachment to the protein, however, would help us to measure the lifetime more accurately with better resolution.

Interestingly, in the case of ATTO 643, calculations predict a visible effect. The lack of a visible effect in the experimental data may be because the labeling position yields an unfavorable orientation of the dye toward the heme due to steric hindrance, reducing the FRET efficiency. However, it should be pointed out that some quenching effect is visible for met-Mb with both dyes (Table 4.3). Since met-Mb has the largest Förster radius of the three forms, this further points towards a too large of distance, possibly coupled with unfavorable attachment geometry.

Regarding the experimental ensemble fluorescence lifetime of N-terminally labeled Mb, the fluorescence decays of different variants and of the free dye show different intensities. For the met and deoxy forms, the intensity is low, presumably because of fluorescence quenching. However, as expected, the intensity is larger for ATTO 740-labeled MbCO. So the CO form of labeled Mb can be distinguished from the other two forms (deoxy and met forms) on the basis of the fluorescence intensities. The low fluorescent intensity and interference with the IRF ( $\tau \sim 0.6$  ns) do not allow for sufficiently precise lifetime data.

Comparing calculated values of  $R_0$ ,  $k_{ET}$ , and  $E$  for Cy7 and ATTO740 with deoxy-Mb and MbCO shows a difference between the two Mb forms (Table 4.12). But experimentally, for Cy7, the difference between the two forms of Mb could not be distinguished (Figure 4.11) while, for ATTO 740, the two states could be recognized on the basis of the intensity of the fluorescent decay (Figure 4.15). This remarkable difference between ATTO 740 and Cy7 can be connected to the different  $R_0$  values

and how the dyes after labeling interact with the protein and solution, which directly affects the orientation and distance of the dye to the heme center ( $r$ ), resulting in different quenching.

It is worth mentioning that, although we could not see the difference between the two states in ATTO 643 and Cy7 labeled-deoxy-Mb and -MbCO (Table 4.3), we could see a significant difference (based on the fluorescence intensity) for ATTO 740-labeled-deoxy-Mb and -MbCO, which will allow us to monitor these two states in a mixture after illumination of labeled-MbCO with near infra-red light and to study the rebinding kinetics of CO. It might enable successful single molecule-FRET monitoring of CO unbinding and rebinding.

Finally, we should consider that the dyes, after attachment to the protein, may change their spectral properties and even the properties of the protein and that this may affect the FRET efficiencies and the kinetics of binding and rebinding.

## 4.4 Conclusion

Based on the results of Chapter 3, we concluded that the illumination of MbCO with near infra-red light (700-800 nm) does not break the Mb-CO bond efficiently and we estimated that MbCO will be stable with an upper estimate of dissociation quantum yield less than 6% under illumination with near infra-red light ( $\lambda > 700$  nm).

We used FRET by which the donor emission is quenched through a non-fluorescent acceptor (the protein heme) that can be used to study the kinetics of CO rebinding. In our experiments, the acceptors are the different states of myoglobin, which exhibit different quenching efficiencies. For example, deoxy-Mb in which CO is unbound from Mb acts as a more efficient quencher than MbCO, where CO is bound to Mb.

In chapter 4, we have labeled MbCO with dyes which emit in the near infra-red (ATTO 740 and Cy7). This enables studies of the energy transfer from the dye to the Mb when illuminating with  $\lambda > 700$  nm. However, it is essential to be able to distinguish between MbCO and deoxy-Mb when illuminating Mb with near infra-red light. Based on the results of Chapter 4, we could observe a significant difference (based on the fluorescence intensity) for ATTO 740 labeled-deoxy-Mb and -MbCO, which reveals the possibility to distinguish these two states in a mixture. Here, we can use infrared illumination of the labeled-MbCO to study rebinding kinetics of CO to the labeled-deoxy-Mb. These results open a new research area for single molecule-FRET experiments, which is sensitive and specific for labeled molecules and provides useful information about heterogeneity of rates and molecules in an ensemble.

## References

- (1) Eftink, M. R.; Shastry, M. C. Fluorescence Methods for Studying Kinetics of Protein-Folding Reactions. *Methods Enzymol.* **1997**, 278, 258–286.
- (2) Brown, M. P.; Royer, C. Fluorescence Spectroscopy as a Tool to Investigate Protein Interactions. *Curr. Opin. Biotechnol.* **1997**, 8 (1), 45–49.
- (3) Schuler, B. Single-Molecule Fluorescence Spectroscopy of Protein Folding. *ChemPhysChem* **2005**, 6 (7), 1206–1220.
- (4) Schuler, B. Single-Molecule FRET of Protein Structure and Dynamics - a Primer. *J. Nanobiotechnology* **2013**, 11 (1), S2.

- (5) Pradhan, B.; Engelhard, C.; Mulken, S. V.; Miao, X.; Canters, G. W.; Orrit, M. Single Electron Transfer Events and Dynamical Heterogeneity in the Small Protein Azurin from *Pseudomonas Aeruginosa*. *Chem. Sci.* **2020**, *11* (3), 763–771.
- (6) Cupane, A.; Leone, M.; Vitrano, E.; Cordone, L. Structural and dynamic properties of the heme pocket in myoglobin probed by optical spectroscopy. *Biopolymers* **1988**, *27*(12), 1977–1997.
- (7) The absorption spectra and extinction coefficients of myoglobin - PubMed <https://pubmed.ncbi.nlm.nih.gov/18119239/> (accessed 2022 -04 -01).
- (8) Direct observation of ultrafast large-scale dynamics of an enzyme under turnover conditions | PNAS <https://www.pnas.org/doi/abs/10.1073/pnas.1720448115> (accessed 2022 -04 -01).
- (9) Analysis of Complex Single-Molecule FRET Time Trajectories - ScienceDirect <https://www.sciencedirect.com/science/article/pii/S0076687910720115> (accessed 2022 -04 -01).
- (10) Somssich, M.; Ma, Q.; Weidtkamp-Peters, S.; Stahl, Y.; Felekyan, S.; Bleckmann, A.; Seidel, C. A. M.; Simon, R. Real-Time Dynamics of Peptide Ligand-Dependent Receptor Complex Formation in Planta. *Sci. Signal.* **2015**, *8* (388), ra76.
- (11) Kapusta, P.; Wahl, M.; Benda, A.; Hof, M.; Enderlein, J. Fluorescence Lifetime Correlation Spectroscopy. *J. Fluoresc.* **2007**, *17* (1), 43–48.
- (12) Schuler, B. Single-Molecule FRET of Protein Structure and Dynamics - a Primer. *J. Nanobiotechnology* **2013**, *11 Suppl 1*, S2.
- (13) Lerner, E.; Barth, A.; Hendrix, J.; Ambrose, B.; Birkedal, V.; Blanchard, S. C.; Börner, R.; Sung Chung, H.; Cordes, T.; Craggs, T. D.; Deniz, A. A.; Diao, J.; Fei, J.; Gonzalez, R. L.; Gopich, I. V.; Ha, T.; Hanke, C. A.; Haran, G.; Hatzakis, N. S.; Hohng, S.; Hong, S.-C.; Hugel, T.; Ingargiola, A.; Joo, C.; Kapanidis, A. N.; Kim, H. D.; Laurence, T.; Lee, N. K.; Lee, T.-H.; Lemke, E. A.; Margeat, E.; Michaelis, J.; Michalet, X.; Myong, S.; Nettels, D.; Peulen, T.-O.; Ploetz, E.; Razvag, Y.; Robb, N. C.; Schuler, B.; Soleimaninejad, H.; Tang, C.; Vafabakhsh, R.; Lamb, D. C.; Seidel, C. A.; Weiss, S. FRET-Based Dynamic Structural Biology: Challenges, Perspectives and an Appeal for Open-Science Practices. *eLife* **2021**, *10*, e60416.
- (14) ATTO-TEC GmbH - ATTO-TEC GmbH <https://www.atto-tec.com/?language=de> (accessed 2022 -04 -01).
- (15) Chroma Technology Corp <https://www.chroma.com> (accessed 2022 -04 -01).
- (16) PyMOLWiki [https://pymolwiki.org/index.php/Main\\_Page](https://pymolwiki.org/index.php/Main_Page) (accessed 2022 -04 -01).
- (17) <https://www.jenabioscience.com/images/PDF/PP-305-647N.0002.pdf>.



- (18) [https://www.edinst.com/wp-content/uploads/2017/04/EI\\_FLS1000\\_Brochure\\_Product\\_02.2022\\_Stage-02.2.pdf](https://www.edinst.com/wp-content/uploads/2017/04/EI_FLS1000_Brochure_Product_02.2022_Stage-02.2.pdf).
- (19) Ghann, W.; Kang, H.; Emerson, E.; Oh, J.; Chavez-Gil, T.; Nesbitt, F.; Williams, R.; Uddin, J. Photophysical Properties of Near-IR Cyanine Dyes and Their Application as Photosensitizers in Dye Sensitized Solar Cells. *Inorganica Chim. Acta* **2017**, 467, 123–131.

# 5

## **FRET to a distribution of acceptors at the ensemble and single-molecule levels**

*Theodor Förster some 80 years ago predicted a stretched-exponential fluorescence intensity decay under ensemble conditions. This is related to a distribution of acceptors in the vicinity of each donor; the decay rate depends on the concentration of acceptor around the donor. These non-exponential kinetics arise from a distribution of the exponential steps. In chapter 5, we first tested the consistency of Förster's theory by studying an ensemble of the acceptors (ATTO575Q) around the donor (Azaoxatriangulenium, ADOTA) for different concentrations of the acceptor in a thin polymeric layer. The advantage of a dye-doped polymer layer is that it allows for control of the dispersion of the dye molecules in the polymer films and prevents any type of quenching other than that due to FRET. Our single-molecule study showed that histograms of the decay rates of single ADOTA molecules are much more sensitive to the heterogeneity than the average non-exponential decay.*

## 5.1 Introduction

Single-molecule spectroscopy has become an established technique to uncover heterogeneity in soft-matter and biological systems, for example, to study protein folding,<sup>1</sup> nucleic acid dynamics,<sup>2</sup> and to monitor electron transfer events in metalloproteins.<sup>3</sup> Although the interpretation of the complex signals in biological systems is challenging, fluorescence resonance energy transfer (FRET) signals between donor and acceptor at the single-molecule level provide reliable information about the individual single molecules and about their surroundings.

The non-radiative energy transfer called FRET proceeds from a photoexcited donor fluorophore to an acceptor molecule and competes with donor fluorescence for donor-acceptor distances in the 1-10 nm range. The FRET rate depends on the distance between donor and acceptor ( $r$ ) and is inversely proportional to the sixth power of  $r$  (Eq. 1.10). The FRET efficiency ( $E$ ) is defined as the fraction of donor excitations that are transferred to the acceptor. The histogram of FRET efficiencies and the corresponding donor-acceptor distances extracted from single-pair FRET data make it possible to follow the structural dynamics of biomolecules over time and to distinguish the different surrounding environments of single molecules. However, in ensemble experiments, both the spatial and temporal heterogeneities are averaged out, and most of the information about the complexity of system is lost.<sup>4-8</sup>

The aim of this chapter is to reveal the heterogeneity of a FRET process from single donor molecules to a set of acceptor molecules randomly distributed in space around each individual donor. This problem has been treated for an ensemble of donors by Theodor Förster in 1949.<sup>9</sup> He found a strongly non-exponential decay for the average donor fluorescence, which under reasonable assumptions, decays as a stretched

exponential,  $\exp\left[-\sqrt{\frac{t}{\tau_0}}\right]$ . Through single-molecule measurements, we want to show

that each single donor molecule decays as a single exponential, and that the stretched-exponential decay arises purely from the spatial averaging over donor molecules, with their individual distributions of acceptor molecules around each of them. For this, we design a system of donors and acceptors with a low concentration of donors and a higher concentration of acceptors, giving rise to a distribution of distances between each donor and a large number of acceptors in its vicinity. We will study FRET at both ensemble and single-molecule levels. We will measure fluorescence decays of the donors and plot histograms of donor lifetimes in presence of acceptors.

### 5.1.1 Non-fluorescent quenching

As we discussed in chapter 1 (Figure 1.4B), FRET does not require the acceptor to be fluorescent. When the fluorescence of the donor is quenched by the acceptor, the fluorescence intensity and the lifetime of the donor will change. This kind of FRET to a non-fluorescent acceptor has some advantages. For example, since the acceptor itself is not fluorescent, the background and related noise are reduced, which improves the signal-to-noise ratio, particularly for high concentrations of acceptors. Another advantage is the extended observation times because the acceptor dyes do not readily photo-bleach. Moreover, such studies prevent the problem of cross talk in emission detection, when the emission of both donor and acceptor may contribute to the detected signal.

Here, we used a long-lifetime fluorescent dye, ADOTA, as the donor and a non-fluorescent quencher (ATTO575Q) as the acceptor for both ensemble and smFRET studies. Note that the geometry of Fig. 5.1 is not exactly the random 3D distribution postulated by Förster for a homogeneous solution. However, due to the symmetry with respect to the plane interface, the situation in Fig. 5.1 corresponds to a 3D distribution with half the concentration of acceptors.

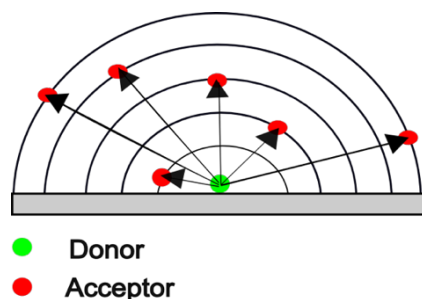


**Figure 5.1** A distribution of acceptors around a donor with different distances. The green dot represents the donor on the surface and the red dots are the acceptors distributed at various distances around the donor.

### 5.1.2 Donor: Long-lifetime fluorescent ADOTA dye, a triangulenium dye

The azaoxa-triangulenium fluorophores are organic molecules with planar and rigid structures in which three aromatic rings are bonded to a central carbon atom with a positive charge. This kind of red fluorophores is known as the longest-lived red emitting organic fluorophores because their lifetime in both protic and aprotic solvents is around 20-50 ns. Azadioxa-triangulenium (ADOTA) dyes absorb and emit in the red with a high quantum yield, long fluorescence lifetimes (16-20 ns) and high fluorescence anisotropy, close to the theoretical limit, 0.4.<sup>10-12</sup> These special characteristics of ADOTA make them suitable probes for fluorescent lifetime imaging (FLIM), time-gated fluorescence imaging, fluorescence lifetime and polarization measurements.<sup>13,14</sup>

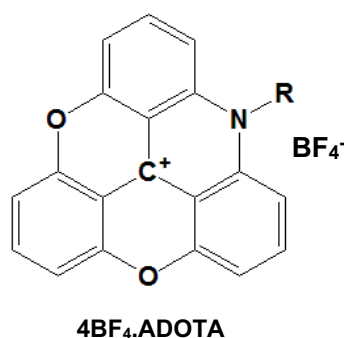


**Figure 5.2** The chemical structure of azadioxa-triangulenium dye (ADOTA)<sup>10,11</sup>

### 5.1.3 Acceptor: ATTO575Q, a non-fluorescent quencher dye

Here, we used the ATTO 575Q as a novel fluorescence quencher. This dye has an absorption spectrum with maximum absorbance at 582 nm (Figure 5.3) with a molar extinction coefficient of  $1.2 \times 10^5 \text{ M}^{-1} \text{ cm}^{-1}$ , and high thermal and photo-stability. ATTO 575Q is a cationic dye.<sup>15</sup>

### 5.1.4 Calculation of the Förster radius $R_0$ for ADOTA (donor)- ATTO575Q (acceptor)

As we showed in chapter 1 (eq. 1.8), the Förster radius  $R_0$  (the distance at which the energy transfer efficiency is 50%) depends on the overlap of the donor emission spectrum with the acceptor absorption spectrum and on their mutual molecular orientation. The calculated  $R_0$  assuming isotropic dye orientations is 6.38 nm. Figure 5.3 shows the absorption spectrum of ATTO575Q as the acceptor and the emission spectrum of ADOTA as the donor. Figure 5.4 shows that these spectra overlap strongly, leading to a large FRET radius.

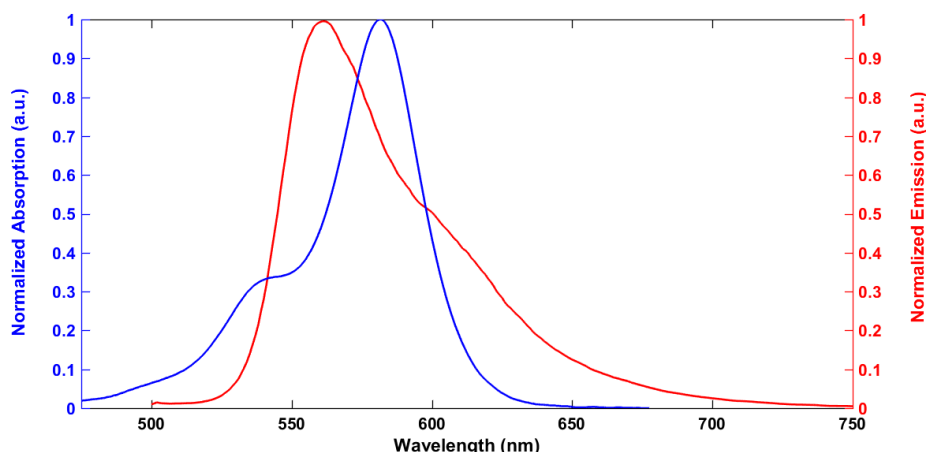


**Figure 5.3** The normalized absorption spectrum of ATTO575Q as acceptor (blue, left axis),<sup>15</sup> and the normalized fluorescence spectrum of ADOTA as donor (red, right axis) in phosphate buffer, pH=7, at room temperature.

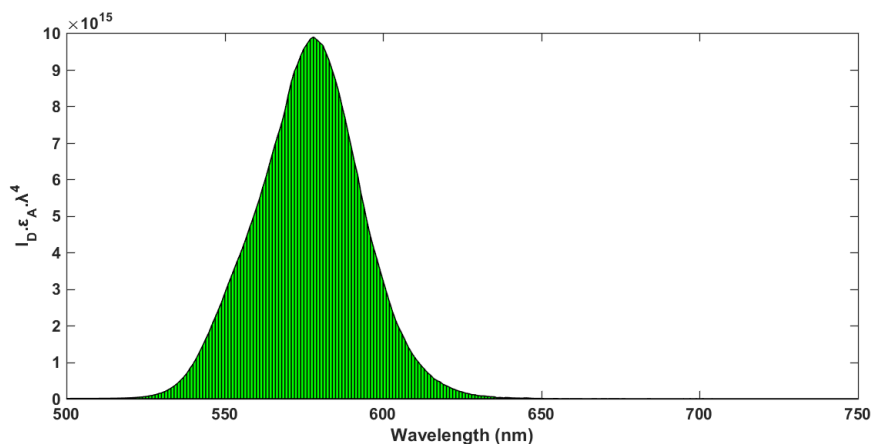


**Figure 5.4.** Product of the normalized absorption spectrum of the ATTO 575Q as the acceptor and of the normalized fluorescence spectrum of the ADOTA as the fluorescence donor. The overlap integral is proportional to the area under this curve (green area), based on equation 1.8 (as  $\int \bar{F}_D(\lambda) \epsilon_A(\lambda) \lambda^4 d\lambda$ ).

### 5.1.5 Ensemble fluorescent quenching

To study the fluorescent characteristics of a donor in presence of acceptors, it is crucial to avoid any chemical quenching due to aggregation. The concentrations have been chosen low enough that the dyes are well soluble in the different polymers used. Moreover, the solid polymers immobilize the donor and acceptor molecules and prevent rotational and translation diffusion. Lifetime measurements will be performed

on times short enough that donor and acceptor molecules will remain at fixed positions during the acquisition of the data.<sup>14,16,17</sup>

### 5.1.6 Ensemble measurements of fluorescence quenching in solid-state dye-doped polymer layers

To avoid the possibility of specific interactions between donor and acceptor in a 3D solution, we decided to incorporate the two dyes into different, immiscible polymers, PMMA and PVA. The donor dye (ADOTA) was doped into a poly(methyl methacrylate) (PMMA) polymer layer, which was spin-coated on the glass surface. The film thickness changes as a function of spin-coating conditions such as the weight percentage of the polymer in the solution, the rotation speed of the spin coater, etc. The uppermost layer of poly(vinyl alcohol) (PVA) was doped with the acceptor dye ATTO575Q and deposited homogeneously (drop casting) on top of the PMMA (Figure 5.5).

We optimized the spin-coating conditions to obtain a thin but regular ADOTA-doped PMMA layer of 6 nm thickness, whereas the acceptor-doped PVA layer was much thicker, about 100 nm. The finite thickness of the PMMA layer introduces a deviation from the Förster model, as the minimum distance between donor and acceptor will be 3 nm on average. We assume this deviation is not too large and does not significantly affect our results.

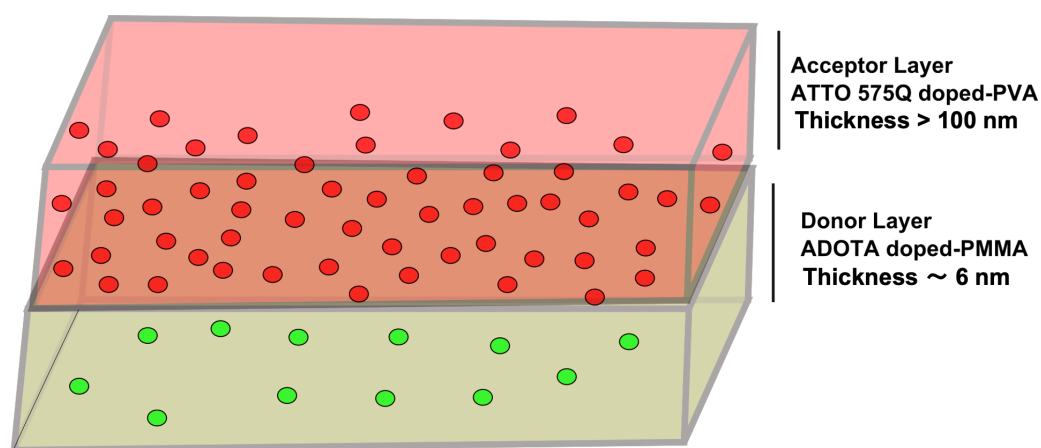


**Figure 5.5** Ensemble sample consisting of two layers. Top layer: ATTO575Q (acceptor) doped-PVA, thickness 100 nm. Bottom layer: ADOTA (donor)-doped PMMA, thickness 6 nm. The layers were deposited on a glass coverslip.

### 5.1.7 Fluorescence quenching as a function of quencher concentration

Due to the distribution of acceptors around each donor molecule, the fluorescence decay of an ensemble of donors is strongly non-exponential. Förster<sup>9</sup> derived an expression for the average fluorescence decay of an ensemble of donor dyes interacting with a random spatial distribution of acceptors, assuming that the distance between the donors was very large compared to the Förster radius. This decay takes the following simple form:

$$\overline{Q(t)} = e^{\frac{-t}{\tau_0} - \frac{NR_0^3\sqrt{\pi}}{Rg^3}\sqrt{\frac{t}{\tau_0}}} \quad 5.1$$

where  $t$ ,  $\tau_0$  are time and the fluorescence lifetime of the free donor dye, respectively, and  $R_0$ ,  $R_g$ ,  $N$  are the Förster radius, the radius of a large spherical volume of the acceptor solution, and the number of acceptor molecules in this spherical volume. We can reformulate Eq. 5.1 by using the concentration  $C$  of the acceptor:

$$\overline{Q(t)} = e^{\left[\frac{-t}{\tau_0} - \frac{4\pi C N_A R_0^3\sqrt{\pi}}{3}\sqrt{\frac{t}{\tau_0}}\right]} \quad 5.2$$

where  $N_A$  is the Avogadro number ( $6.023 \times 10^{23}$  molecule/mole).

Here, our aim is to study an ensemble and measure the averaged decay of the donor dyes and how it varies with the acceptor concentration.

### 5.1.8 Single-molecule fluorescence quenching

The measurement of the fluorescence of an ensemble provides average values of the fluorescence characteristics such as lifetime and fluorescence intensity. Single-molecule observations, however, will eliminate ensemble averaging and will reveal the hidden heterogeneity of the sample.<sup>14</sup>

To study fluorescence quenching of a single donor molecule in presence of a distribution of acceptors, we used the same geometry and polymers as in the ensemble experiment (as described in section 5.1.5), but with an even lower concentration of donors.

Our first control experiment was to study the fluorescence decay of a single ADOTA molecule in PMMA in the absence of any acceptor (ATTO575Q) (Figure 5.5A). In this case we spread an acceptor-free PVA layer on top of the ADOTA-doped PMMA, to compare both with the ensemble results (see section 5.1.5) and with the single-molecule results (see section 5.2.7).

The second control experiment measured of the fluorescence quenching of single ADOTA molecules (donor) in the presence of ATTO575Q acceptors dispersed in the PMMA polymer matrix as well as in the PVA top layer with the same concentration of acceptors in both layers. The aim of this control experiment is to rule out sticking of donors and/or acceptors at the interface between the two polymers. For example, in the ADOTA-doped PMMA bottom layer and ATTO 575Q-doped PVA top layer, there is the possibility of the dyes sticking to the interface. Sticking to the glass-PMMA interface or to the PMMA-air interface would make for a very inhomogeneous distribution of donor-acceptor pairs.

The PMMA polymer layer was spin-coated on the glass surface and the concentration of ADOTA was around 1000 times less than in the ensemble sample, in order to reach the single-donor regime. The spin-coating procedure was the same for all samples. The thickness of donor-doped PMMA layer was measured to be 6 nm on average, whereas the thickness of the acceptor-doped PVA layer was more than 100 nm.

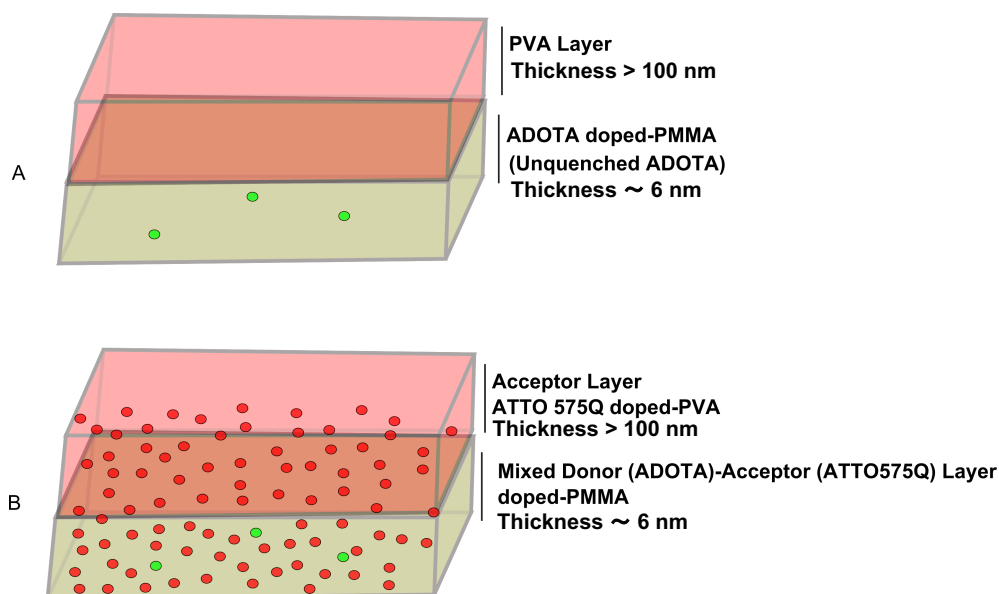


**Figure 5.6** Solid-state dye-doped polymer in the single-molecule fluorescence quenching assay. (A) ADOTA single molecule doped PMMA in the absence of acceptor (B) Both ADOTA (donor) and ATTO575Q (acceptor) dyes dispersed in PMMA polymeric matrix while the PVA top layer also contains the acceptor.

## 5.2 Results

### 5.2.1 Confocal setup

The confocal setup was a home-built microscope in which ADOTA dye (donor) is excited with a pulsed laser at 485 nm with a pulse rate of 26 MHz. The schematic illustration of the setup is shown in Figure 5.7. The collected photons were detected with time-correlated single-photon counting (TCSPC) and converted by the SymphoTime software to fluorescence decays.

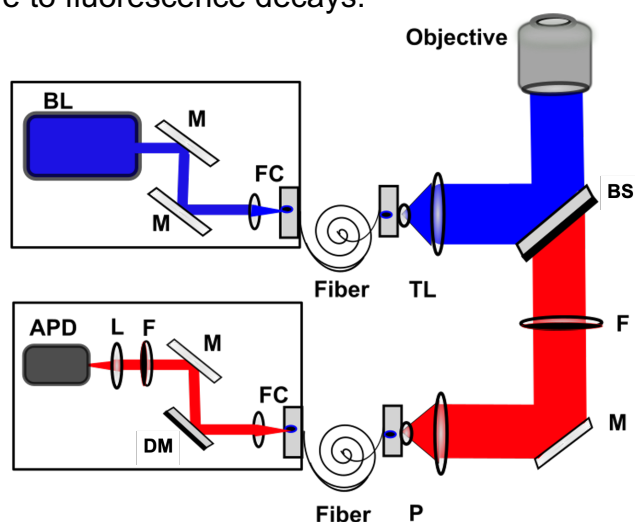


**Figure 5.7** Scheme of our home-built confocal setup for fluorescence decay measurements of FRET from a ADOTA donor to ATTO575Q acceptors. BL=Blue Laser, M=Mirror, FC= Fiber Collimator, L=Lens, TL=Telescope (Beam Expander), BS=Beam splitter, F=Filter, P=Pinhole, DM=Dichroic Mirror, APD=Avalanche Photodiode Detector.



### 5.2.2 Surface preparation of glass microscope cover slips

The surface preparation of clean glass microscope coverslips (No. 1, = 25 mm Hecht-Assistent, Sondheim, Germany) was done according to the following protocol: Both sides of the coverslip glasses were first washed with acetone, then blown dry with nitrogen gas. Then, both sides of the coverslips were rinsed with isopropanol and blown dry with nitrogen. The remaining solvents on the surface of the coverslips were removed through heating the coverslips for 2.5 hours at 170°C.

### 5.2.3 Ensemble sample preparation

The thin film of ADOTA-doped PMMA was prepared by spin-coating dilute ADOTA dye solutions (200 nM) in chloroform containing 1.0% w/w PMMA (average Mw 120000, Sigma Aldrich) onto the surfaced-prepared coverslips. The spin-coating program consists of sequential steps including: 10 seconds (500 rpm), 60 seconds (2000 rpm), and 10 seconds (4000 rpm). The samples were dried in the dark at room temperature. The fluorescent dye, Biotinylated-ADOTA, was purchased from the KU dye company, Copenhagen, Denmark. There were other possibilities of functional groups linked to the ADOTA such as amine, carboxyl, or amide groups instead of the biotin functional group but we selected the Biotinylated-ADOTA to decrease the possibility of chemical interaction of ADOTA to the surface of glass via this group. The thickness of the samples was measured with an AFM thickness profiler (BRUKER, Germany). Figure 5.8 shows the thickness profile of a prepared sample. The sample with 0.1% w/w PMMA has an average thickness of 6 nm (Figure 5.8A-B)

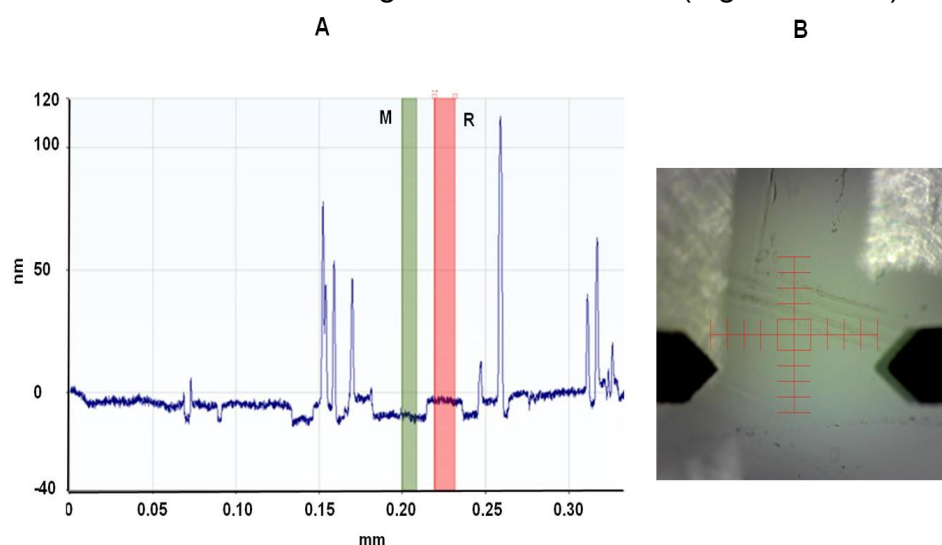


**Figure 5.8** The thickness profile of the prepared sample of ADOTA-doped PMMA spin-coated on the glass coverslip, and measured by an AFM thickness profiler. (A-B) Measurement of the thickness of the thin polymeric monolayer (with an average thickness of 6 nm). The sharp structures are caused by impurities on the surface. Scratching with the tip of the AFM makes a depression in the surface, the depth of which corresponds to the film thickness. The sample was prepared with 0.1% w/w PMMA.

The acceptor (ATTO575Q)-doped PVA layers were prepared by diluting a few drops of an aqueous solution containing ATTO575Q mixed with 1% w/w PVA (99+% hydrolyzed, average Mw 120,000, Sigma Aldrich) in water to reach the desired final

concentration in PVA (400  $\mu\text{M}$ , 1 mM, 3 mM, and 5 mM) and was spread on top of the ADOTA-doped PMMA layer on the glass surface. The sample was dried at room temperature over time in the dark. The non-fluorescent dye, ATTO575Q was purchased from Atto-Tec (Siegen, Germany).

It should be noted that the spin-coating rate and the polymer weight percentage are crucial to make a very thin polymeric layer. For all samples in this chapter, this protocol was applied to have a very thin layer. The reason of preparation of such a thin polymeric layer is that the distance between the donor and acceptor should be between 1-10 nm to be able to study FRET due to the quenching of the donor in presence of acceptors.

### 5.2.4 Ensemble fluorescent lifetime quenching measurements

The fluorescence time traces and fluorescence decay curves of ADOTA-doped PMMA (bottom layer) in presence of ATTO 575Q-doped PVA (with the different concentrations 400  $\mu\text{M}$ , 1 mM, 3 mM, and 5 mM) were recorded using our confocal microscope. Based on equation 5.2, the fluorescent decay of ADOTA (donor) is substantially quenched when the concentration of quencher (ATTO 575Q) in the top polymer layer is increased. Figure 5.9 shows the experimental fluorescence decays (dark colors) and the fit to equation 5.2 (lighter colors). The theoretical fits in this figure were obtained by varying the concentration and the concentrations are 0.25, 1.1, 2.8, and 5.7 mM for the experimental used concentration of 0.400 mM, 1 mM, 3 mM, and 5 mM respectively. It should be noted that the fits have been convoluted with IRF to be compatible with experimental data.

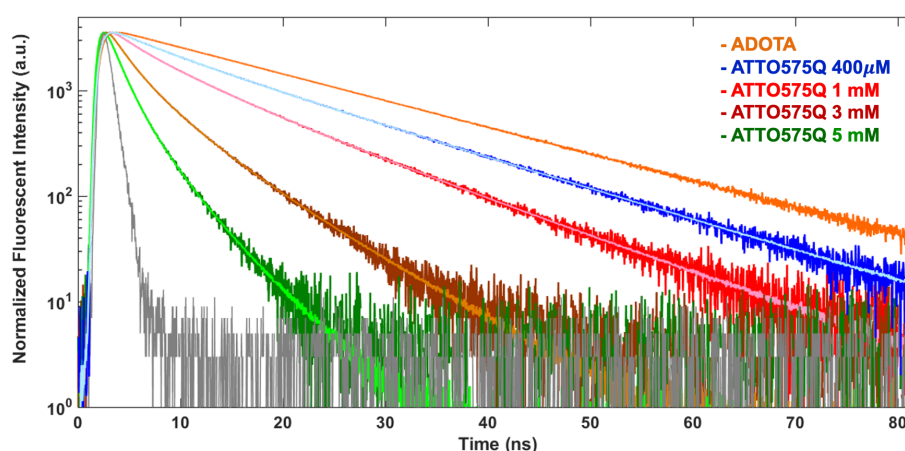


**Figure 5.9** Fluorescence decay (dark colors) and fit (lighter colors) for ADOTA donors in presence of four different concentrations of ATTO575Q acceptors: 400  $\mu\text{M}$  (blue), 1 mM (red), 3 mM (brown), 5 mM (green). The orange-colored decay is the mono-exponential decay of ADOTA in the absence of quencher. The gray decay curve is the Instrument Response Function (IRF). The fits in this figure were obtained by varying the concentration (adjustable parameter) and the best fits yielded with concentrations of 0.250, 1.1, 3.2, and 5.7 mM corresponding with the traces obtained with concentrations of 0.400 mM, 1 mM, 3 mM, and 5 mM respectively.

### 5.2.5 Single-molecule sample preparation

To study the donor (ADOTA) fluorescence in the presence of acceptors (ATTO575Q) at the single-molecule level, we decreased the donor concentration to 200 picomolar.

All the steps for the surface preparation of coverslip glasses and dye-doped polymer layers are the same as for the ensembles described above, except for the lower concentration of ADOTA.

### 5.2.6 Single-molecule fluorescence lifetime measurements

The sample to study the single-molecule quenching was prepared as described in 5.2.3, and 5.2.5. The single-molecule images, fluorescence time traces and fluorescence decay curves were recorded using a confocal microscope. The scan image size is  $10\ \mu\text{m} \times 10\ \mu\text{m}$ . The surface scans were measured with the confocal microscope and the individual lifetimes of single molecules were obtained. Figure 5.10 shows the  $10\ \mu\text{m} \times 10\ \mu\text{m}$  image of a sample of ADOTA-doped PMMA in the absence of quenchers. Each single-molecule time trace of unquenched ADOTA molecules could be collected and showed single-step bleaching with a maximum duration of 2.7 s. All traces gave rise to mono-exponential fluorescence decays with an average lifetime of 18.3 ns and a very limited spread of lifetimes, from 17 to 19 ns.

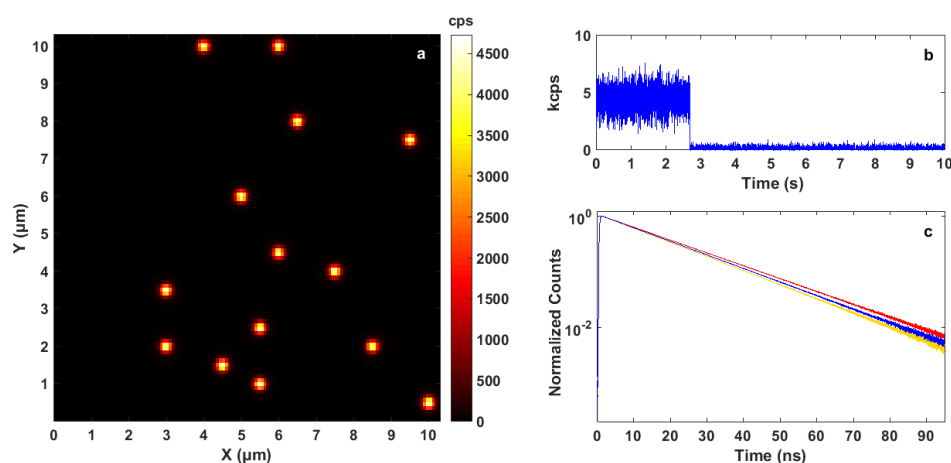


**Figure 5.10 Single molecules of unquenched ADOTA:** a) Single-molecule fluorescence image of PMMA doped with ADOTA; b) Single-molecule time trace of ADOTA showing single-step photobleaching after 2.7 s. This time trace was recorded by focusing on a single molecule embedded in the PMMA film for 1 minute; c) Normalized fluorescence decay curves of three single ADOTA molecules showing mono-exponential behavior.

Figure 5.11 shows a  $10\ \mu\text{m} \times 10\ \mu\text{m}$  image of a sample in which the first PMMA layer, 6 nm thick, was doped with a mixture of ADOTA (donor) and ATTO575Q (acceptors) (1mM). After this first layer was spin-coated on a coverslip, a thick PVA layer (thickness  $> 100\ \text{nm}$ ) doped with ATTO 575Q was added. This control experiment is meant to check that there was no sticking of the donor or acceptors to the glass-PMMA interface or to the PMMA-PVA interface. If such sticking occurs, we expect stronger quenching when the acceptors are present in the PMMA layer. In the case of donor sticking to the glass surface, we expect a larger distance on average between the donor and the acceptors, and therefore less quenching on average. We found no significant difference between the measured samples and the controls, which points to the absence of significant sticking of the donor to the glass or of the acceptor to the PMMA. Figure 5.11b shows a single-molecule time trace of a quenched ADOTA showing photoblinking and single-step photobleaching. The fluorescence decay

curves of different single ADOTA molecules in Fig. 5.11c show mono-exponential decays with a wide range of lifetimes. Single-exponential fits are represented as solid lines and fit the decays perfectly.

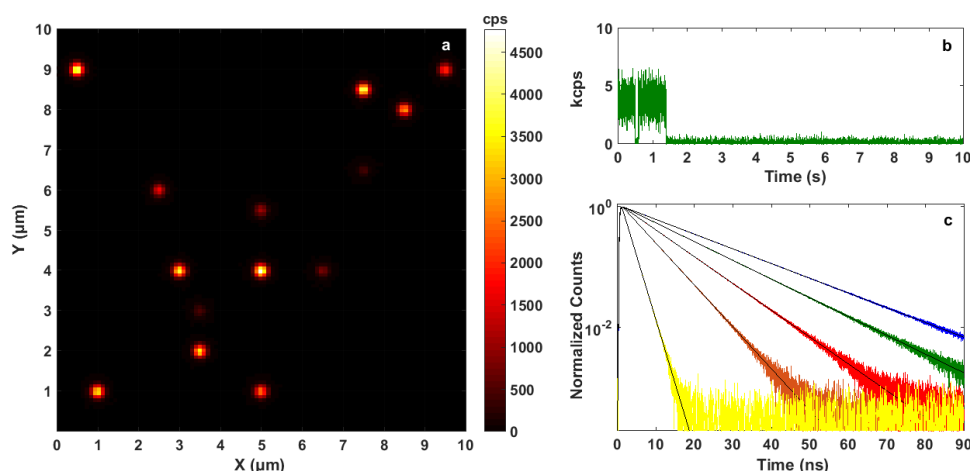


**Figure 5.11 Single molecule of quenched ADOTA with ATTO 575Q :** a) A  $10\ \mu\text{m} \times 10\ \mu\text{m}$  image of Single ADOTA molecules doped in PMMA with a mixture of ATTO 575Q (1mM), spin coated on a coverslip glass as a first layer and covered with a thick PVA film doped with ATTO 575Q (1 mM); b) A single-molecule time trace of a partially quenched ADOTA molecule showing photoblinking and single-step photobleaching; c) Normalized fluorescence decay curves of different single ADOTA molecules showing single-exponential decays with a wide range of lifetimes and their mono-exponential decay fits (black lines). Decay curves were recorded by focusing on individual molecules embedded in the PMMA film.

## 5.3 Discussion

### 5.3.1 Comparison of single-molecule results with and without quenchers

In the presence of acceptors (ATTO575Q), the histogram of lifetimes of the ADOTA donor molecules was profoundly altered in comparison to the unquenched histogram (see decays in Fig. 5.10). The lifetime histogram of quenched ADOTA donors show dramatic broadening and heterogeneity, as shown by the yellow plot in Fig. 5.12b, in comparison with the very narrow and homogeneous histogram of unquenched ADOTA in Fig. 5.12a.

To understand better this heterogeneity, we simulated a lifetime histogram of ADOTA donor in the presence of a random 3D distribution of quenchers (ATTO575Q) (see Eqs. 5.2, and 1.11) in which the value of  $R_0$  (Förster Radius),  $\tau_0$  (Lifetime of free ADOTA in the absence of acceptor), and  $C$  (concentration of ATTO575Q) have been assigned as 6.38 nm, 18.5 ns, and 1 mM. In this simulation, we placed the donor at the origin and distributed acceptors randomly in space around it, with a probability defined by the concentration. Then the total transfer rate towards the acceptors was calculated. As can be seen in Figure 5.12b, both experimental and simulated data show a broad and inhomogeneous distribution of lifetimes, with a significant weight for short lifetimes. Because the time resolution of our time-correlated photon counting apparatus is limited, and because of the weakness of the signals, we cannot measure lifetimes shorter than 0.5 ns. This may explain the large deviation of experimental data from the simulated histogram at lifetimes below 1-2 ns (see Fig. 5.12b).

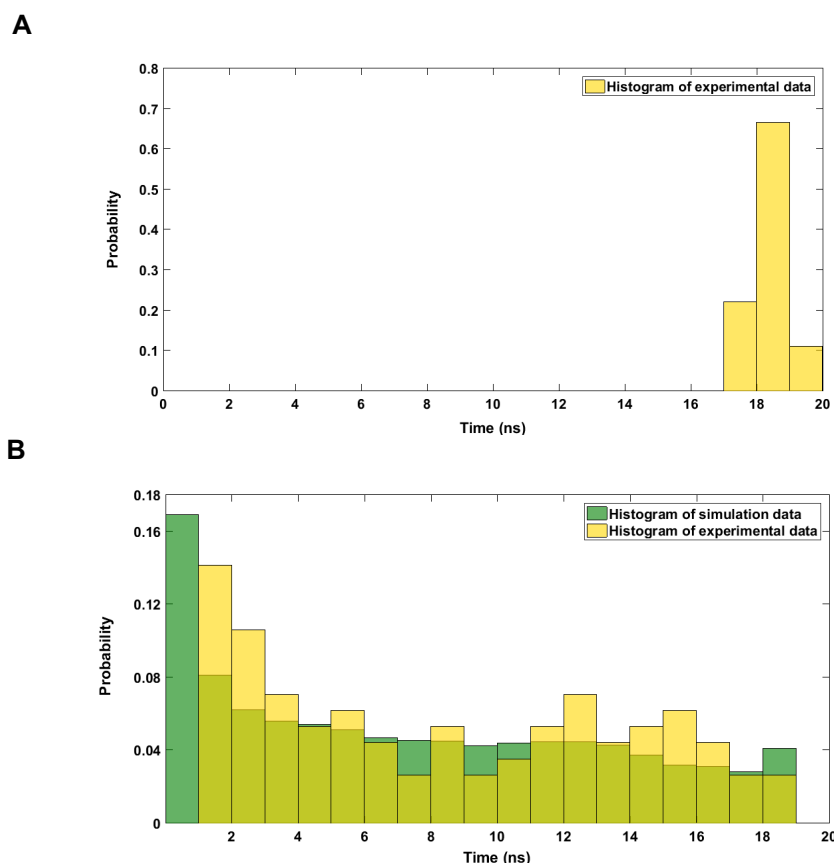


**Figure 5.12** Comparison of data lifetimes histograms of all single molecules from (A) 9 unquenched ADOTA molecules, which shows a low spread of lifetime weighted to long life times and (B) 103 quenched ADOTA molecules in the presence of ATTO 575Q (1mM) (yellow). Simulated data (green) which shows a broad and inhomogeneous distribution of lifetimes and weighted to the short lifetimes, similar to what observed for the experimental data.

### 5.3.2 Comparison of ensemble and single molecule results

The single-molecule images and lifetime histograms demonstrate the distribution of individual molecular properties such as intensity and decay rate. These properties are averaged out in the ensemble measurements giving rise to a multi-exponential decay of the donor fluorescence in presence of acceptors. The non-exponential decay is well reproduced by the formula of Förster, as shown in Fig. 5.9. The complex multiexponential decay of the ensemble measurement resolves into a collection of single-exponential decays with very different decay rates for each individual molecule, corresponding to the particular distribution of acceptors that each single donor molecule experiences.

## 5.4 Conclusion

Some 80 years ago, Theodor Förster predicted a stretched-exponential decay for an ensemble of donors when each of them can transfer energy to a distribution of acceptors. When donor and acceptors are immobilized, this non-exponential kinetics arises from a static distribution of individual exponential decays. In this chapter, we designed ensemble experiments to study transfer from ADOTA donors (Azaoxatriangulenium) towards a distribution of acceptors (ATTO575Q as quenchers). The

donor was chosen because of its high quantum yield and long fluorescent lifetime. The dyes were placed in thin polymeric layers to immobilize them and to prevent direct chemical interactions between them. The “ensemble” fluorescence quenching data of ADOTA (donor) in presence of ATTO 575Q (acceptor) in Fig. 5.9 fit Förster’s theory (eq. 5.2) very well. As expected, the quenching of the donor increases with the concentration of acceptors.

To compare ensemble results with single donor molecule experiments, we used the same system of donor-acceptor, and varied the acceptor concentration. As expected, the fluorescence decays of single donor molecules were all single-exponential with a wide spread of decay times (see Figure 5.11), as expected for Förster energy transfer towards a fixed distribution of acceptors. The wide distribution of decay rates results into the strongly non-exponential decays of Figure 5.9. On the basis of the lifetime histograms presented in Figure 5.12, we find a remarkable agreement between the observed lifetimes of individual donors and simulations assuming a homogeneous distribution of acceptors in the vicinity of the donors.

In conclusion, the spatial heterogeneity in the ensemble measurements is revealed by single-molecule measurements and show a large spread of local quenching situations. By measuring a large number of single molecules (here 103), we obtain a histogram of exponential lifetimes, which not only reproduce the ensemble results, but give a much more detailed view of the distribution of distances at the level of single molecules, in qualitative agreement with simulations.

## References

- (1) Deniz, A. A.; Laurence, T. A.; Beligere, G. S.; Dahan, M.; Martin, A. B.; Chemla, D. S.; Dawson, P. E.; Schultz, P. G.; Weiss, S. Single-Molecule Protein Folding: Diffusion Fluorescence Resonance Energy Transfer Studies of the Denaturation of Chymotrypsin Inhibitor 2. *Proc. Natl. Acad. Sci. U. S. A.* **2000**, 97 (10), 5179–5184.
- (2) Karymov, M. A.; Chinnaraj, M.; Bogdanov, A.; Srinivasan, A. R.; Zheng, G.; Olson, W. K.; Lyubchenko, Y. L. Structure, Dynamics, and Branch Migration of a DNA Holliday Junction: A Single-Molecule Fluorescence and Modeling Study. *Biophys. J.* **2008**, 95 (9), 4372–4383.
- (3) Tabares, L. C.; Gupta, A.; Aartsma, T. J.; Canters, G. W. Tracking Electrons in Biological Macromolecules: From Ensemble to Single Molecule. *Mol. Basel Switz.* **2014**, 19 (8), 11660–11678.
- (4) Pradhan, B.; Engelhard, C.; Van Mulken, S.; Miao, X.; Canters, G. W.; Orrit, M. Single Electron Transfer Events and Dynamical Heterogeneity in the Small Protein Azurin from *Pseudomonas Aeruginosa*. *Chem. Sci.* **11** (3), 763–771.
- (5) Tabares, L. C.; Kostrz, D.; Elmalk, A.; Andreoni, A.; Dennison, C.; Aartsma, T. J.; Canters, G. W. Fluorescence Lifetime Analysis of Nitrite Reductase from *Alcaligenes Xylosoxidans* at the Single-Molecule Level Reveals the Enzyme Mechanism. *Chem. Weinh. Bergstr. Ger.* **2011**, 17 (43), 12015–12019.

- (6) Zondervan, R.; Kulzer, F.; Kol'chenk, M. A.; Orrit, M. Photobleaching of Rhodamine 6G in Poly(Vinyl Alcohol) at the Ensemble and Single-Molecule Levels. *J. Phys. Chem. A* **2004**, *108* (10), 1657–1665.
- (7) Vogel, S. S.; Nguyen, T. A.; van der Meer, B. W.; Blank, P. S. The Impact of Heterogeneity and Dark Acceptor States on FRET: Implications for Using Fluorescent Protein Donors and Acceptors. *PloS One* **2012**, *7* (11), e49593.
- (8) Sanabria, H.; Rodnin, D.; Hemmen, K.; Peulen, T.-O.; Felekyan, S.; Fleissner, M. R.; Dimura, M.; Koberling, F.; Kühnemuth, R.; Hubbell, W.; Gohlke, H.; Seidel, C. A. M. Resolving Dynamics and Function of Transient States in Single Enzyme Molecules. *Nat. Commun.* **2020**, *11* (1), 1231.
- (9) Förster, V. T. Experimentelle und theoretische untersuchung des zwischenmolekularen übergangs von elektronenanregungsenergie. *Z.Naturforschg.* **1949**, *4a*, 321-327.
- (10) Bora, I.; A. Bogh, S.; Rosenberg, M.; Santella, M.; Just Sørensen, T.; W. Laursen, B. Diazaoxatriangulenium: Synthesis of Reactive Derivatives and Conjugation to Bovine Serum Albumin. *Org. Biomol. Chem.* **2016**, *14* (3), 1091–1101.
- (11) Robust Long Fluorescence Lifetime Dyes. *KU dyes*.
- (12) Sørensen, T. J.; Thyraug, E.; Szabelski, M.; Luchowski, R.; Gryczynski, I.; Gryczynski, Z.; Laursen, B. W. Azadioxatriangulenium (ADOTA<sup>+</sup>): A Long Fluorescence Lifetime Fluorophore for Large Biomolecule Binding Assay. *Methods Appl. Fluoresc.* **2013**, *1* (2), 25001.
- (13) Maliwal, B. P.; Fudala, R.; Raut, S.; Kokate, R.; Sørensen, T. J.; Laursen, B. W.; Gryczynski, Z.; Gryczynski, I. Long-Lived Bright Red Emitting Azaoxa-Triangulenium Fluorophores. *PLoS ONE* **2013**, *8* (5), e63043.
- (14) Kacenauskaite, L.; Bisballe, N.; Mucci, R.; Santella, M.; Pullerits, T.; Chen, J.; Vosch, T.; Laursen, B. W. Rational Design of Bright Long Fluorescence Lifetime Dyad Fluorophores for Single Molecule Imaging and Detection. *J. Am. Chem. Soc.* **2021**, *143* (3), 1377–1385.
- (15) ATTO-TEC GmbH - ATTO-TEC GmbH <https://www.atto-tec.com/?language=de> (accessed 2022 -04 -29).
- (16) Shundo, A.; Okada, Y.; Ito, F.; Tanaka, K. Fluorescence Behavior of Dyes in Thin Films of Various Polymers. *Macromolecules* **2012**, *45* (1), 329–335.
- (17) Gushiken, N. K.; Paganoto, G. T.; Temperini, M. L. A.; Teixeira, F. S.; Salvadori, M. C. Substrate for Surface-Enhanced Raman Spectroscopy Formed by Gold Nanoparticles Buried in Poly(Methyl Methacrylate). *ACS Omega* **2020**, *5* (18), 10366–10373.



# Summary

Förster Resonance Energy Transfer (FRET), is a known technique in biotechnology to monitor dynamics, conformational changes, and kinetics of binding-unbinding of small molecules in proteins through measuring inter- and intramolecular distance changes at a scale of 1-10 nm. FRET is based on a dipole dipole interaction between two fluorescent dyes (donor and acceptor) resulting in non-radiatively energy transfer from excited state of the donor to an acceptor molecule which is reversely proportional to the six power of distance between donor and acceptor ( $R^{-6}$ ). In this thesis we focus on the Förster resonance energy transfer technique to study the kinetics of binding and dissociation of CO to and from myoglobin which has been fluorescently labeled (Chapters 3,4). FRET quenching is reported for an acceptor (ATTO575Q dye) and a donor (Azaoxa-triangulenium, ADOTA dye) doped in thin polymeric layers at both ensemble and single molecule level (Chapter 5).

## **The photodissociation of carboxymyoglobin (MbCO)**

Myoglobin (Mb) plays a vital role in transporting small molecules such as  $O_2$ , CO, and NO. The mechanism of the reaction of these ligands with ferrous Mb (deoxy-Mb) is interesting because the binding is reversible and the system can be used as a prototype for more complex systems.

Early time-resolved experiments by Frauenfelder and coworkers on ensembles of myoglobin demonstrated that, at cryogenic temperatures, rebinding of CO to myoglobin's heme cofactor after flash photolysis shows a strongly stretched exponential behavior, that is not observed at room temperature. This low temperature behavior has been assigned to structural heterogeneity of myoglobin and different rebinding rates of CO, but no direct observation of this effect exists to date. The conclusion of these experiments was that the reaction rates of individual molecules there exhibit large spread.

The protein relaxations and fluctuations are nonexponential in time at room temperature, which points to the possibly collective nature of these motions. Although recently a few studies have focused on the variation of protein reaction rates by means of single-molecule experiments, the mechanism by which small molecules such as CO bind/unbind to the heme of myoglobin is less well understood. In particular insight in the kinetics of CO rebinding at single molecule level is missing. Our aim is to study the rebinding kinetics of CO through fluorescence quenching of a dye attached to the myoglobin and by using FRET.

## **Estimation of dissociation quantum yield of the Mb-CO bond**

In chapter 3, FRET technology is described which was used to determine the interaction between myoglobin and CO. In this system, donor emission (dye attached to the myoglobin) is quenched through a non-fluorescent acceptor (myoglobin). The acceptor can be a different state of myoglobin for example deoxy-Mb in which CO is unbound from Mb, can act as a quencher and MbCO where CO is bound to Mb has no quenching effect or less. The weak bands beyond 700 nm, particularly Band III at 760 nm, in the deoxy-Mb absorption spectrum quenches the fluorescence of a deep red dye, whereas those bands beyond 700 nm are absent in the spectrum of MbCO.



It is well known that visible light in a wide spectral range, particularly  $400 < \lambda < 550$  nm, breaks the Mb-CO bond with high efficiency, which precludes FRET-based investigations of CO dissociation in this spectral region. We therefore developed a strategy involving the far-red spectral region,  $\lambda > 700$  nm. The challenge is that if red-light illumination of a labeled MbCO would break the Mb-CO bond with high efficiency, probing the absorption of MbCO with red light would make it impossible to monitor CO rebinding by fluorescence spectroscopy and FRET. For this reason, we wanted to obtain the quantum yield for photodissociation of the Mb-CO under red-light illumination ( $\lambda > 700$  nm). Three states of myoglobin, met-Mb (heme contains  $\text{Fe}^{3+}$ ), deoxy-Mb (heme contains  $\text{Fe}^{2+}$ ), and MbCO (heme contains  $\text{Fe}^{2+}$ ), have been prepared and optically characterized.

Experimentally the quantum yield of Mb-CO bond breaking is established by following the number of deoxy-Mb molecules that have not re-bound to CO at a given time after photodissociation. Because the recombination of CO to the heme is fast, it is essential to slow down the kinetics of recombination of the escaped CO molecule to the heme. CO molecules after photodissociation and escaping from the protein should be removed from the vicinity of the newly formed deoxy-Mb. We prevented CO recombination chemically by using  $\text{H}_2\text{O}_2$  as an oxidant which quickly converts the deoxy-Mb to another form that does not bind CO, for example met-Mb. The exact amount of MbCO converted to deoxy-Mb was measured by following the absorption spectrum of MbCO (using the absorption bands at 542 nm and 579 nm which are characteristic of MbCO). As the quantum yield of MbCO bond breaking by blue light is close to 1, we could use this photoreaction as a reference. By comparing the effect of MbCO illumination by a red LED ( $\lambda = 730$  nm) in the presence of  $\text{H}_2\text{O}_2$  with the effects of the blue LED illumination ( $\lambda = 450$  nm) we could estimate an upper bound quantum yield of MbCO photodissociation by red light ( $\lambda = 730$  nm) of less than 6%.

### **FRET study of CO binding to fluorescently labeled myoglobin**

Based on the estimated quantum yield of bond breaking in (see chapter 3), we concluded that illumination of MbCO with far-red light (700-800 nm) does not break the Mb-CO bond efficiently and the MbCO complex should be stable enough to monitor FRET from the far-red donor to the heme, with enough donor fluorescence photons emitted before dissociating MbCO during the FRET measurement. For the FRET experiment selection of the proper dye, position of labeling on the protein and the labelling method are crucial. For this purpose, not only an independent estimation of FRET efficiency is needed to characterize CO re-binding but also the development of quantitative methodologies for steady-state parameters of ligand binding is crucial. In chapter 4, we performed two different labelling methods: labelling at engineered sites and N-terminal labelling. Different dyes were tried (ATTO643, ATTO740, and Cy7) which absorb and emit in the red. Various labeling positions for example at position of serine 3 were realized by site-directed mutagenesis. During the FRET experiments we measured the fluorescence intensity of the dye and/or the fluorescence lifetime of labelled Met-Mb, Deoxy-Mb and MbCO. We could observe significant intensity differences for ATTO 740 labeled-deoxy-Mb and -MbCO which show that it is possible to distinguish these two states in a mixture.

### **Non-fluorescent quenching for FRET assay in ensemble and at the single molecule level in polymeric layer**

Single Molecule FRET (sm-FRET) may provide the distributions of experimental parameters such as excited state lifetime, fluorescent intensity, local environmental fluctuations, etc. Theodor Förster some 80 years ago predicted a stretched-exponential fluorescence intensity decay under ensemble conditions. This is related to a distribution of acceptors in the vicinity of each donor; the decay rate depends on the concentration of acceptor around the donor. These non-exponential kinetics arise from distributions of exponential steps. In chapter 5, we first tested the consistency of Förster's theory by studying an ensemble of the acceptors (ATTO575Q) around the donor (Azaoxa-triangulenium, ADOTA) for different concentrations of acceptor in a thin polymeric layer. The advantage of dye-doped polymer layer is that it allows for control of the dispersion of the dye molecules in the polymer films and prevents any type of quenching other than FRET. Our single-molecule study showed that histograms of decay rates of single ADOTA molecules are much more sensitive to heterogeneity than the average non-exponential decay. Each individual molecule exhibits a single-exponential fluorescence intensity decay, but the distribution of acceptor sites around each molecule produces a wide distribution of decay rates.



# Samenvatting

Förster Resonance Energy Transfer (FRET) is een bekende optische techniek in de biotechnologie waarmee men de dynamiek en conformatie veranderingen van eiwitten kunt volgen. Ook kan men de kinetiek van binding-ontbinding volgen van kleine moleculen aan eiwitten. Dit kan allemaal door de gevoeligheid van FRET voor inter- en intramoleculaire afstandsveranderingen tussen twee kleurstofmoleculen op een onderlinge afstand van 1-10 nm. FRET is gebaseerd op de dipool-dipool interactie tussen twee fluorescerende kleurstoffen (donor en acceptor) waarbij een stralingsloze energieoverdracht plaatsvindt van de aangeslagen toestand van de donor naar een acceptormolecuul. De grote van deze overdracht is omgekeerd evenredig met de zesde macht van de afstand tussen donor en acceptor ( $R^{-6}$ ). In dit proefschrift bestuderen we de kinetiek van CO binding aan en dissociatie vanaf fluorescent gelabelde myoglobine, waarbij we gebruiken maken van onderscheidbare FRET eigenschappen van verschillende toestanden van myoglobine (Hoofdstukken 3, 4). Ook wordt FRET doving (quenching) gerapporteerd voor een acceptor (ATTO575Q-kleurstof) gebonden aan de myoglobine en een donor (Azaoxa-triangulenium, ADOTA-kleurstof) dat is gedoteerd in een dunne polymeer laag. De experimenten zijn uitgevoerd op zowel ensemble- als enkelmolecuulniveau (Hoofdstuk 5)

## **De fotodissociatie van carboxymyoglobine (MbCO)**

Myoglobine (Mb) speelt een vitale rol bij het transporteren van kleine moleculen zoals  $O_2$ , CO en NO. Het mechanisme van de reactie tussen deze verschillende liganden met ijzerhoudend Mb (deoxy-Mb) is interessant omdat de binding omkeerbaar is en het systeem kan worden gebruikt als prototype voor complexere systemen.

Eerdere tijdsopgeloste experimenten door Frauenfelder en collega's op ensembles van myoglobine toonden aan, bij cryogene temperaturen, dat herbinding van CO aan de heem-cofactor van myoglobine na flash fotolyse een sterk uitgerekt exponentieel gedrag vertoont. Dit wordt niet waargenomen bij kamertemperatuur. Dit gedrag bij lage temperaturen wordt toegeschreven aan de structurele heterogeniteit van myoglobine en aan de verschillende herbindingssnelheden van CO. Tot op heden bestaat er echter geen directe waarneming van deze processen. De conclusie die werd getrokken uit deze experimenten was dat van individuele moleculen de reactiesnelheid een grote spreiding vertoont.

De relaxaties en fluctuaties van het eiwit zijn niet-exponentieel over de tijd bij kamertemperatuur, wat wijst op een mogelijk collectief karakter van deze bewegingen. Hoewel recent een paar onderzoeken zich hebben gericht op de variatie van eiwitreactiesnelheden door middel van enkel molecuul experimenten, is het mechanisme waarmee kleine moleculen zoals CO binden/ontbinden aan het heem van myoglobine nog niet goed begrepen. Met name inzicht in de kinetiek van CO-herbinding op enkel-molecuul niveau ontbreekt. Ons doel is om de herbindingsskinetiek van CO te bestuderen door middel van fluorescentie doving van een kleurstof die aan de myoglobine is gebonden en door verschillende configuraties van FRET experimenten toe te passen.

### **Schatting van de dissociatie kwantumopbrengst van de Mb-CO-verbinding**

In hoofdstuk 3 wordt de FRET techniek beschreven die is gebruikt om de interactie tussen myoglobine en CO te bepalen. In dit systeem wordt de donoremissie (kleurstof gehecht aan de myoglobine) gedoofd door een niet-fluorescerende acceptor (toestanden van myoglobine). Het dovingsmiddel kan bijvoorbeeld deoxy-Mb zijn waarin CO ongebonden is aan Mb, of MbCO waar CO is gebonden aan Mb. Deze toestanden hebben beide dovings eigenschappen maar MbCO heeft in verhouding geen of een minder dovend effect. Dit kan verklaard worden aan de hand van de zwakke banden boven de 700 nm en met de Band III bij 760 nm in het deoxy-Mb absorptiespectrum die de fluorescentie van een verroode kleurstof dooft, terwijl die banden voorbij 700 nm afwezig zijn in het spectrum van MbCO. Het is bekend dat zichtbaar licht in een breed spectraal bereik, in het bijzonder  $400 < \lambda < 550$  nm, de Mb-CO binding hoogst efficiënt verbreekt, wat FRET-gebaseerde onderzoeken naar CO-dissociatie in dit spectrale gebied uitsluit. Daarom hebben we een strategie ontwikkeld met betrekking tot het verroode spectrale gebied,  $\lambda > 700$  nm. De uitdaging is dat als rood licht van een gelabelde MbCO de Mb-CO-binding met hoge efficiëntie zou verbreken, het onderzoeken van de absorptie van MbCO met rood licht het onmogelijk zou maken om de CO-herbinding te volgen door middel van fluorescentiespectroscopie en FRET. Om deze reden wilden we eerst de kwantumopbrengst verkrijgen voor fotodissociatie van de Mb-CO onder rood licht ( $\lambda > 700$  nm). Drie toestanden van myoglobine, met-Mb (heem bevat  $\text{Fe}^{3+}$ ), deoxy-Mb (heem bevat  $\text{Fe}^{2+}$ ) en MbCO (heem bevat  $\text{Fe}^{2+}$ ), zijn daarom bereid gemaakt en optisch gekarakteriseerd.

Experimenteel wordt de kwantumopbrengst van het verbreken van Mb-CO-bindingen vastgesteld door het aantal deoxy-Mb-moleculen te volgen die niet opnieuw aan CO zijn gebonden op een gegeven tijdstip na fotodissociatie. Omdat de recombinitie van CO naar het heem snel is, is het echter essentieel om de kinetiek van recombinitie van het ontsnapte CO-molecuul naar het heem te vertragen. CO-moleculen moeten na fotodissociatie en het ontsnappen uit het eiwit worden verwijderd uit de buurt van het nieuw gevormde deoxy-Mb. We hebben CO-recombinitie chemisch voorkomen door  $\text{H}_2\text{O}_2$  te gebruiken als oxidatiemiddel dat het deoxy-Mb snel omzet in een andere vorm die CO niet bindt, bijvoorbeeld met-Mb. De exacte hoeveelheid MbCO omgezet in deoxy-Mb werd gemeten door het absorptiespectrum van MbCO te volgen (met behulp van de absorptiebanden bij 542 nm en 579 nm die kenmerkend zijn voor MbCO). Aangezien de kwantumopbrengst van de verbreking van MbCO-bindingen door blauw licht dicht bij 1 ligt, kunnen we dit als bijpassende referentie gebruiken.

Door te vergelijken wat het effect van verlichting door een rode LED ( $\lambda = 730$  nm) op MbCO is in aanwezigheid van  $\text{H}_2\text{O}_2$  met de effecten van de blauwe LED ( $\lambda = 450$  nm) konden we schatten dat er een bovengrens is van de kwantumopbrengst van MbCO-fotodissociatie bij rood licht ( $\lambda = 730$  nm) van minder dan 6%.

### **FRET-studie van CO-binding aan fluorescent gelabelde myoglobine**

Op basis van de geschatte kwantumopbrengst van het breken van bindingen (zie hoofdstuk 3), concluderen we dat belichting van MbCO met verrood licht (700-800 nm) de Mb-CO-binding niet efficiënt verbreekt en dat het MbCO-complex stabiel genoeg is om FRET van de verroode donor naar de heem te meten, met voldoende donorfluorescentiefotonen die worden uitgezonden voordat MbCO wordt gedissocieerd tijdens de meting. Voor het FRET experiment is selectie van de juiste kleurstof, zijn positie op het eiwit en de label methode cruciaal. Voor dit doel is niet alleen een onafhankelijke schatting van de FRET efficiëntie nodig om de herbinding

van CO te karakteriseren, maar ook de ontwikkeling van kwantitatieve methodologieën voor het meten van steady-state parameters van ligandbinding is cruciaal. In hoofdstuk 4 hebben we twee verschillende labelmethodes uitgevoerd: labelling op gemanipuleerde locaties en N-terminale labeling. Er werden verschillende kleurstoffen uitgetest (ATTO643, ATTO740 en Cy7) die in het rood absorberen en uitzenden. Verschillende labelposities, bijvoorbeeld op de positie van serine 3, werden gerealiseerd door plaatsgerichte mutagenese. Tijdens de FRET experimenten hebben we de fluorescentie intensiteit van de kleurstof en/of de fluorescentielevensduur van gelabeld Met-Mb, Deoxy-Mb en MbCO gemeten. We konden significante intensiteitsverschillen waarnemen tussen ATTO 740 gelabeld deoxy-Mb en MbCO met hetzelfde label, wat aantoont dat het mogelijk is om deze twee toestanden in een mengsel te onderscheiden.

### **Niet-fluorescerende uitdoving voor het FRET assay in ensemble en op enkel molecuul niveau in een polymeer laagje**

Single Molecule FRET (smFRET) kan de distributies verschaffen van experimentele parameters zoals de levensduur van de aangeslagen toestand, fluorescentie intensiteit, lokale omgevingsfluctuaties, enz. Theodor Förster voorspelde rond 80 jaar geleden een uitgerekt exponentieel verval van de fluorescentie-intensiteit onder ensemble omstandigheden. Dit hangt samen met een verdeling van acceptoren in de buurt van elke donor groep. Want de vervalsnelheid is afhankelijk van de acceptorconcentratie rond de donor. Deze niet-exponentiële kinetiek komt voort uit verdelingen van exponentiële stappen. In hoofdstuk 5 hebben we eerst de consistentie van Förster's theorie getest voor een ensemble van acceptoren (ATTO575Q) rond de donor (Azaoxa-triangulenium, ADOTA). Dit hebben we bestudeerd voor verschillende concentraties van acceptor in een dun polymeer laagje. Het voordeel van het gebruik van een met kleurstof gedoteerde polymeerlaagje is dat men de dispersie van de kleurstofmoleculen in de polymeerlaag kan reguleren en dat elk type uitdoving anders dan FRET kan worden voorkomen. Onze enkel molecuul studie toonde aan dat histogrammen van vervalsnelheden van individuele ADOTA-moleculen veel gevoeliger zijn voor heterogeniteit dan het gemiddelde niet-exponentiële verval. Elk individueel molecuul vertoont een enkelvoudig exponentieel verval van de fluorescentie intensiteit, maar de verdeling van acceptorposities rond elk molecuul produceert een brede verdeling van vervalsnelheden.



# Curriculum Vitae

I was born on 13th December 1979 in Falavarjan-Isfahan, Iran. I received my Bachelor in Pure Chemistry at the University of Isfahan-Iran in 2003. I was accepted for my first master in the field of Organic Chemistry under supervisory of Prof. M.A. Karimi Zarchi at University of Yazd, where my thesis was about a polymeric catalyst for organic synthesis. I received my master in 2005. From 2005-2010, I could obtain many experiences in the subject of organic chemistry synthesis in the presence of green reusable catalyst under supervisory of Prof. I. Mohammadpoor at chemistry department in the University of Isfahan. During 2005-2012, I have worked as part-time lecturer for bachelor students teaching organic chemistry, physical organic chemistry, spectroscopy, organic chemistry laboratory. These experiences pushed me into the depth of organic chemistry knowledge. In 2013 I had a research collaboration at Radboud University in the field of Peptide-Protein interaction and protein synthesis. In 2014, I worked as R&D manager in a project at Iron-Making company in Isfahan-Iran, where we could successfully innovate and develop a hybrid organic-inorganic polymer binder to reuse the waste fine coke at high temperature. In December 2015, I was accepted for my second master in Erasmus Mundus program founded by European Commission. I studied in the field of Chemical Innovation and Regulation at the University of Bologna; Italy and the University of Algarve/Tecnico Lisboa; Portugal. My master thesis was about tip-specific functionalization of gold nanorod with DNA as a nano-biosensor under supervisory of Dr. Pedro Paulo. In May 2018, I joined the single molecule optics group of Prof. Michel Orrit at Leiden University in the project of FRET study for Myoglobin protein and CO binding-unbinding to Myoglobin. In June 2020, I was awarded a grant by the HRSMC PhD mobility program for a visit to Prof. Don Lamb in chemistry department of LMU at Munich, Germany. From 2018-2021 I assisted in teaching the bachelor course biomolecular physics of Prof. Martina Huber at Leiden University. From 2019-2021, I served the Casimir PhD platform for organizing the winter-summer schools, workshops, and various courses for PhDs. From 2020-2021 I served in the LION PhD council.





# List of Publications

1. Karimi Zarchi M A, **Eskandari Z.** A Mild and Clean Synthesis of Alkyl Azides from Alkyl Halides Mediated by Poly(4-vinylpyridine)-Supported Sodium Azide Under Nonaqueous Conditions (2011) Journal of applied polymeric science 121: 1916–1920.
2. Mohammadpoor-Baltork I, Moghadam M, Tangestaninejad S, Mirkhani V, **Eskandari Z.** A Green and Selective Synthesis of 2-Aryloxazines and 2-Aryltetrahydropyrimidines (2011) Journal of Heterocyclic Chemistry 48: 479-483.
3. Mohammadpoor-Baltork I, Moghadam M, Tangestaninejad S, Mirkhani V, **Eskandari Z.** H<sub>3</sub>PW<sub>12</sub>O<sub>40</sub>: An Efficient and Recyclable Heterogeneous Catalyst for the Selective Synthesis of 2-Aryl-5,6-dihydro-4*H*-1,3-oxazines and 2-Aryl-1,4,5,6-tetrahydropyrimidines (2010) Z. Naturforsch. 65b: 461-469.
4. Mohammadpoor-Baltork I, Moghadam M, Tangestaninejad S, Mirkhani V, **Eskandari Z.** Ultrasound promoted selective synthesis of 2-aryl-5,6-dihydro-4*H*-1,3-oxazines catalyzed by K-10 and KSF montmorillonite clays: A practical procedure under mild and solvent-free conditions (2010) Ultrasonics Sonochemistry 17: 857-862.
5. Mohammadpoor-Baltork I, Moghadam M, Tangestaninejad S, Mirkhani V, **Eskandari Z.** Chemoselective Synthesis of 2-Aryloxazines and 2-Aryltetrahydropyrimidines Using Nano-SiO<sub>2</sub> as a Reusable Solid Acid Catalyst under Thermal Conditions and Microwave Irradiation (2010) J. Iranian Chem. Soc. 8: S 17- S 27.



# Acknowledgements

I am so glad for all support, guidance, and help that I have received during the four years of my PhD at Leiden University.

At the beginning, I would like to express my deep gratitude to Prof. Michel Orrit that offered me this possibility to combine Chemistry with Biophysics, for his guidance, support, and patience, and for the freedom I was given in my research. I would like to give my special thanks to Prof. Gerard Canters who taught me how to think deeply on chemical aspect of the research project, and answering all of my questions about chemistry, proteins, biochemistry and biophysics.

I would like to thank also to my second promotor, Prof. Sylvestre Bonnet, for following my progress in the project and for all of his suggestions, guidance, and support.

I owe a big and special thank to my daily supervisor Dr. Christopher Engelhrad who helped me with all fields of chemistry, protein, optics, and confocal microscopy. Special thanks for his patience, and for the time to teach me how to do research and how to think and understand problems fundamentally.

I greatly acknowledge Prof. Don Lamb in Ludwig-Maximilians-Universität München (LUM). I am so happy that we had the collaboration with his group, and for the duration of my visit. I acknowledge Damir and Ganesh Agham that helped me for the labeling of Myoglobin and preparation of Myoglobin states.

I gratefully acknowledge Henriette Van Leenuwen and Yvonne Kerkhof for all administration procedures and academic steps which have a lot of paper work on time, and also thanks to Henriette for her guidance when I had questions and for our nice conversations on coffee table.

I wish to appreciate my sincere gratitude to Prof. Martina Huber during my assistant teaching for the course of Molecular Physics for bachelor student of Leiden University. I would like to thank Lionel Ndamba and Laura van Opdam for training me in the protein labelling, protein purification, working with HPLC, FPLC, Liquid-Mass Chromatography, and SDS-page filtration. My thanks go to Harmen van der Meer for excellent mechanical support, and also to Peter van Veldhuizen, and René Overgauw. I would like to thank all of MoNOS members: Dr. Patrick Späth, Dr. Biswajit Pradhan, Dr. Weichung Zhang, Dr. Amin Moradi, Dr. Sergi Pud, Dr. Sids, Dr. Zoran Ristanovic, Dr. Xuxing Lu, Dr. Deep Punji, Dr. Subhasis Adhikari, Jacco Ton (specially for his great kindness to translate my summery-thesis into Dutch), Robert Smit, Dr. Martin Baaske, Dr. Martin Caldarola, Dr. Wiebke Albrecht, Nasrin Asghari, Jaccuil Labramunoz, Pryianshi Klara, and Dr. Thomas Jollans.

I am thankful to all of my colleagues in the Casimir PhD platform and the LION PhD committee.

Finally, I would like to thank my husband, Payam: although there is not a word in the human dictionary to thank you, I would say from my heart, great thank for your love, warm support, and all of your scientific help in programming and data analysis. I am deeply grateful that you have been sharing with me the sadness and happiness, and for your encouragement to reach high. Lastly, many thanks to our parents for supporting us.

